MATHEMATICAL MODELLING OF UNDERGROUND FLOW PROCESSES IN HYDROTHERMAL ERUPTIONS

A thesis presented in partial fulfilment of the
requirements for the degree of

Doctor of Philosophy
in
Mathematics

at Massey University, Palmerston North
New Zealand.

Thomasin Ann Smith

October 2000

Abstract

This thesis reports on a study of underground fluid flow and boiling processes which take place in hydrothermal eruptions. A conceptual model is presented for the eruptive process and a laboratory scale physical model confirming the effectiveness of this process is described. A mathematical formulation of the underground flow problem is given for two fluid flow regimes: two-phase homogeneous mixture (HM) flow and separable two-phase (SP) flow. Solutions to the system of equations obtained are solved under the simplifying assumptions of two-dimensional steady isothermal flow and transient non-isothermal horizontal flow. The main contribution of the study on steady isothermal flows is a description of how the ground flow may recover following a hydrothermal eruption. A numerical technique developed for plotting the streamlines in this case (and verified against analytic results) may also have applications in solving the steady non-isothermal flow problem. The main contribution of the study on the transient horizontal flow problem is a comparison of the differing predictions of HM and SP flow. The rate at which a boiling front progresses through a porous medium and the degree of boiling which occurs is described for each fluid flow regime. A set of horizontal physical experiments and numerical simulations have also been carried out for comparison with the mathematical model. Qualitative results for these three models agree. Suggestions given for improvements to the design of the physical experiment provide a basis for future study into the type of flow which occurs in hydrothermal eruptions.

Acknowledgements

- I would like to express my special gratitude to my chief supervisor Professor Robert McKibbin for providing me with a topic to explore that was both exciting and provided a range of modelling experiences (conceptual, mathematical and experimental). I highly valued his guidance, patience, and encouragement throughout this work and leave with respect for his contribution to this work and to the modelling of hydrothermal eruptions in general.

- I would like to thank the staff in the Institute of Fundamental Sciences, particularly those in the Mathematics Discipline, for creating a friendly and supportive environment in which to work.

- I am also grateful to my fellow mathematics graduate students for their invaluable contributions to the sanity of the author. In particular, I would like to thank Chris Palliser, Nick Allsop, Anton Raviraj, Mary Day, Mark Johnston, Tracey Flux, and Deborah Kelly. It's been fun.

- Thanks to Mark Johnston for the help he has given me in all things LaTeX.

- The physical experiments detailed in Sections 2.2 and 5.3 were done with funds provided by the Massey University Graduate Research Fund, the contribution of which is gratefully appreciated.

- Thanks are due to Sarah Codd for her assistance with the NMR experiments and interpretation. I would also like to thank the Institute of Fundamental Sciences workshop staff, in particular Noel Foote and Grant Platt for their help with the design and construction of experimental work.

- Thank you to Massey University for the Doctoral Scholarship and to the Mathematics Department and later the Institute of Fundamental Sciences for the Graduate Assistant and Casual Assistant work. This financial assistance and teaching experience is very much appreciated.

- Thanks Mom and Dad for starting me on this journey many years ago and for the innumerable kindesses (love, support, unwavering belief in me, financial aid in times of need) that have always sustained me.

- Finally, this thesis is dedicated with infinite appreciation and love to my husband, Brian. Thank you for bringing your smile into my life.

Nomenclature

All constants and variables used in this thesis are defined when they first appear in the text. Commonly used notation is summarized here. Units are as given below unless otherwise stated within the text.

Roman

A_e	energy per unit volume of formation, Jm^{-3}
A_m	fluid mass per unit volume of formation, $kg\ m^{-3}$
c	heat capacity, $Jkg^{-1}K^{-1}$
c_F	Forchheimer coefficient, *dimensionless*
$\mathbf{e}_r$, $\mathbf{e}_\theta$	unit vectors in the r, θ directions respectively, *dimensionless*
$\mathbf{g}$, g	acceleration due to gravity, ms^{-2}
h	specific enthalpy, Jkg^{-1}
k	permeability, m^2
k_{rg}, k_{rl}	relative permeability of the gas, liquid phases respectively, *dimensionless*
K	thermal conductivity, $Wm^{-1}K^{-1}$
p	pressure, Pa
$\mathbf{Q}_e$	energy flux per unit area, $Jm^{-2}s^{-1}$
$\mathbf{Q}_m$	mass flux per unit area, $kg\ m^{-2}s^{-1}$
r	radial coordinate, m
S	liquid saturation, *dimensionless*
t	time, s

T	temperature, K
u	specific internal energy, Jkg^{-1}
$\mathbf{u}$	pore-averaged velocity, ms^{-1}
$\mathbf{v}$	volume flux per unit area (Darcy velocity), ms^{-1}
$\mathbf{w}$	phase-averaged velocity, ms^{-1}
x	horizontal coordinate, m
z	vertical coordinate, m

Greek

$\eta = x/\sqrt{t}$	similarity variable, $ms^{-1/2}$
θ	angular coordinate, *radians*
μ	dynamic viscosity, $kg\ m^{-1}s^{-1}$
$\nu = \mu/\rho$	kinematic viscosity, m^2s^{-1}
ρ	density, $kg\ m^{-3}$
ϕ	porosity, *dimensionless*
Φ	velocity potential function, *units dependent on coordinate system*
Φ_m	specific mass flux potential function, *units dependent on coordinate system*
Ψ	velocity stream function, *units dependent on coordinate system*
Ψ_m	specific mass flux stream function, *units dependent on coordinate system*

Subscripts

f	fluid mixture
f	condition placed on the boundary $\eta = 0$ in the numerical experiment described in Section 5.2
i	condition placed on the boundary $\eta \to \infty$ in the numerical experiment described in Section 5.2
l	liquid phase
r	rock matrix
v	vapour phase
t	partial derivative with respect to time t
x	partial derivative with respect to horizontal distance x

Superscripts

$',''$	first and second derivatives with respect to similarity variable η

Table of Contents

CHAPTER 1

Introduction

Hydrothermal eruptions are violent events driven by the expansion of hydrothermal fluids. Without warning, they eject large volumes of rock particles mixed with liquid water, water vapour and other gases. (See Figure 1.1.) They last from minutes to several hours over which time showers of ejecta are thrust intermittently to varying heights and thrown over areas which may be anywhere from a few square metres to as large as 12 km^2. Material is ejected from depths of up to 450 m. This event alters the surroundings of the area in question, leaving craters ranging from 2 to 500 m across. (See Figures 1.2 and 1.3). Trees may be felled and surrounding foliage scorched. People have been injured or killed and property damaged.

Though rare temporally, hydrothermal eruptions have occurred around the world and they are typical features of many geothermal fields in New Zealand. Figure 1.4 illustrates some areas in which hydrothermal eruptions have occurred while Figure 1.5 details sites of hydrothermal eruptions in the North Island of New Zealand.

Hydrothermal eruptions have been naturally occurring phenomena in the history of many geothermal systems. However, the effects of exploitation of geothermal fields for energy production induce changes in the pressures and temperatures in near-surface regions where risks to life as well as engineering structures are increased in an as yet unquantified way. The sites of recent hydrothermal eruptions such as Craters of the Moon, Waimangu and Waiotapu are now also common tourist sites. In order to reduce the risks to life and property, the problem of understanding this hazard phenomenon becomes an important one. The more we learn about these events through the application of modelling techniques, the better any assessment of the risks.

The development of a complete mathematical model of the hydrothermal eruption process is beyond the scope of this thesis. This thesis aims, instead, to add to the

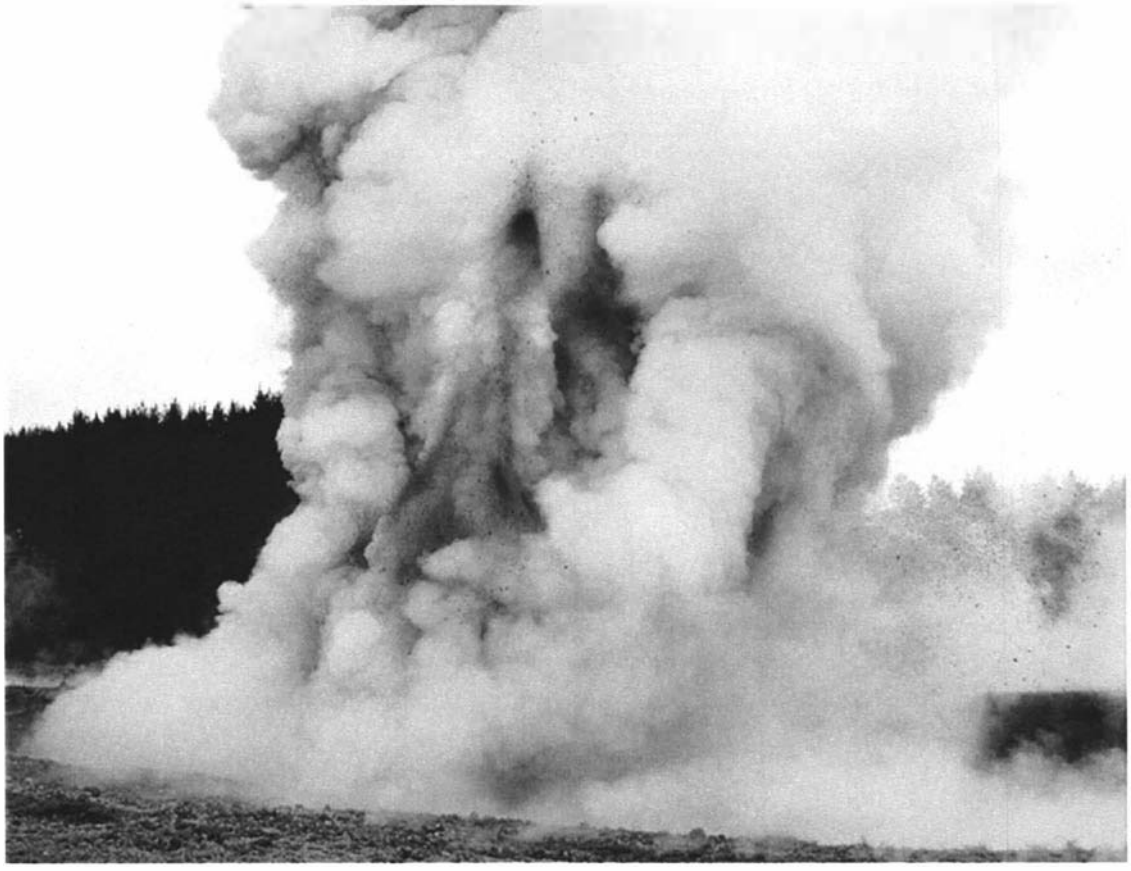

Figure 1.1: Hydrothermal eruption which occurred at Craters of the Moon, Karapiti Thermal Area of Wairakei Geothermal Field, New Zealand on April 17, 1989. Photograph taken by Craig Potton (Potton and Woods 1990).

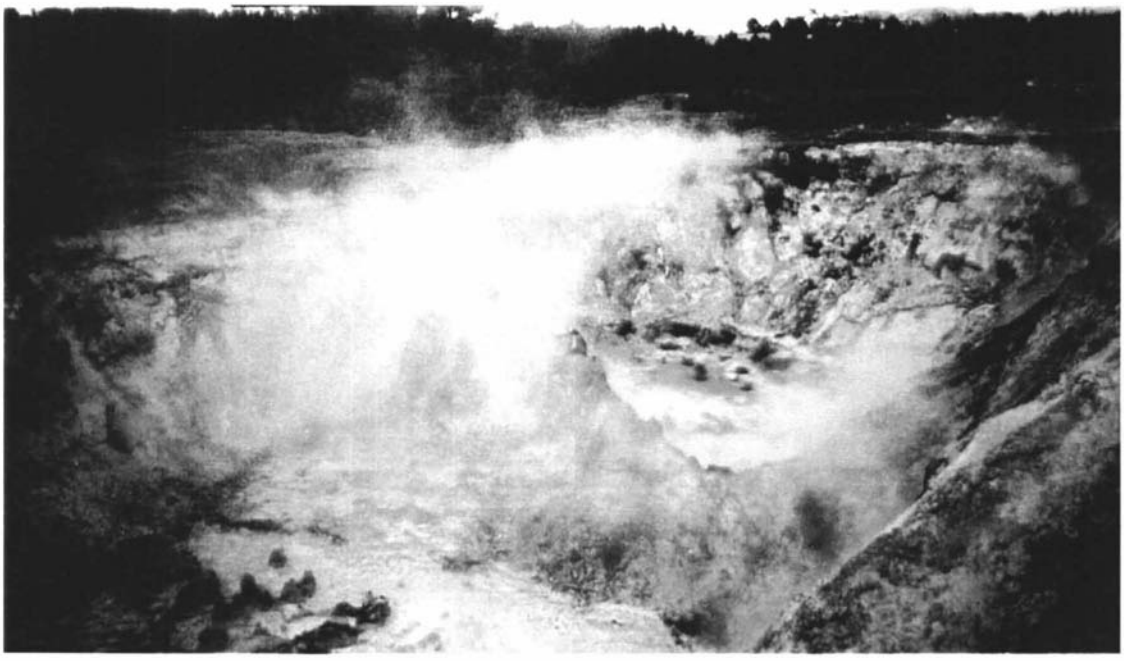

Figure 1.2: Hydrothermal eruption crater, Craters of the Moon, Karapiti Thermal Area, Wairakei Geothermal Field, New Zealand. Site from which the hydrothermal eruption pictured in Figure 1.1 occurred as well as at least five other eruptions before it.

Figure 1.3: Overhead view of hydrothermal eruption crater, Craters of the Moon, Karapiti Thermal Area, Wairakei Geothermal Field, New Zealand. View inside crater is shown in Figure 1.2.

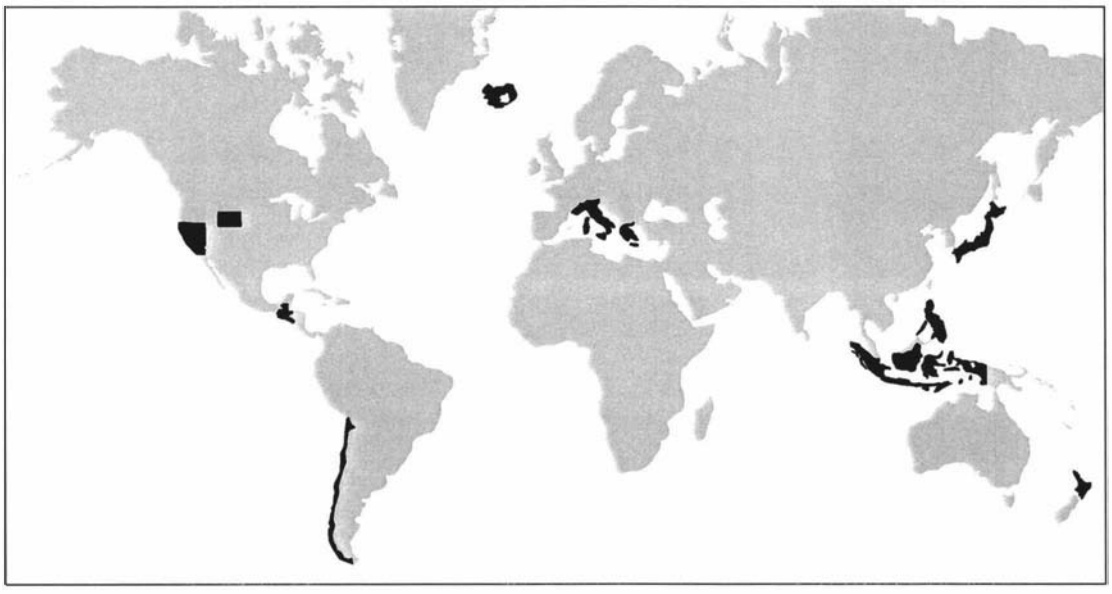

Figure 1.4: Map illustrating some areas in which hydrothermal eruptions have occurred around the world. Some specific sites of hydrothermal eruptions are listed in Tables 1.1 and 1.2. A more comprehensive list of hydrothermal eruption sites may be found in Browne and Lawless (in press).

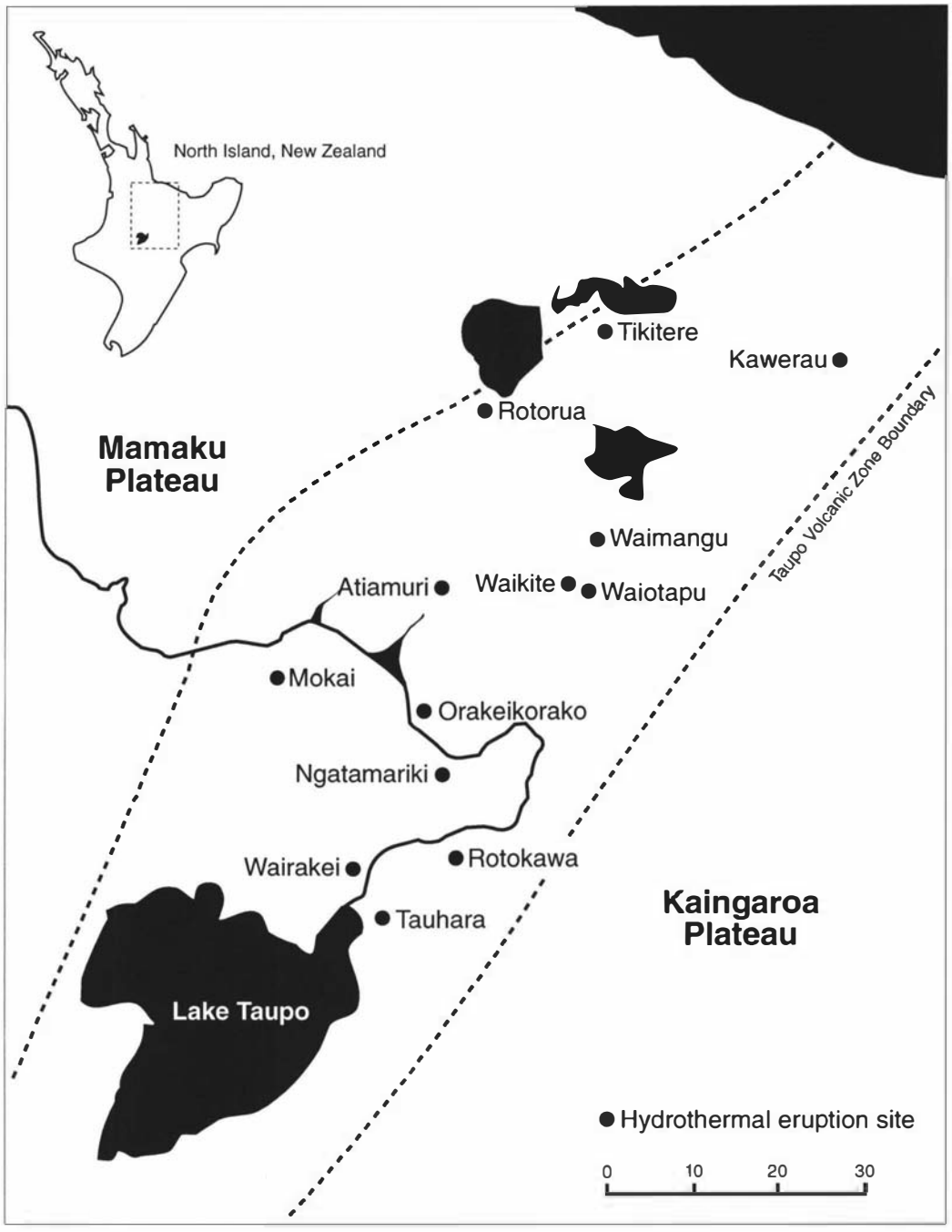

Figure 1.5: Map illustrating sites of New Zealand hydrothermal eruptions. Adapted from Collar (1985).

understanding of the underground flow processes involved, in particular to the transient boiling processes in porous media which drive the eruption. A conceptual model for hydrothermal eruptions is put forward which describes the progression of a boiling front as it moves through the porous medium. Physical and numerical experiments have been carried out to investigate the behavior of these fronts. In previous mathematical models, the assumption that the underground fluid involved flows as a single homogeneous (two-phase) mixture was made. In this thesis, an examination of the differences between the progression of the front under the assumptions of homogeneous (two-phase) mixture flow and separable two-phase flow is given. An investigation of the isothermal case is also provided, giving some insight into the possible recharge of the system following an eruption.

1.1 Background

Of the multitude of eruptions which have played a role in the shaping of the earth, most can be classified into one of the following three types of eruptive processes: magmatic, phreato-magmatic or steam-blast. Magmatic eruptions are ventings due to depressurization of molten rock which contains water and gases in varying concentrations. In contrast, phreato-magmatic eruptions eventuate when rising magma comes into contact with large amounts of groundwater or sea-water. The term steam-blast eruption is used to describe a variety of eruptive types whose common factor is that they do not expel juvenile rock.

Many names and types of steam-blast eruptions have been discussed in the literature. They have been classified in terms of the types of erupting fluid, the initial temperatures of erupting fluid, the amount of solid debris ejected and the cause of eruption. As each of these factors is not always clear, a rigid classification of eruptive types may not be possible. An attempt is made, however, in Figure 1.6, to give a general distinction between the different kinds of steam-blast eruptions.

The driving fluid of non-juvenile eruptions is either gas or heated groundwater. If it is gas, or superheated water vapour at initial temperatures approaching magmatic, the eruption is called a gas eruption. The eruption of exsolved gas and solid debris on the Mount St Helens lava dome in 1983 is an example of a gas eruption (Mastin 1995). If the driving fluid is heated groundwater which is predominantly meteoric in origin, the eruption is termed phreatic.

One type of phreatic eruption is the mixing eruption. These are caused by the mixing of groundwater with hot rock. They may occur when large amounts of groundwater flow into a collapsed eruptive conduit. This was the case at Halemaumau crater, Kiluea

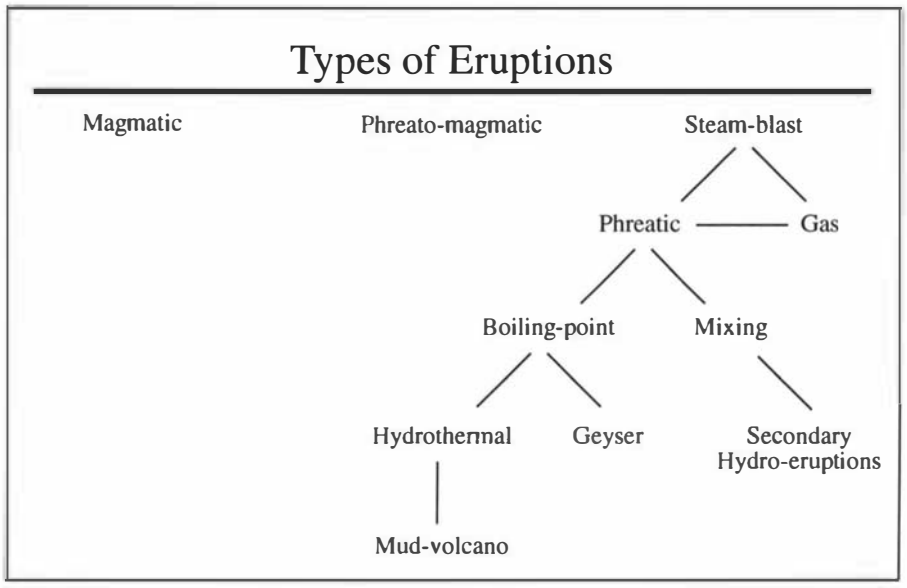

Figure 1.6: Chart of eruptive types. A general classification of steam-blast eruptive types is given.

Volcano, Hawaii in 1924, when large amounts of groundwater flowed into the crater following the drainage of a lava lake. The mixing of this water with hot country rock caused up to thirteen eruptions a day over a period of eighteen days (Mastin 1995). Mixing eruptions may also occur when erupted volcanic debris comes into contact with ground or surface water. These rootless eruptions are known as secondary hydroeruptions (Mastin 1995). Several such eruptions took place in Alaska following the volcanic eruption of Novarupta in 1912. In this case, a blanket of hot ash several metres deep was thrown over the surrounding valley, sealing in water from creeks and glacial streams. Over the next several years, this water resurfaced through vents as superheated steam in the form of secondary hydroeruptions, fumaroles and mud pools. (See Figure 1.7.) During this time the area was renamed the Valley of 10,000 Smokes (NGT 1994).

Another type of steam-blast eruption is the boiling-point eruption. These are driven by water which is liquid, or two-phase with high liquid saturation, initially at boiling-point temperatures. Unlike mixing eruptions, these eruptions are in-situ. Hydrothermal eruptions and geysers are both boiling-point eruptions.

The term hydrothermal eruption is used to imply fluids from a pre-existing hydrothermal system are involved. They are driven by the expansion of hydrothermal fluids to atmospheric pressure (Lloyd 1959). They are distinct from geysers in that they are not cyclic and eject relatively large amounts of non-juvenile rock. Other names which have

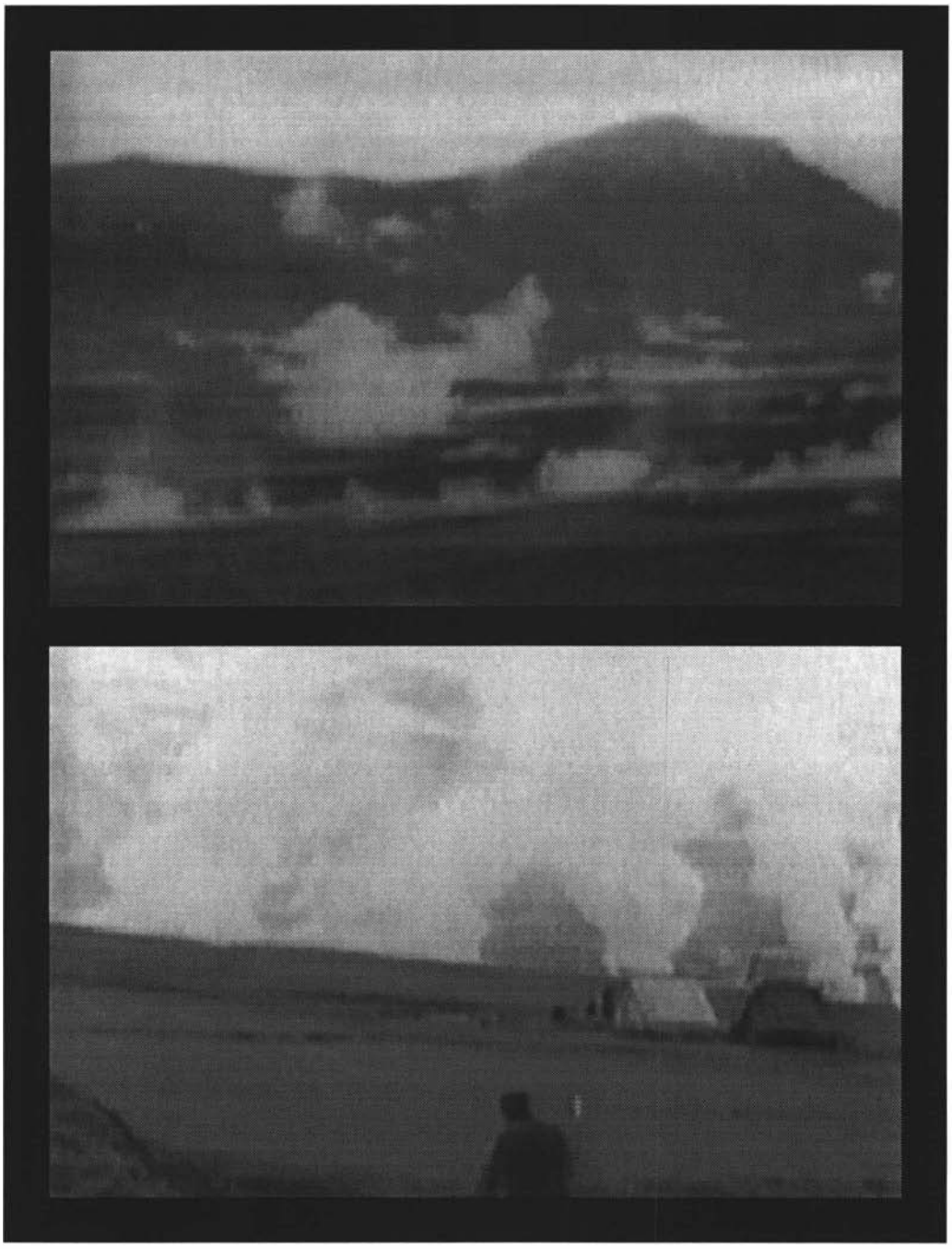

Figure 1.7: Secondary hydroeruptions in the Valley of Ten Thousand Smokes, Alaska, USA. Video stills taken from National Geographic Television (NGT 1994).

Figure 1.8: Eruption of the Waimangu Geyser, Waimangu, New Zealand in March 1903. Photograph taken by C. Shepherd (Shepherd 1903).

been used in the literature to describe such events include hydrothermal explosion and phreatic eruption. There are eruptions, such as mixing eruptions, which are phreatic but not hydrothermal; hence the term hydrothermal is more specific. The term eruption is used here instead of explosion in recognition of the fact that a hydrothermal eruption is an ongoing process, lasting from minutes to several hours, as opposed to a process in which material is thrown out in one large "explosion" as is the case in certain chemical or nuclear reactions. Mud-volcanoes, as described by White (1955), are one type of hydrothermal eruption. They expel a muddy mixture of steam, gas and fine solid debris. They may have been mud pools before or after eruption, but this is not necessary.

Geysers are hot-water eruptions in which steam and boiling water are expelled periodically. Unlike most other types of steam-blast eruptions, they do not eject any significant amount of solid debris. Models of these have been well studied and can be found in, for example, Anderson et al. (1978) and Dowden et al. (1991). A history of geyser theory including descriptions of several geyser models is presented in Luketina (1995).

As stated at the beginning of this section, it is not always clear where certain eruptions fit into the scheme illustrated in Figure 1.6. One such example is the Waimangu Geyser. This vent erupted periodically, in a 36-hour cycle, between 1900 and 1904. The periodicity of its eruption is typical of a geyser. However, it ejected large amounts of solid debris to heights of up to 450 m. (See Figure 1.8.) This would be more characteristic of a

hydrothermal eruption.

1.2 Previous work

The process of trying to model hydrothermal eruptions is a difficult one. Precursors for such events are unknown, making it impossible to know when and where the next one might occur. Consequently, few hydrothermal eruptions have been observed directly, making for a lack of insight due to close observation. Because of this, and the fact that many such eruptions are prehistoric, most have been studied only after the fact, and many have been studied hundreds or even thousands of years later. Written documentation describing particular hydrothermal events is rare. Thanks to Scott and Cody (1982), Allis (1983), Lloyd and Keam (1974) and Bruno et al. (1992), however, we do have a few well-documented recent cases. The rarity of the occurrence of hydrothermal eruptions also makes data collection and documentation of the events difficult. Because of these limiting factors, many assumptions about the eruptive process must be made. The fields of geology, geophysics, geochemistry, thermodynamics, and mathematics have provided some information about these eruptions, but there is still much that is to be determined.

1.2.1 Models of prehistoric hydrothermal eruptions

Many prehistoric eruptions were sizeable, leaving craters as large as 300 m in diameter, ejecting material from depths of up to 450 m, and depositing ejecta up to 40 m thick over areas as great as 12 km^2. Sites of some prehistoric hydrothermal eruptions are given in Table 1.1.

One of the more substantial efforts on the modelling of prehistoric eruptions was tackled by Browne (1986), Collar (1985) and Collar and Browne (1985); their reports summarize the hydrothermal eruption history of the Rotokawa Geothermal Field, New Zealand over the past 20,000 years. At least 8 hydrothermal eruptions were found to have occurred during that period, with the latest occurring about 3700 years ago. It is likely that there were more eruptions, but the deposits of those which occurred relatively close to one another in time may not be separated by a paleosol or tephra and hence may not be noticed as having come from separate events. Tephrochronology and carbon dating (of wood found in the deposits) were used to estimate the dates of various events. The texture and distribution of eruptive deposits is used to estimate possible vent locations. Areas in which the deposit is thicker and the fragments are larger, are assumed to be closer to the vent. However, it is noted that if the eruption has a preferred direction, or if significant amounts of erosion have occurred since the event, thickness of deposit may not be useful. In some cases the direction of felled trees may also indicate vent location.

Table 1.1: Examples of Prehistoric Hydrothermal Eruptions

Location	Reference
Kawerau, NZ	Nairn and Wiradiradja (1980)
Mokai, NZ	Collar (1985)
Orakeikorako, NZ	Lloyd (1972)
Rotokawa, NZ	Browne (1986), Collar (1985)
Tikitere, NZ	Espanola (1974)
Upper Atiamuri, NZ	Browne (1986)
Waikite, NZ	Collar (1985)
Waiotapu, NZ	Cross (1963), Hedenquist and Henley (1985)
Whakarewarewa, NZ	Collar (1985)
Nisyros, Dodecanese, Greece	Marini et al. (1993)
Yellowstone National Park, Wyoming, USA	Wold et al. (1977), Muffler et al. (1971)

The size and the shape of the vents were examined. It is thought that some of the vents may be larger than 250 to 300 m in diameter and that their depths may be up to 450 m. The depths of the vents are determined by examining the types of ejecta. It is noted that these depths may in some cases be deceiving as it is possible for an eruption to re-eject earlier ejecta. Browne (1986) also gives a historical overview of occurrences of hydrothermal eruptions in New Zealand.

1.2.2 Models of recent hydrothermal eruptions

Recent hydrothermal eruptions may be classified as either natural or induced. Natural eruptions include those which are prehistoric and also those historic eruptions which occur in unexploited fields. Induced eruptions are those which occur due to the exploitation of a geothermal field. As induced eruptions occur in areas frequented by people, they are more likely to be witnessed, or the aftermath of the eruption seen soon after. Hence many of the well-documented recent eruptions are of this type. They tend to last from minutes to a few hours, leave craters under 60 m in diameter, and eject material from depths of under 20 m over areas less than 100 m from the vent. Table 1.2 gives examples of sites of historic eruptions.

Lloyd and Keam (1974), Allis (1983), Scott and Cody (1982) and Bruno et al. (1992) give detailed descriptions of hydrothermal eruptions which have occurred in the last 30 years. The settings for these eruptions are varied. Waimangu is a geothermal field recently reconfigured by the volcanic eruption of Tarawera; Craters of the Moon and Agua Shuca are fields which have undergone large changes in activity with the nearby extraction of water for geothermal power; Tauhara is an old geological field. The Trinity Terrace eruption occurred in a lake; the Craters of the Moon eruption occurred in the bottom of a pre-existing crater; the Agua Shuca and Taupo Pony Club eruptions did not occur in either. The Craters of the Moon, Taupo Pony Club, and Agua Shuca eruptions were induced, while the Trinity Terrace eruption was natural. However, despite the variety of settings, the eruptions described in the above articles have similar characteristics. Some details on the scale of these eruptions are provided below. Details taken from these reports on possible triggers for these eruptions, what an eruption looks like in progress, and on how the surrounding area appears immediately after an eruption, were used in forming the conceptual model described in Chapter 2.

In 1981 a hydrothermal eruption occurred near the Taupo Pony Club in the Tauhara Geothermal Field, New Zealand. Eyewitness accounts of the eruption indicate its column reached heights of over 100 m. A detailed study of the site by Scott and Cody (1982) determined that material was ejected from depths of between 15 to 20 m, forming a crater

Table 1.2: Examples of Historic Hydrothermal Eruptions

Location	Type	Reference
Craters of the Moon, NZ	Induced	Allis (1979, 1983)
Ngatamariki, NZ	Natural	Brotheridge et al. (1995)
Rotorua, NZ	Induced	NZHerald (2000), Dominion (2000)
Tauhara, NZ	Induced	Scott and Cody (1982)
Waimangu, NZ	Natural	Lloyd and Keam (1974), Morgan (1917)
Whakarewarewa, NZ	Induced	Browne (1986)
Agua Shuca, Ahuachapan, El Salvador	Induced	Bruno et al. (1992)
Lake City Hot Springs, California, USA	Natural	White (1955)
Imperial County, California, USA	Natural	White (1955)
Nakano-Yu, Japan	Induced	Yuhara (1997)
Nisyros, Dodecanese, Greece	Natural	Marini et al. (1993)
Tiwi, Philippines	Induced	Grindley (1982)
Washoe County, Nevada, USA	Natural	White (1955)
Zunil, Guatemala	Induced	Goff and Goff (1997)

of area 1640 m^2 with a maximum depth of 4.5 m. The volume of material ejected was approximately 6800 m^3. Fine debris was distributed over an area 800 m from the vent while blocks greater than 1.2 m in diameter were confined to within 20 m of the vent. Average velocities of ballistic ejecta were estimated to be around 90 ms^{-1} indicating ejecta was thrown to maximum heights of approximately 70 m. Vegetation within 80 m of the crater was totally buried, a row of young pine trees between 70 and 80 m from the vent were felled and fencing wire approximately 90 m from the crater was broken when struck by ballistic blocks. An absence of gypsum found in ejecta indicates temperatures for the erupted material were greater than $40°C$ while an absence of quartz formation implies temperatures were also less than $140°C$.

At least 20 hydrothermal eruptions have taken place at Craters of the Moon, Karapiti Thermal Area of Wairakei Geothermal Field, New Zealand in recent years (Allis 1979; Allis 1983). One such eruption in 1983 was witnessed and well-documented (Allis 1983). It occurred from a crater in which at least four previous eruptions were known to have occurred, increasing the maximum depth of the crater from 10 to 15 m while leaving the area of the crater (1000 m^2) approximately the same. The height of the eruption was witnessed to be between 50 and 100 m. Ejecta was thrown to heights of 35 to 60 m with an estimated vent velocity of 30 to 40 ms^{-1}. Fine ejecta was thrown as far as 120 m from the vent, while coarse ejecta was thrown only as far as 50 m. The volume of material ejected was estimated to be between 1000 and 2000 m^3.

The Waimangu Valley is another common site for hydrothermal eruptions in New Zealand. The Waimangu Geyser, as mentioned in Section 1.1, erupted several times between 1900 and 1904. Though periodic in nature, each eruption of the geyser had characteristics consistent with those of a hydrothermal eruption. The largest hydrothermal eruption in the Waimangu area occurred in 1917 in Echo Crater. It lasted for 3 days (Lloyd and Keam 1965) forming new craters, which over the following year filled with warm water to form what is now Frying Pan Lake. Two people were killed in this eruption and a building 600 m from the vent was destroyed (Scott 1992). The best documented eruption at Waimangu is the Trinity Terrace eruption of 1973 (Lloyd and Keam 1974). This eruption occurred through Frying Pan Lake at night and was not witnessed. Stream flow records from the Hot Water Creek gauging station show the effects of the eruption and indicate its duration was at least 15 minutes. Nearby vegetation was killed, scalded or stripped of foliage and a boardwalk located on the tourist path was destroyed. Investigations of the area by Lloyd and Keam following the eruption show the area of Frying Pan Lake was increased by 285 ± 15 m^2. The total volume of ejecta thrown was approximately 970 ± 150 m^3, with 190 ± 20 m^3 being thrown on land over an area of 3000 m^2 to a maximum thickness of 0.45 m. The depth of the eruption was estimated to

be less than 90 m and its height greater than 42.5 m. Examination of ejecta indicated it was likely that some material erupted at temperatures exceeding $100°C$. Ejected blocks as large as 0.3 m in diameter were common.

Agua Shuca, in the Ahuachapan Geothermal Field, El Salvador has been a site of several mud-volcanoes as well as at least two other hydrothermal eruptions. One of these eruptions occurred in approximately 1868 and the other in 1990. Details of the 1990 eruption are described in Bruno et al. (1992). This eruption threw 1600 m^3 of ejecta over an area of $10,000$ m^2, killing 25 people and injuring 15. Several nearby huts were also damaged or destroyed. The crater formed by the eruption was approximately 40 m in diameter and 5 m deep.

Details of mud-volcanoes in the southwestern United States and Baja California are given in White (1955). The area of greatest activity described is Lake City Hot Springs where on March 1 and 2, 1951 four or five large mud-volcanoes (20 - 60 m diameter) as well as several smaller ones erupted concurrently. This event significantly altered an area of approximately $81,000$ m^2. Material was thrown to heights of over 1500 m and fine debris was found further than 7 km to the southeast.

Other examples of recent hydrothermal eruptions include the eruption which occurred in the Zunil I Geothermal Field, Guatemala in 1991 and the recent eruptions in January, 2000 in Rotorua. In both of these cases hot water features were covered with soil, resulting in eruption. In the Guatemalan eruption, a landslide buried a production well in the geothermal field. Hot liquid or two-phase water escaping from the well threw the newly-created overburden over the surrounding area (Goff and Goff 1997). In Rotorua approximately two years after a mud pool had been filled in with soil, it erupted, ejecting boiling mud to heights of 13 m over an area with a radius of 5 m from the vent. The fence surrounding the pool was destroyed in the event (NZHerald 2000). Housing which had existed within the area hit by boiling mud had just been removed a couple of years earlier due to the eruption of a rogue geyser. With this latest eruption, residents of nearby houses were fearful for the safety of their property. This eruption was followed within a week by another eruption only metres away; this second eruption lasted for approximately 15 minutes (Dominion 2000).

Examples of many of the hydrothermal eruptions which have occurred, prehistoric and historic, including those listed above and some which are likely phreato-magmatic in origin, are given in a summary paper by Browne and Lawless (in press).

1.2.3 Mathematical models of hydrothermal eruptions

To date, there are two different approaches to the mathematical modelling of hydrothermal eruptions. One approach (Mastin 1995) uses estimates of the energy available and released in such events to provide magnitudes of the mass of material moved and spatial distribution of the debris. The other approach (Bercich and McKibbin 1992; McKibbin 1990, 1996) is a more mechanistic approach using local conservation laws to model the way a particular eruption might proceed.

In Mastin's (1995) approach, thermodynamic concepts are used to estimate the mechanical energy released during an eruption as well as the final temperature, mass fraction of steam, and maximum theoretical velocities of ejecta. He concludes that the higher the mass fraction of rock in the erupting water/rock mixture, the greater the percentage of liquid water converted to steam, and the higher the final temperatures of the ejecta. On the other hand, the lower the mass fraction of rock in the erupting water / rock mixture, the higher the energy release, and the higher the maximum theoretical velocities.

If the mass fraction of rock is less than 0.95, the maximum theoretical velocities calculated by Mastin (1995) are higher than has ever been observed. Reasons given for why this may be the case are as follows. During an eruption, much of the solid debris is ejected early on in the process. The fluid ejected towards the end is nearly free of solid debris. Velocities have usually been calculated from ballistic fragments and would therefore better describe the velocity of the fluid towards the beginning of the eruption than at the end. Choked flow and frictional flow may also be responsible for differences in observed and theoretical maximum velocities.

McKibbin (1990, 1996) and Bercich and McKibbin (1992), describe one-dimensional vertical models of near-surface fluid escaping to atmospheric conditions. The resultant depressurization allows the fluid below to boil. A boiling front moves down into the formation while solid material is ejected from the erosion surface. These models focus on the underground movement of the boiling fluid rather than the above-ground flight of ejected material. In each model, the process is modelled as quasi-steady (that is, it is assumed that the eruption is already in progress.)

In McKibbin (1990) and Bercich and McKibbin (1992) the fluid is assumed to be two-phase water which, due to the rapidity of the flow, flows as a single homogeneous mixture. The first model (McKibbin 1990) assumes the simple Darcy's Law holds and that the erosion of the surface and flashing front move downwards at the same constant speed. Under these assumptions, it was concluded that the progression of the boiling front would be slower in reservoirs with higher liquid saturations. The effect of this would be eruptions of longer duration. It was also determined that the thickness of the

boiling zone was approximately inversely proportional to the speed of the boiling front.

In Bercich and McKibbin (1992), the motion of the flashing front and the erosion surface, and the distance between them, was examined. It was found that both the eroding surface and boiling front decelerate with time; however, in contrast to the assumption of the first model by McKibbin, this model determined that the eroding surface slows down at a faster rate than the boiling front. In other words, the thickness of the boiling zone increases with time. The thickness of this zone was also shown to be affected by varying cohesive rock stresses; an increase in cohesion gave a thinner boiling zone. Bercich and McKibbin also investigated the effects of adding a non-linear drag term (the Forchheimer term) to the conservation of momentum equation. Results showed that for permeabilities of $1 \times 10^{-12}\ m^2$ (≈ 1 Darcy) or less, the effects of the term were negligible and the simple Darcy's Law provided good approximations. However, for larger permeabilities the Forchheimer term should be used.

In McKibbin (1996) the effects of the geothermal fluid containing significant amounts of non-condensable gas (in particular CO_2) were considered. While it was shown that the presence of CO_2 affected fluid properties most in systems with low liquid saturation, the speed of the boiling zone was also reduced most in these regions. While the initial temperature at which the erupting fluid will begin to boil is affected by the non-condensable gas content, McKibbin concluded that further work was needed to determine whether or not the likelihood of hydrothermal eruption in a liquid-dominated system was increased by the presence of moderate amounts of non-condensable gases.

1.3 This work - an outline

Each of the publications described in Section 1.2 adds new insight into the problem of modelling hydrothermal eruptions. A "complete" hydrothermal eruption flow model, however, is a distant goal and beyond the scope of this thesis. The objective of this work is to help further the understanding of the underground flow and boiling processes involved in hydrothermal eruptions. Ideas presented in previous modelling experiences are synthesized to form a conceptual model which is then used to formulate a mathematical model for the problem. The mathematical model is solved under various simplifying assumptions. Results obtained in some cases are compared to physical experiments and numerical simulations using a groundwater flow and heat transport simulator.

The conceptual model used in this thesis is formed in Chapter 2. It describes a downward moving boiling front which is initiated by a pressure reduction at the surface. A laboratory model of a hydrothermal eruption has been constructed. Observations from the laboratory experiment provide qualitative results which support the conceptual

model and the proposed triggering mechanism.

Chapter 3 formulates the problem of modelling the underground boiling processes in hydrothermal eruptions using the principles of conservation of mass, momentum and energy. The conservation equations and boundary conditions describing the flow in a hydrothermal eruption are outlined. Two flow models based on differing assumptions about the fluid flow regime are described. In the first model, it is assumed that the fluid is moving so rapidly that separable two-phase flow does not have time to eventuate and the flow is modelled as a single homogeneous mixture. In the second model, the two-phases are modelled as flowing separately.

Methods for solving the system of equations detailed in Chapter 3 are investigated in Chapter 4 for the (simpler) steady isothermal flow case. Results are given for three different geometrical configurations, and, in each case, the flow is quantified. While in a hydrothermal eruption full steady-state flow will not be established, solutions obtained from this isothermal case provide insights into the origin of hydrothermal eruption fluid and into the recharge of the system following an eruption. For two of the three cases studied, numerical solutions were also compared to analytic results and excellent agreement was obtained. The numerical method used for plotting streamlines in these cases, may eventually prove to be a useful tool in solving the non-isothermal case. Comparisons of numerical results to calculations from a groundwater flow simulation also suggest the possibility of the usefulness of simulators for further investigation into the non-isothermal case.

In Chapter 5, the process which drives the hydrothermal eruption, the boiling of water, is studied. The behavior of a "boiling front" as it moves through the porous medium is investigated through both numerical and physical experiments. Under the assumption that the flow is in one horizontal dimension and that the porous medium is semi-infinite in length, a solution to the system of equations outlined in Chapter 3 is presented. Some of the algebraic details of the derivation of the conservation equations used for solution in this horizontal case are given in Appendix A. A set of simple correlations describing the thermodynamic properties of the liquid and vapour phases needed for solution over the temperature and saturated pressure ranges of interest were determined and are given in Appendix B. Results of calculated solutions provide insight into the implications of making either the assumption of homogeneous mixture flow [made in the models described by McKibbin (1990, 1996) and Bercich and McKibbin (1992)] or the assumption of separable phase flow [generally made in geothermal reservoir modelling and used in numerical simulators such as HYDROTHERM (Hayba and Ingebritsen 1994) and TOUGH2 (Pruess 1991)]. A set of laboratory experiments have been carried out for comparison with results from our numerical models. While qualitative results for these models are similar, more

investigation is needed to obtain quantitative agreement. Numerical simulations using HYDROTHERM provide insights into certain aspects of the physical experiment that are a result of the finiteness of the core. Results from our separable phase flow model were also compared with HYDROTHERM simulations and a good agreement between the two numerical solutions was found for early time periods. The effects of the finiteness of the core in the numerical solution do not allow for comparison with the semi-infinite similarity solution in later time periods.

A summary of results and suggestions for future work are given in Chapter 6.

CHAPTER 2

Conceptual Formulation

2.1 The conceptual model

In order to form a basis of knowledge on which to build a mathematical model, it is desirable to integrate information from throughout the literature to form a conceptual model. Many ideas have been put forward and debated in the literature. Some of these ideas are presented here and a conceptual model based on a current understanding of the literature is given.

Early models of hydrothermal eruptions described sudden "explosions" that were initiated at depth. The point at which the eruption was initiated, the focal depth, was assumed to be the deepest point from which material was ejected. It was proposed that the effective sealing of a geothermal system by mineral deposition would decrease the permeability of the rock matrix near the ground surface, preventing the upward flow of fluid, and increasing the fluid pressure in the system. When the fluid pressure at the focal depth exceeded lithostatic, brecciation would occur, lifting the rock above, and a water, steam and rock mixture would be ejected in one sudden explosion.

Evidence from geothermal fields in which hydrothermal eruptions occur, however, does not support the concept of a field-wide cap. The inspection of eruption breccia from Rotakawa by Collar (1985) found that mineral deposition was not extensive. Significant discharges of steam and water in many of the geothermal fields in which hydrothermal eruptions occur also contradicts this mechanism.

Furthermore, the concept of a single "explosion" is not supported by the documentation of recent hydrothermal eruptions. Allis (1983), Scott and Cody (1982) and White (1955) all described eruptions which lasted for a period of several minutes to days and describe material which is ejected and re-ejected in the eruptive stream. The "explosion"

model does not account for such effects.

Nelson and Giles (1985) noted that measured overpressures in fields such as Wairakei, Yellowstone and Kawerau were insufficient to trigger an eruption of any significant depth. Overpressures such as those required for hydrothermal eruptions of depths described by Collar (1985) are not likely.

The following conceptual model is the model that will be used in this thesis. It does not require overpressures and occurs over a period of time. In this model, based on one initially suggested by McKibbin (1989), it is the depressurization of fluid which initiates an eruption.

In geothermal fields susceptible to hydrothermal eruptions, liquid water, or a two-phase water mixture, lies below the surface at boiling point conditions. This fluid is then suddenly exposed to reduced pressure conditions due to some initiation event [see Figure 2.1 (a)]. There is no clear agreement on which events initiate eruption. Many such events have been suggested and a discussion on some of these is given in Section 2.1.1.

Owing to the initiation event, hot fluid is suddenly exposed to a zone of reduced pressure relative to the original saturated conditions. This pressure reduction allows boiling to occur and the fluid to expand. A common misconception is that the fluid lying below the surface boils causing an increase in the pressure and that this pressure build-up eventually causes an "explosion" that throws material upwards. This is thermodynamically incorrect. The in-situ formation liquid will not boil unless depressurization occurs. The continuation of this boiling relies on escape paths being provided. If escape paths are not provided the fluid will not boil. If escape paths are provided the fluid will move towards regions of lower pressure; in this geophysical situation, the fluid will therefore move upward towards the surface. The upward fluid velocities will provide lift to the rock particles above. If the net lift is large enough to overcome the weight and cohesive stresses of the rock, a rock and fluid mixture will be ejected upwards. The shear force, or drag, created by the upward fluid movement may also take some of the forming crater wall along with it. The fluid continues to boil as it rises and the eruption column is therefore likely to have a greater steam fraction at the top than it does towards the bottom [see Figure 2.1 (b)].

As fluid and rock are ejected upwards, the depressurization propagation path progresses downwards, causing the boiling front to continue downwards, prompting more fluid and rock to be ejected [see Figure 2.1 (c)]. Much of the material falls back into the vent and is re-ejected in the eruptive stream (Browne 1986). In general, the finer the debris the further it is thrown from the vent (Browne 1986; Collar 1985).

The continuing downward movement of the boiling front is dependent on hot-water

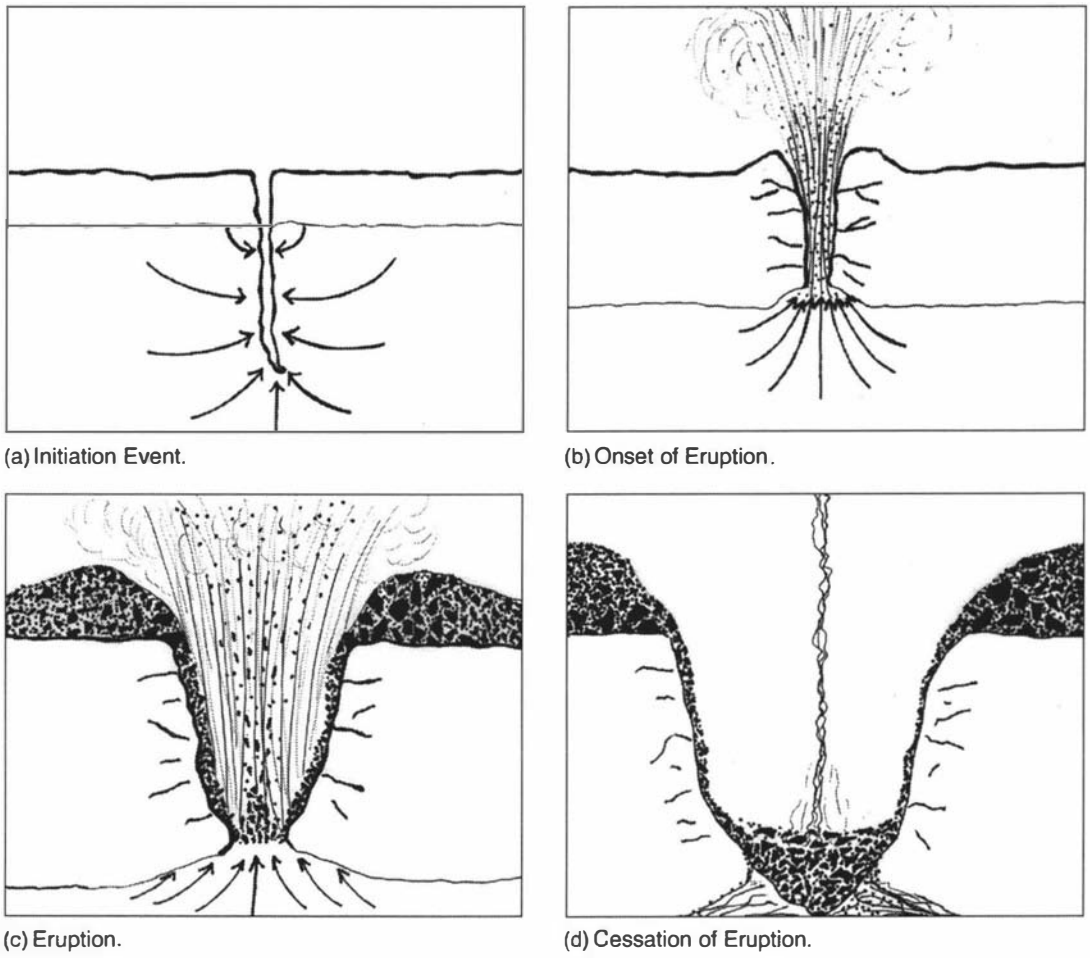

Figure 2.1: Schematic diagram of the eruptive process.

recharge or the inflow of heated water to the two-phase conduit. The front will stop progressing if it encounters a region in the rock matrix of negligible porosity or permeability.

One of the better accounts of how an eruption appears while in progress is given by Allis (1983) in his description of an eruption at Craters of the Moon in 1983. In that eruption loose pumice clasts were apparently either collapsing regularly or blocking the vent, and were then being ejected with large amounts of fluid high into the eruption column. Following the ejection of these clasts, neighboring finer debris was ejected giving rise to an eruption column which was a brown mixture of fine debris and steam at the bottom half and white steam only in the top half. Pumice clasts would again block the vent and the process would be repeated several times over. As noted in Section 1.2.3, mathematical modelling indicates that the vertical speed of the boiling front is approximately inversely proportional to the thickness of the underground boiling zone (McKibbin 1990). The re-deposition of ejecta would increase the thickness of this zone and slow the eruption.

Eyewitness accounts of the Taupo Pony Club eruption in 1981, described it as strongest immediately after its initiation, with the most violent effects occurring in the first 30 to 60 minutes. The eruption continued with decreasing vitality throughout the weekend (Scott and Cody 1982). Accounts of the 1951 Lake City Hot Springs mud-volcano eruptions also described activity as decreasing in strength over a period of days.

As an eruption continues, the pressure reduction, cooling effects, and gravitation slowing dissipate the energy of the eruption (McKibbin 1990). This causes the eruption to slow and eventually stop. As noted above, much of the erupted material falls back into, and is therefore eventually left in, the formed crater. There is possibly a muddy mixture left at the bottom of the crater and most likely residual steam still rising from the vent [see Figure 2.1 (d)]. In his description of the 1983 Craters of the Moon eruption, Allis (1983) noted that the steam output of the crater in question was unusually high immediately following the eruption, but slowly decreased with time.

Collar (1985) deduces the shape of the crater shortly after eruption to be funnel-cylindrical shaped with some of the ejecta left lying inside and fractures left along the crater walls. His assumption about the shape of the vent is based on the proportions of different sub-surface formations found in eruption breccia. It may also be possible that smaller proportions of deeper stratigraphic units were found in eruption deposits due to the fact that, as the strength of an eruption decreases with time and the depth of the crater increases with time, the strength of the eruption stream was not great enough to throw the latter ejecta any significant distance and it simply fell back into the vent.

Due to the release of formation stresses, the walls of the crater formed during the eruption will eventually begin to slump inwards. Scott and Cody (1982) noted fissures

and cracks surrounding the Taupo Pony Club eruption vent and attributed these to such slumping. The loss of significant amounts of material from under the surface may also cause the ground to subside. Allis (1983) noted the appearance of cracks and fissures in the ejecta shortly after the 1983 Craters of the Moon eruption and thought these occurred due to ground settling caused by a decrease of pore pressure or a loss of material during eruption. In this case the cracks were concentrated on one side of the crater possibly signifying a "preferential direction of depressurizing, and therefore also permeability."

It is worth noting the similarity of the schematic model described in Figure 2.1 and the field situation around an idle well that taps a hot-water aquifer. Concerns over blowouts following "initiation events" that cause a drastic lowering of the water level in the well and subsequent pressure drop and boiling in the aquifer often result in requirements for blowout preventers and casing integrity tests. Initiation events for such wells and for hydrothermal eruptions are similar and a model for one might provide insights into the other. An interesting discussion on drilling and casing problems leading to eruptions at Wairakei Geothermal Field is given by Bixley and Browne (1988). They use the term "man-made" hydrothermal eruptions to describe these events.

2.1.1 Suggested Initiation Events

Understanding the events that initiate an eruption is necessary to provide the boundary conditions for the mathematical problem. Many initiation events for hydrothermal eruptions have been suggested in the literature. Some of the suggested events are in fact initiation events in the sense that they cause the depressurization of fluid needed to initiate an eruption. These events include the removal of overburden, hydraulic fracturing, and seismic activity. Other suggested events may be better described as pre-initiation events in the sense that they do not themselves initiate eruptions but instead cause situations which exploit the instability of the system allowing a subsequent initiation event to trigger an eruption. Pre-initiation events include landslides, the collapse of post-eruptive crater walls, the sealing of a rock unit or area of mineral precipitation, climatological factors and pressure changes induced by the exploitation of a geothermal field. For most eruptions what caused the instability of the system, the pre-initiation event, may be easier to determine than the event that initiated it. The current understanding of the situation is generally confused. A short description of initiation and pre-initiation events follows.

The initiation of a hydrothermal eruption by the removal or lifting of overburden has been suggested by several authors including Muffler et al. (1971) and Dench (1988). The sudden removal of material from the top of thermal ground reduces the confining

pressure in the underlying system. If the fluid in the system was formerly at near boiling conditions, this pressure reduction will cause boiling to occur and an eruption may follow. Hydrothermal eruptions where this mechanism has been suggested include several eruptions at Yellowstone National Park, Wyoming, USA (Muffler et al. 1971) and eruptions at Wairakei Geothermal Field in New Zealand (Dench 1988). At Yellowstone during prehistoric glaciation, glacially-dammed lakes covered hydrothermal systems in the Lower Geyser Basin. Muffler et al. (1971) suggest that the sudden draining of one such lake at the Pocket Basin site during the latter stages of the Pinedale Glaciation led to a decrease in lithostatic pressure, thereby triggering an eruption. The authors also suggest that other eruptions in the Lower Geyser Basin may have been triggered in a similar manner. At Wairakei, the release of water vapour into the area over a period of time prompted a mud flow down a hillside (Dench 1988). The removal of this material resulted in a sudden decrease in confining pressure and hydrothermal eruptions ensued.

Hydraulic fracturing has been suggested as a possible initiating mechanism by, among others, Nairn and Wiradiradja (1980), Hedenquist and Henley (1985) and Nelson and Giles (1985). As stated in the conceptual model, in order for boiling to occur in a geothermal system escape paths must be provided. Hydraulic fractures which link saturated or superheated fluid to atmospheric conditions at the surface will initiate boiling and possibly trigger an eruption. Hedenquist and Henley (1985) noted that non-condensable gases may accumulate in fractures in the rock matrix. If these fractures are driven to the surface through hydraulic activity, the release of non-condensable gases to the atmosphere will decrease the fluid boiling pressures and an eruption may ensue.

The initiation of hydrothermal eruptions by seismic activity has been supported by Bixley and Browne (1988), Marini et al. (1993) and Nairn and Wiradiradja (1980), and also noted by Collar (1985), Lloyd and Keam (1974), Hedenquist and Henley (1985) and Scott and Cody (1982). Seismic activity provides another method by which fluid in higher pressure regions may be connected to lower pressure regions. It provides the escape paths in a manner similar to hydraulic fracturing and may also allow for the release of non-condensable gases. Marini et al. (1993) believe the hydrothermal eruptions which occurred in Nisyros, Greece in 1873 were initiated by fracturing due to earthquakes.

Landslides, the collapse of post-eruptive crater walls, the sealing of a rock unit or area of mineral precipitation and climatological factors have all been suggested as mechanisms which "seal off" a thermal area preventing the flow of fluid. These events provide a medium that prevents heat transport to the surface leading to high temperature gradients being set up over short distances. Any event that then connects the area just below the ground to the surface provides superheated conditions relative to the atmospheric conditions it is connected to. The landslide at Zunil Geothermal Field which buried a

production well (Goff and Goff 1997) and the filling in of a mud pool at Rotorua (NZHerald 2000, Dominion 2000) provided such unstable conditions resulting in eruptions. At Craters of the Moon, several hydrothermal eruptions occurred from a common site (Allis 1983). Following each eruption, significant amounts of steam continued to escape from the vent. Allis (1983) suggested that the collapse of a pre-existing crater wall from such a site may block steam vents sealing the thermal ground below. This would cause an unstable situation similar to that caused by other landslides. Allis (1983) also suggested the possibility of a "seal" being created due to certain weather conditions. Preceding eruptions at both the Taupo Pony Club and Craters of the Moon, months of dry weather were followed by weeks of wet weather. It was suggested by Scott and Cody (1982) that a decrease in groundwater flow due to below-average rainfall may cause an increase in steam flow to the surface. Allis (1983) suggested that if this were then followed by a period of heavy rain, an increase in near-surface soil saturation may then create an effective "seal" to the ground below. The sealing of thermal ground by a rock unit or area of mineral precipitation has also been suggested by, among others, Nelson and Giles (1985), Hedenquist and Henley (1985), Marini et al. (1993) and Bruno et al. (1992). Whether or not such a seal would be effective in preventing the upward flow of fluid, thereby providing the over-pressures necessary to initiate an eruption, has been questioned by Collar (1985) and Bixley and Browne (1988).

As noted in Section 1.2.2, many historic hydrothermal eruptions have occurred near geothermal fields exploited for energy production. Many of these eruptions, such as those at Tauhara and Karapiti near Wairakei, New Zealand, have been attributed to the changes in pressures and temperatures in near-surface regions induced by such exploitation. Declining water levels together with an increased steam flow to the surface leads to an increase in sub-surface steam pressures. This pressure increase may create the instability necessary for a subsequent initiation event to trigger an eruption. The accumulation of non-condensable gases in the upper regions of the system may further increase this instability.

2.2 Laboratory hydrothermal eruption

As described in Section 2.1, it has been hypothesized that hydrothermal eruptions occur due to a sudden pressure reduction at the surface. A depressurization of fluid initiates boiling at the surface, and a boiling front progresses downward through the porous medium. A laboratory model of a hydrothermal eruption has been constructed to test the validity of this proposed triggering mechanism and to provide visual observations of the processes that occur during an eruption.

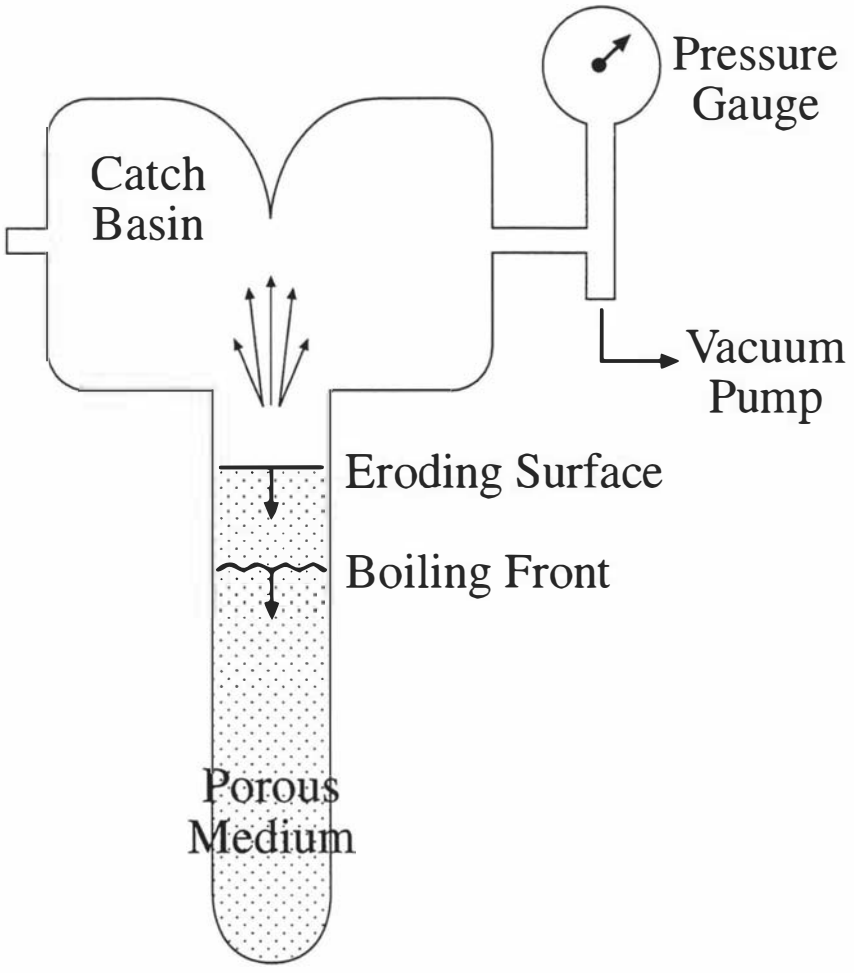

Figure 2.2: Laboratory model of hydrothermal eruption: diagram of experimental apparatus. Diagram not drawn to scale. Dimensions of eruption column: diameter 30 mm, height 325 mm. Dimensions of catch basin: diameter 75 mm, width 160 mm. The height of the porous medium placed in the eruption column was approximately 255 mm in conducted experiments.

In this model (see Figure 2.2), a Pyrex cylinder was filled with sand and the sand was saturated with liquid water. The eruption column was then placed in a hot water bath, heated to near $100°C$ and connected to a Pyrex catch basin. This basin was designed to act as a receiver for erupted material and to provide ambient conditions for the eruption. With the use of a vacuum pump, the pressure in the basin was reduced to boiling point conditions. This allowed boiling to begin at the top of the eruption column triggering the laboratory hydrothermal eruption. A boiling front was initiated at the surface, sand was thrown from the top of the eruption column and the boiling front quickly progressed downwards through the column.

Figure 2.3 contains stills taken from a video recording of a laboratory eruption in progress. Arrows have been placed on certain stills to indicate the lowest points where, from close observation of the stills, boiling appeared to have taken place. Movement of the arrows therefore indicates the progression of the boiling front. Figure 2.3 (a) illustrates what the setup looked like before the depressurization of the catch basin; the eruption column was full of sand and saturated with liquid water. Within one second of pressure reduction at the top of the column, the surface of the column had begun to rise [see Figure 2.3 (b)]. Sand was being ejected and "thrown around" at the top of the eruption column and a boiling front had begun to move downwards through the porous medium. Two seconds after the eruption began, the boiling front had progressed through more than half of the column [see Figure 2.3 (c)]. Small gaps could be seen in the sand, produced by the boiling of water and the upward movement of the sand. Between two and four seconds, a further rise of the surface was seen and the boiling front had again moved further down the column [see Figure 2.3 (d)]. Larger holes were produced by the continued upward movement of the sand. After 7 seconds the boiling front had completely moved through the column and the eruption was at its height [see Figure 2.3 (e)]. From this point on, the eruption slowed and eventually stopped. Some slumping occurred as material fell back down the eruption column [see Figure 2.3 (f)].

This experiment supports the hypothesis that a pressure reduction at the surface may trigger an eruption and initiate a downwards-moving boiling front. Physical features observed in naturally-occurring hydrothermal eruptions, including the ejection of solid material, the falling of ejected material back into the vent, the re-ejection of this material in the eruptive stream and the slumping of the ground surface following an eruption, were all observed.

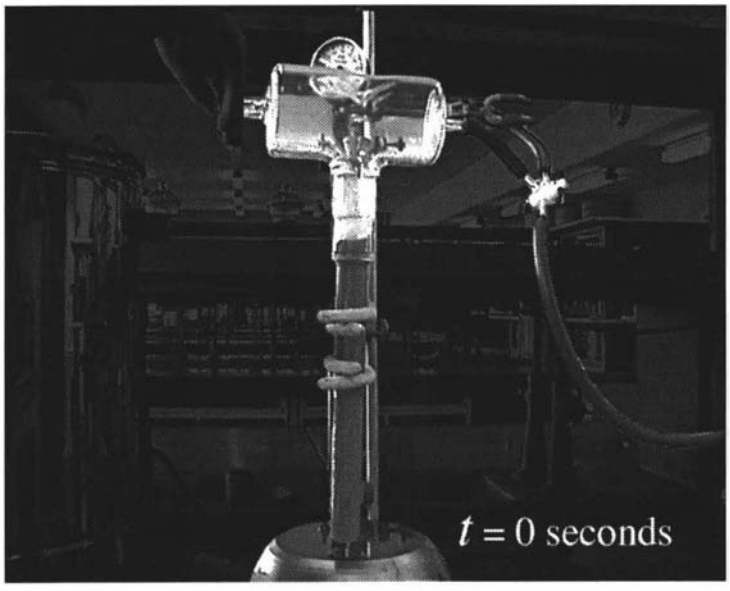

(a) 0 seconds

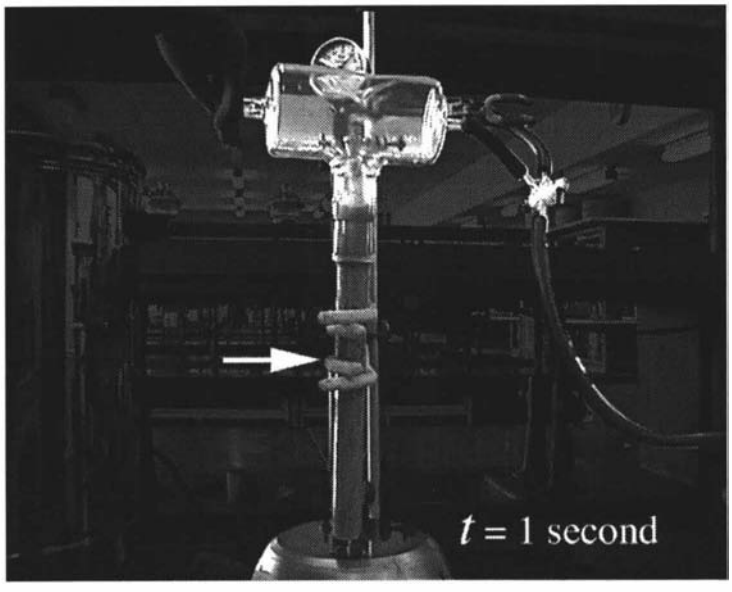

(b) 1 second

Figure 2.3: Laboratory hydrothermal eruption in progress.

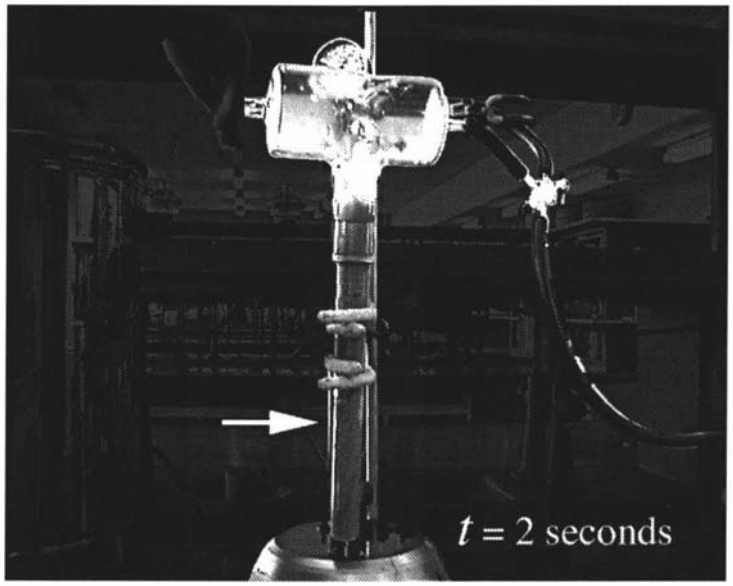

(c) 2 seconds

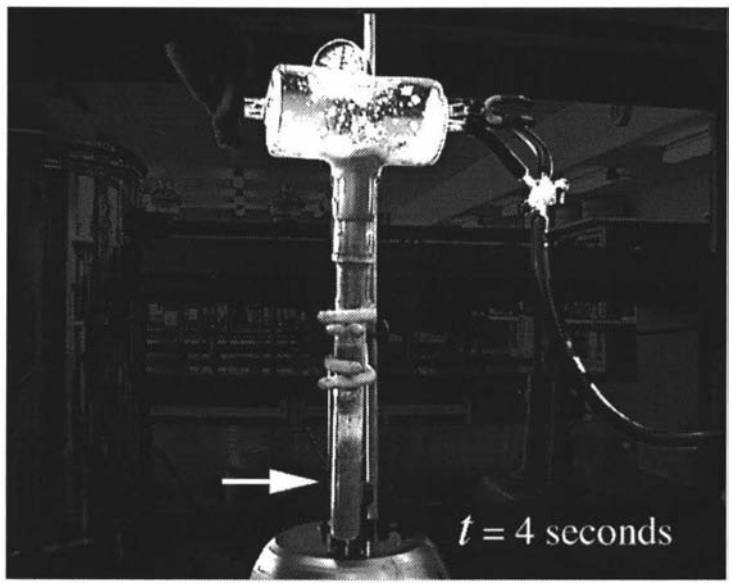

(d) 4 seconds

Figure 2.3: Laboratory hydrothermal eruption in progress.

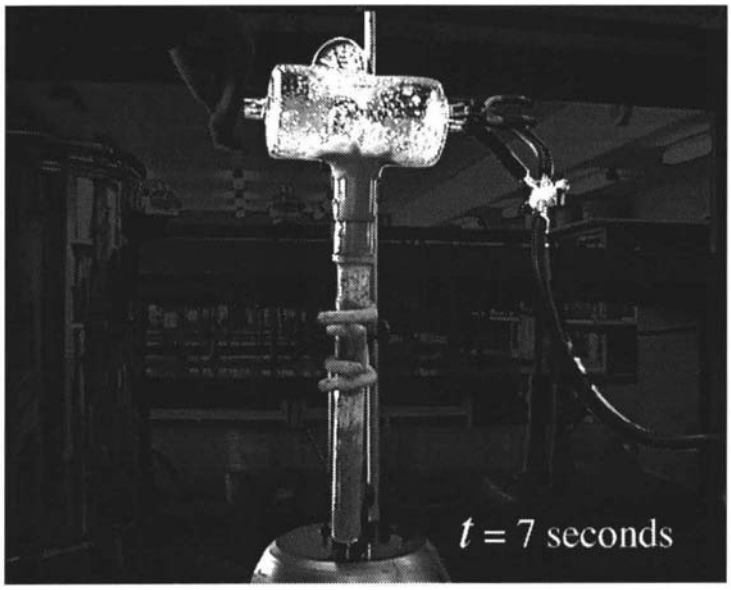

(e) 7 seconds

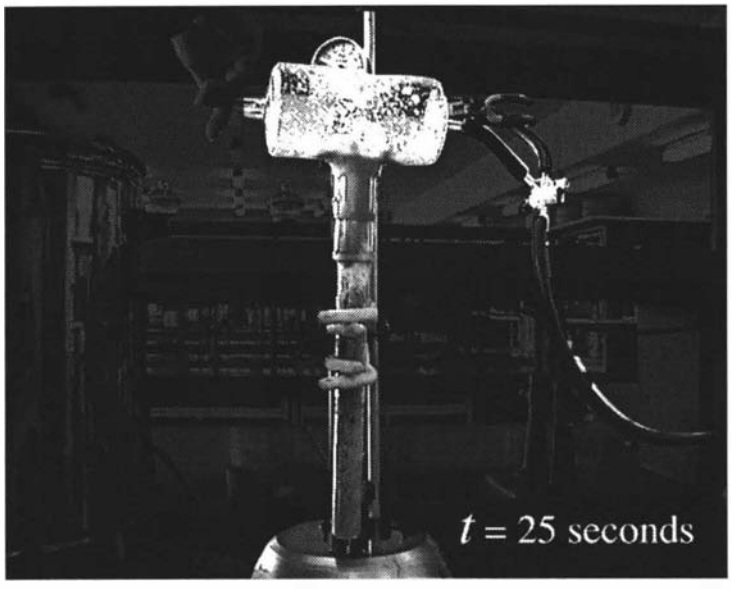

(f) 25 seconds

Figure 2.3: Laboratory hydrothermal eruption in progress.

CHAPTER 3

Mathematical Formulation

Now that a conceptual model has been formed from the information collected by efforts of those such as Browne (1986), Collar (1985), Scott and Cody (1982), Allis (1983) and Lloyd and Keam (1974) and qualitative support for the model has been obtained through experiment, the laws of physics and thermodynamics may be employed to form a mathematical model to determine how an eruption might proceed. The remainder of this thesis will focus on the underground fluid flow and boiling processes that take place and in this chapter a mathematical model for this flow is presented. The principles of conservation of mass, momentum and energy are used to formulate the mathematical problem. A set of non-linear partial differential equations governing transient mass and energy transport is obtained. The remainder of this work will be concerned with the solution to those equations under various simplifying assumptions.

3.1 The Equations of Motion

The geothermal field in which the hydrothermal eruption occurs is considered to be a permeable fluid-saturated porous medium. That is, it is made up of a solid rock matrix (the ground) and interconnected void space (spaces and fractures in the rock through which fluid flows). The rock matrix together with the void space will be referred to as "the formation". The rock matrix is assumed to be rigid (non-deformable) and its matrix properties are assumed to be uniformly constant. The ground fluid that saturates the void space is assumed to be a two-phase mixture of liquid water and water vapour. The effects of non-condensable gases on the system are not considered here.

The usual course of deriving the equations of motion that govern fluid flow in a porous medium is to obtain macroscopically-averaged forms of the standard microscopic

fluid dynamical equations. While in theory the standard microscopic equations can be solved for quantities of interest, such as pressure, in practice this is not possible. The complex geometry of the boundaries that exist between phases at this level cannot be seen or accurately described. Furthermore, any results obtained from the solution of such equations would be impractical as quantities solved for at a point will vary irregularly with respect to space and time and cannot be validated by experimental measurement. Experimentally, flow quantities are measured at the macroscopic level. Space-averaged quantities at this level vary regularly and macroscopic boundary value problems can be solved. A rigorous description of the derived macroscopic equations for this general fluid flow can be found in, for example, Bear and Bachmat (1991). Details of the equations, as they are needed in the mathematical model presented here, follow.

In forming the mathematical model a small universal averaging volume or representative elementary volume (REV), taken from the ground region is considered. Macroscopic variables are then defined as appropriate averages over the REV and the value of the variable is assigned to its centroid. The obtained value of this variable must be independent of the choice of REV. The size of the REV is chosen such that if l is a characteristic length of the REV, d a characteristic length of the microscopic structure of the void space and L a characteristic length of the porous medium domain then $d \ll l \ll L$. That is, the REV is chosen to be large enough to contain both some rock and some fluid, but small enough so that any property of the rock matrix or water mixture is nearly uniform throughout. Figure 3.1 illustrates an REV containing both rock and pore space through which a water mixture flows.

Two models for the underground boiling process which occurs in hydrothermal eruptions are presented based on differing assumptions about the fluid which is flowing through the void (or pore) space. The first model assumes that because of the rapidity of motion, a separable two-phase flow does not have time to develop. In this case the liquid and vapour phases are modelled as if they are flowing together through the void space in a single flow while boiling occurs. The fluid is a homogeneous mixture of liquid water and water vapour and the model is called the homogeneous mixture (HM) flow model. In the second model, the water mixture is modelled as two phases flowing separately. The liquid and vapour each develop their own separate flows through the pore space and the model is called the separable phase (SP) flow model. Under one of these two fluid flow assumptions, conservation of mass, momentum and energy equations are set up on the universal averaging volume (REV) within the formation.

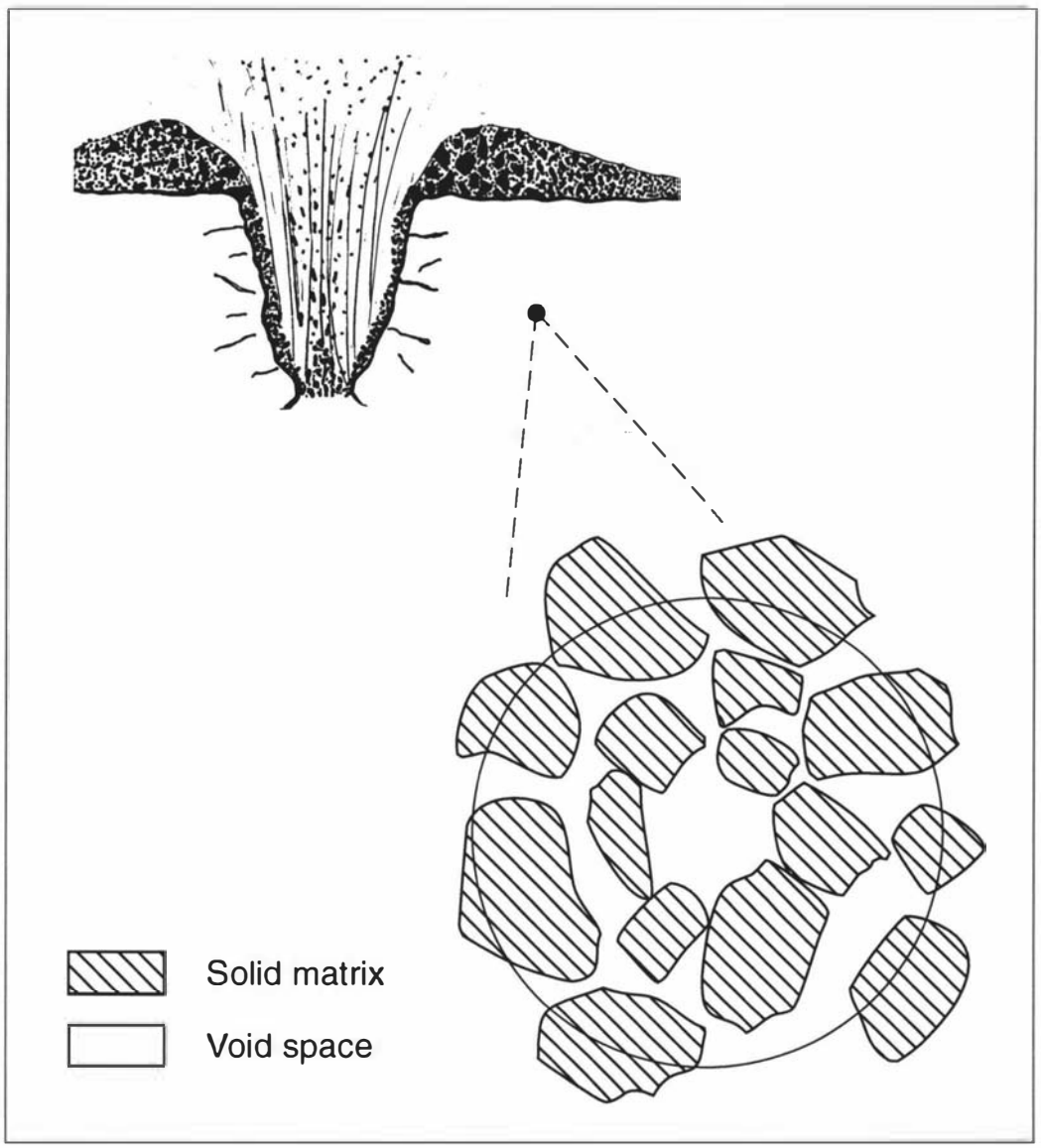

Figure 3.1: Representative Elementary Volume within the formation.

3.1.1 General Conservation of Fluid Mass and Energy Equations

In both models, the general conservation of fluid mass and energy equations for transient flow without sources can be written respectively as follows

$$\frac{\partial A_m}{\partial t} = -\nabla \cdot \mathbf{Q}_m \tag{3.1}$$

$$\frac{\partial A_e}{\partial t} = -\nabla \cdot \mathbf{Q}_e \tag{3.2}$$

where A_m and A_e are the fluid mass and energy per unit volume of formation and $\mathbf{Q}_m$ and $\mathbf{Q}_e$ are the mass and energy fluxes per unit area of the formation.

Expressions for A_m, A_e, $\mathbf{Q}_m$, and $\mathbf{Q}_e$ in terms of matrix and fluid parameters are given in Section 3.1.2 for the homogeneous mixture flow case and in Section 3.1.3 for the separable phase flow case. In both cases Equation 3.1 states that the time rate of increase of mass inside a representative elementary volume equals the net mass flow rate across the surface of the volume, while Equation 3.2 states that the change in energy inside the volume is equal to the net advected energy flow rate across the surface plus the net energy gained or lost by conduction. Derivations of these equations can be found in, for example, O'Sullivan and McKibbin (1989).

3.1.2 Homogeneous mixture (HM) flow model

In the case of the homogeneous mixture model, single-phase equations with parameters that depend on the two-phase fluid mixture are used to describe the flow. The parameters of the fluid mixture that are needed for this description are:

$$\rho_f = S\rho_l + (1-S)\rho_v \tag{3.3}$$

$$h_f = \frac{S\rho_l h_l + (1-S)\rho_v h_v}{S\rho_l + (1-S)\rho_v} \tag{3.4}$$

$$u_f = \frac{S\rho_l u_l + (1-S)\rho_v u_v}{S\rho_l + (1-S)\rho_v} \tag{3.5}$$

$$\mu_f = S\mu_l + (1-S)\mu_v \tag{3.6}$$

Here the subscript f is used to represent the fluid mixture and the subscripts l and v refer to the liquid and vapour phases. The properties of the fluid mixture ($i = f$), liquid phase

($i = l$) and vapour phase ($i = v$) are: ρ_i is the density, h_i is the specific enthalpy, u_i is the specific internal energy and μ_i is the dynamic viscosity. The density, specific enthalpy and specific internal energy of the fluid mixture are found by mass fraction considerations (or volume balances). The liquid saturation S of the fluid mixture is the volume fraction of the two-phase fluid mixture that is occupied by liquid water. The volume fraction that is occupied by water vapour is therefore $1 - S$. The dynamic viscosity of the fluid mixture may not be found from conservation laws and is assumed to have the form given in Equation 3.6.

The volume available for the flow of fluid within an REV is given by the porosity ϕ. It is the fraction of the total volume of the REV (or in general, the porous medium) that is void space. It is a property of the rock matrix and is assumed to be uniformly constant. The mass density, or mass of water per unit volume of the formation, referred to in Equation 3.1 is then given by

$$A_m = \phi \rho_f \tag{3.7}$$

The energy density referred to in Equation 3.2 includes two terms: one for the energy content of the rock matrix and another for the energy of the two-phase water mixture. The volume within the REV occupied by the rock matrix is $1 - \phi$. The energy content of the rock matrix is then given by $(1 - \phi)\rho_r u_r$ where the subscript r is used to represent the rock matrix. The specific internal energy of the rock is very closely proportional to the temperature and can be written in the form $u_r = c_r T$ where c_r is the specific heat (heat capacity) of the rock and T is the temperature. As stated earlier, the properties of the rock matrix, and therefore ρ_r and c_r, are assumed to be constant. The energy of the water mixture is given by $\phi \rho_f u_f$. Therefore, the energy density referred to in the conservation of energy equation can be written in the form

$$A_e = (1 - \phi)\rho_r c_r T + \phi \rho_f u_f \tag{3.8}$$

The mass flux term found in the conservation of mass equation (3.1) is given by

$$\mathbf{Q}_m = \rho_f \mathbf{v}_f \tag{3.9}$$

where $\mathbf{v}_f$ is the specific volume flux (fluid volume flux per unit cross-sectional area of formation), also called the Darcy velocity or specific discharge.

For sufficiently small fluid velocities ($Re < 1$), $\mathbf{v}_f$ is given by Darcy's law. In this HM flow model, a single-phase Darcy law with parameters depending on the two-phase fluid mixture is used.

$$\mathbf{v}_f = \frac{k}{\mu_f}(-\nabla p + \rho_f \mathbf{g}) \tag{3.10}$$

Here k is the permeability of the rock matrix and is assumed to be constant. It is a measure of the ease with which fluid may flow through the porous medium. The constant vector $\mathbf{g}$ is the acceleration due to gravity. Note that by Darcy's Law, the mass flow rate $\mathbf{Q}_m$ is proportional to the dynamic pressure gradient, that is, fluid flows towards regions of lower dynamic pressure (pressure corrected for fluid weight).

For higher velocities, such as those occurring near the surface in hydrothermal eruptions, non-linear drag effects must be taken into account. In this case, Darcy's Law can be modified and the following Forchheimer's Equation used (see Nield and Bejan 1992 for details).

$$\mathbf{v}_f = \frac{k}{\mu_f}(-\nabla p + \rho_f \mathbf{g}) - \frac{c_F}{\nu_f k^{1/2}} \mid \mathbf{v}_f \mid \mathbf{v}_f \tag{3.11}$$

Here c_F is a dimensionless form-drag constant which depends on the geometrical properties of the fluid particles and the porous medium, and ν_f is the fluid kinematic viscosity which is given by ρ_f/μ_f.

When modelling the one-dimensional case of vertical flow in hydrothermal eruptions Bercich and McKibbin (1992) found that for permeabilities of $1 \times 10^{-12}\ m^2$ (≈ 1 Darcy) or less, the effects of the non-linear Forchheimer term were negligible and the simple Darcy's Law provided good approximations. Note that the use of the Forchheimer term alters the pressure gradient calculations (slightly), but the fluid still flows in the same direction. For the work in this thesis, the simple Darcy's Law will be used.

The energy flux term found in Equation 3.2 includes two terms: the first represents the advected energy flow rate across the surface of the REV while the second accounts for the energy gained or lost by conduction.

$$\mathbf{Q}_e = h_f \mathbf{Q}_m - K\nabla T \tag{3.12}$$

K is the thermal conductivity of the formation and is given by $K = K_r(1-\phi) + K_f\phi$, where K_r is the thermal conductivity of the rock matrix and K_f is the thermal conductivity of the fluid mixture. For small porosities, $K \approx K_r$. In this work, it is assumed $K = K_r$ is uniformly constant.

3.1.3 Separable phase (SP) flow model

In the case of separable phase flow, a two-phase Darcy Law is used to determine the mass flow rate per unit area. The fluid mass and energy per unit volume of formation and mass and energy fluxes per unit area in this case are given by

$$A_m = \phi[S\rho_l + (1-S)\rho_v] \tag{3.13}$$

$$A_e = (1-\phi)\rho_r c_r T_{sat} + \phi[S\rho_l u_l + (1-S)\rho_v u_v] \tag{3.14}$$

$$\mathbf{Q}_m = \mathbf{Q}_{ml} + \mathbf{Q}_{mv} \tag{3.15}$$

$$\mathbf{Q}_e = h_l\mathbf{Q_{ml}} + h_v\mathbf{Q_{mv}} - K\nabla T \tag{3.16}$$

where

$$\mathbf{Q_{ml}} = \rho_l\mathbf{v_l} = -\rho_l\frac{kk_{rl}}{\mu_l}(-\nabla p + \rho_l\mathbf{g}) \tag{3.17}$$

$$\mathbf{Q_{mv}} = \rho_v\mathbf{v_v} = -\rho_v\frac{kk_{rv}}{\mu_v}(-\nabla p + \rho_v\mathbf{g}) \tag{3.18}$$

Here k_{rl} and k_{rv} are the relative permeabilities (or permeability reduction factors) with respect to the liquid and vapour phases respectively. As the liquid and vapour phases flow together through the porous medium, they interfere with each other. The relative permeabilities are permeability reduction factors used to account for this interference. At any point in the liquid phase, the flow of the liquid is affected not only by the presence of (and its interaction with) the rock matrix, but by the vapour phase which shares the pore space. The effective permeability of the medium to the liquid phase is given by kk_{rl} and the effective permeability of the vapour phase is given by kk_{rv}. The relative permeabilities are functions of liquid saturation and may be determined experimentally for homogeneous porous media. In geothermal reservoir engineering a variety of relative

permeability functions have been used, including linear curves, (most frequently) Corey curves, Brooks-Corey curves, and van Genuchten curves. Descriptions of these functions can be found in, for example, Guerrero (1998). Relative permeability curves used in this work are linear and are described in Appendix B.

3.2 Equation of State

The fluid is assumed to be at saturated (boiling) conditions; the equation of state is given by

$$p = p_{sat}(T) \tag{3.19}$$

where $p_{sat}(T)$ is the saturation pressure, the pressure at which water boils for a given temperature T. Alternatively, for a given pressure p, $T_{sat}(p)$ is the saturation temperature. At such so-called saturated conditions, both liquid water and water vapour may be present in the system. Saturation temperature increases with increasing pressure [see any standard set of steam tables, for example, Rogers and Mayhew (1980)].

Standard correlations for the thermodynamic properties of water may be used. In Chapter 5, solutions to the models presented are found over small temperature and pressure ranges. In an effort to speed up calculations, the "full" correlations [as used in the commercially available groundwater flow and heat transport simulators TOUGH2 (Pruess 1991) and HYDROTHERM (Hayba and Ingebritsen 1994), for example] were not used. Instead, a set of formulas were developed for the thermodynamic properties over suitable temperature and pressure ranges. These formulas are described in Appendix B.

3.3 Boundary Conditions

The pressure and temperature conditions at the ground surface and at large distances in the ground are assumed to be ambient (defined here to mean: motionless, with hydrostatic pressure distribution, and temperature increasing with the so called "boiling point with depth" relation).

3.4 Steady Flow

In earlier investigations (Bercich and McKibbin 1992; McKibbin 1990, 1996), the following additional assumptions were made: the eruption was assumed to already be in

progress and was modelled as steady over short periods of time; the fluid was assumed to be moving so rapidly that the heat transfer between the rock and fluid was ignored, that is, conductive energy was assumed to be negligible, and the process was modelled as adiabatic.

Under these assumptions, the equations for conservation of mass and energy given in Equations 3.1 and 3.2 become, respectively,

$$\nabla \cdot \mathbf{Q}_m = 0 \tag{3.20}$$

$$\nabla \cdot (h_f \mathbf{Q}_m) = 0 \tag{3.21}$$

By combining Equations 3.20 and 3.21 we find

$$\mathbf{Q}_m \cdot \nabla h_f = 0 \tag{3.22}$$

which implies that the specific enthalpy is constant along the streamlines.

In this chapter, the equations of motion describing the underground flow in hydrothermal eruptions have been laid out. The remainder of this thesis is concerned with the solutions to these equations under the simplified situations of steady isothermal flow and flow in one horizontal dimension.

CHAPTER 4

Steady State Isothermal Flows

4.1 Introduction

The problem of solving the set of non-linear partial differential equations governing the transient non-isothermal underground flow during hydrothermal eruptions is a complicated one. Analytic techniques for solving these equations (see Chapter 3) are not available, and numerical methods are, in practice, employed. However, solutions of the (suitably simplified) equations of motion for steady isothermal single-phase flow may be obtained analytically and numerical solutions verified against analytical results. Such verification allows testing of mathematical procedures, which may then be used in solving the non-isothermal case. Solutions obtained from this isothermal case also provide insights into the recharge of the system following an eruption.

The procedure of solving the equations of motion in the steady isothermal case under boundary conditions as given in Section 3.3 relates to the following: consider the problem of digging a hole for the purposes of extracting water. If water is continually pumped out of the hole, where does the water come from? As with the non-isothermal case, a pressure reduction will cause the flow to commence. In this chapter we investigate how to quantify the flow around and into the hole in the isothermal case, and determine where the flowing water originates.

Assumptions for this steady isothermal single-phase case are as follows. Conductive and advective heat flow can be neglected, as the process is isothermal. Treating the problem as seepage flow, the non-linear term in the specific volume flux, Equation 3.11, may also be neglected and Darcy's Law, Equation 3.10, may be used. The fluid is liquid water and, as the process is isothermal, $\rho = \rho_f$ and $\mu = \mu_f$ are both constant.

Then from Equations 3.9 and 3.10, the specific mass flux vector is given by

$$\mathbf{Q}_m = \frac{k}{\nu}(-\nabla p + \rho \mathbf{g}) \tag{4.1}$$

where $\nu = \mu/\rho$ is the kinematic viscosity of the fluid. The mass flux vector may then be written in the form:

$$\mathbf{Q}_m = \nabla \Phi_m \tag{4.2}$$

where the potential Φ_m for the specific mass flux $\mathbf{Q}_m$ may be written

$$\Phi_m = -\frac{k}{\nu}(p - p_{atm} + \rho g z) \tag{4.3}$$

where z is the vertical co-ordinate, with $z = 0$ at the surface (where $p = p_{atm}$). Substitution into the conservation of mass equation 3.20 gives

$$\nabla^2 \Phi_m = 0 \tag{4.4}$$

which is Laplace's equation for Φ_m, and so Φ_m is a harmonic function.

The solution to the axially-symmetric isothermal problem is found below in three different two-dimensional geometrical configurations.

4.2 Semi-circular horizontal trench

First, consider the case of digging a semi-circular horizontal trench in level ground for the extraction of water. The axis of the trench lies along the surface and its origin is located at the centre of the trench. The radius of the trench is a and it is assumed that conditions are ambient at a distance b from the origin. The solution to the flow in this problem can be found by solving Laplace's equation, Equation 4.4, in polar co-ordinates perpendicular to the trench. See Figure 4.1.

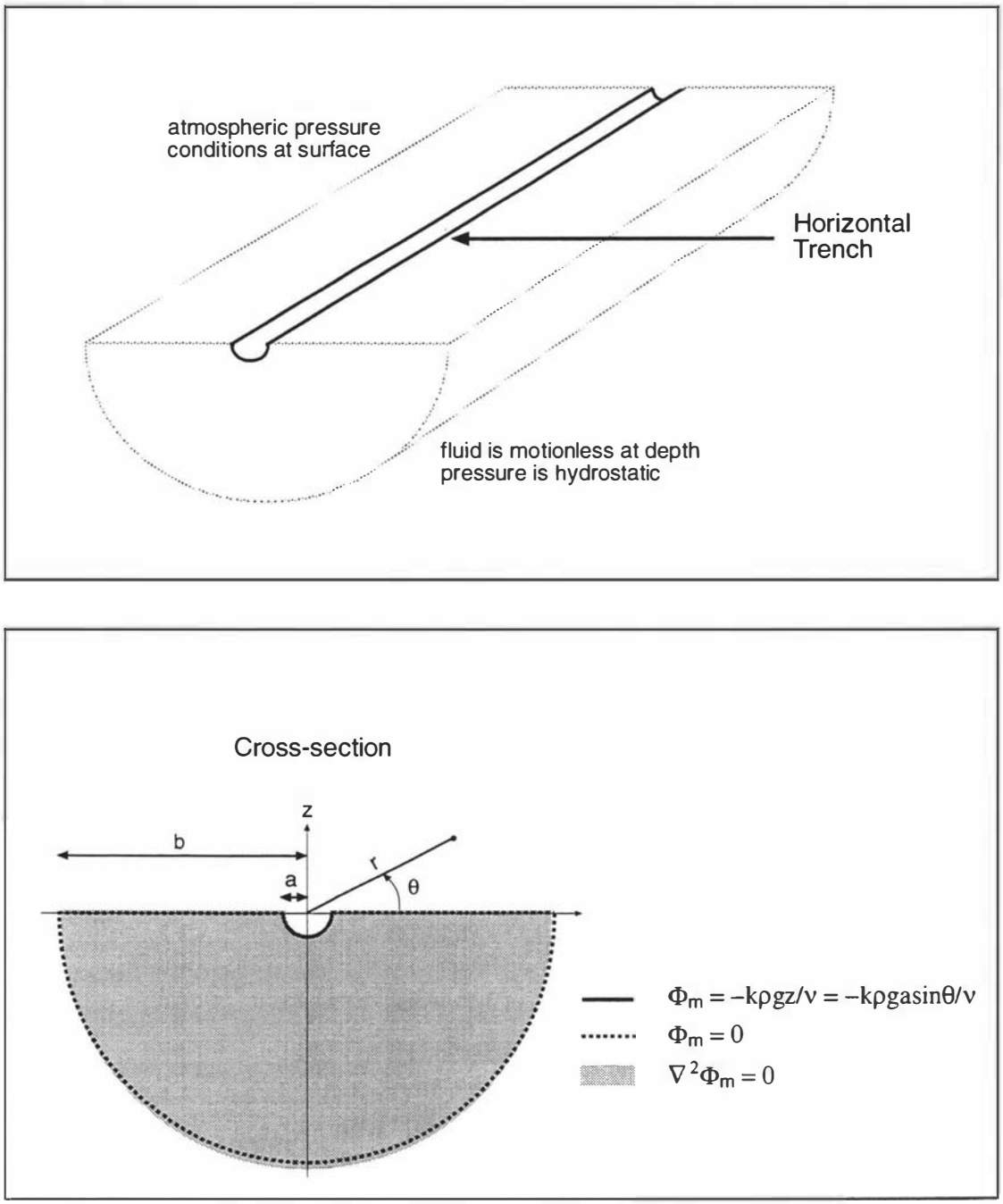

Figure 4.1: Semi-circular horizontal trench dug for extracting water. A cross-section of the ground region, illustrating boundary conditions for the flow problem, is shown. (See text in Section 4.2 for details.)

In polar co-ordinates, with the usual notation, Laplace's equation for $\Phi_m(r,\theta)$ is given by

$$\frac{\partial^2\Phi_m}{\partial r^2}+\frac{1}{r}\frac{\partial\Phi_m}{\partial r}+\frac{1}{r^2}\frac{\partial^2\Phi_m}{\partial\theta^2}=0 \tag{4.5}$$

where $a \leq r \leq b$, $\pi \leq \theta \leq 2\pi$. (See Figure 4.1.) The boundary conditions at the surface are taken to be very idealized. The pressure is atmospheric and remains so. At large r, the pressure is hydrostatic. In this case the boundary conditions are

$$\begin{aligned} &\Phi_m(r,\pi)=\Phi_m(r,2\pi)=0 && \text{for} \quad a\leq r\leq b \\ &\Phi_m(a,\theta)=\tfrac{-k\rho gz}{\nu}=\tfrac{-k\rho ga\sin\theta}{\nu},\ \Phi_m(b,\theta)=0 && \text{for} \quad \pi\leq\theta\leq 2\pi \end{aligned} \tag{4.6}$$

The analytic solution for Equation 4.5 with boundary conditions 4.6 is found using separation of variables. The mass flux potential is

$$\Phi_m=\frac{k\rho ga^2b}{\nu(b^2-a^2)}\left(\frac{r}{b}-\frac{b}{r}\right)\sin\theta \tag{4.7}$$

From Equation 4.2 the specific mass flux vector is then

$$\mathbf{Q}_m=\frac{k\rho ga^2b}{\nu(b^2-a^2)}\left[\left(\frac{r^2+b^2}{br^2}\right)\sin\theta\mathbf{e_r}+\left(\frac{r^2-b^2}{br^2}\right)\cos\theta\mathbf{e}_\theta\right] \tag{4.8}$$

where $\mathbf{e_r}$, $\mathbf{e}_\theta$ are unit vectors in the r, θ directions respectively. If the total mass flux into the trench per unit length of the cavity is denoted by Q, then by integrating the radial component of the mass flux vector (flux normal to the trench surface) the following expression for Q is obtained:

$$Q=\frac{2k\rho ga}{\nu}\frac{a^2+b^2}{b^2-a^2} \tag{4.9}$$

A mass stream-function, Ψ_m, which is related to the mass flux by

$$\mathbf{Q}_m = \frac{1}{r}\frac{\partial \Psi_m}{\partial \theta}\mathbf{e_r} - \frac{\partial \Psi_m}{\partial r}\mathbf{e}_\theta \tag{4.10}$$

and which thereby enables Equation 3.20 to be satisfied exactly, may be found for this problem in the form

$$\Psi_m = -\frac{k\rho g a^2 b}{\nu(b^2 - a^2)}\left(\frac{r}{b} + \frac{b}{r}\right)\cos\theta \tag{4.11}$$

A velocity potential, Φ, and stream-function, Ψ, may then be found for the flow in the form

$$\Phi = \frac{\Phi_m}{\rho} = \frac{k\rho g a^2 b}{\mu(b^2 - a^2)}\left(\frac{r}{b} - \frac{b}{r}\right)\sin\theta \tag{4.12}$$

$$\Psi = \frac{\Psi_m}{\rho} = -\frac{k\rho g a^2 b}{\mu(b^2 - a^2)}\left(\frac{r}{b} + \frac{b}{r}\right)\cos\theta \tag{4.13}$$

The stream surfaces (surfaces whose tangents are everywhere parallel to the velocity vector) are given by Ψ equal to a constant. The streamlines (cross-section of the stream surfaces) are everywhere perpendicular to the equipotential lines (isolines for the velocity potential function).

As the outer radius b of the solution region becomes large, for finite r

$$\Phi \rightarrow -\frac{k\rho g a^2}{\mu}\frac{1}{r}\sin\theta \tag{4.14}$$

$$\mathbf{Q}_m \rightarrow \frac{k\rho g a^2}{\nu}\left(\frac{1}{r^2}\sin\theta\mathbf{e_r} - \frac{1}{r^2}\cos\theta\mathbf{e}_\theta\right) \tag{4.15}$$

$$Q \rightarrow \frac{2k\rho g a}{\nu} \tag{4.16}$$

$$\Psi \rightarrow -\frac{k\rho g a^2}{\mu}\frac{1}{r}\cos\theta \tag{4.17}$$

$$p \quad \rightarrow \quad p_{atm} + \rho g \left(\frac{a^2}{r} - r \right) \sin\theta \tag{4.18}$$

Note that the total mass flux per unit length, Q, is proportional to the depth, a, of the trench.

The value of b for which the equations describing the flow near the trench converge to those found in Equations 4.14 - 4.18 is of interest. While in this case an analytic solution can be found, such a value for b may provide a guide to domain size where only a numerical solution is able to be found. From Equations 4.9, 4.16, 4.13 and 4.17,

$$\begin{aligned} \frac{Q}{Q \text{ as } b \rightarrow \infty} = \frac{\Psi(a,\theta)}{\Psi(a,\theta) \text{ as } b \rightarrow \infty} &= \frac{a^2 + b^2}{b^2 - a^2} = \frac{1 + \frac{a^2}{b^2}}{1 - \frac{a^2}{b^2}} \\ &\approx \left[1 + \left(\frac{a}{b} \right)^2 \right] \left[1 + \left(\frac{a}{b} \right)^2 \right] \\ &\approx 1 + 2 \left(\frac{a}{b} \right)^2 \end{aligned} \tag{4.19}$$

Hence analytic solutions for large b and for $b = 10a$ agree to within about 2%.

The isobars (cross-section of isobaric surfaces) and streamlines (cross-section of the stream surfaces) are shown in Figures 4.2 and 4.3 respectively. These were calculated on the simulation field $a \leq r \leq b = 10a$, and an enlargement of the region out to $r = 2.5a$ is also depicted. Equipotential lines have also been calculated in this case and can be shown, as expected, to be everywhere perpendicular to the streamlines. (See Figure 4.4.)

The results show the main pressure reduction to be local. (See Figure 4.2.) It is this pressure lowering which will have a significant effect on flashing in a hydrothermal eruption. We might therefore expect hydrothermal eruption fluid to originate locally.

From Equation 4.13, the ratios of the flow originating from the surface to the total flow, and that from the subsurface to the total, are given by

$$\frac{\Psi(a,\pi) - \Psi(b,\pi)}{\Psi(a,\pi) - \Psi\left(a, \frac{3\pi}{2}\right)} = 1 - \frac{2ab}{a^2 + b^2} \tag{4.20}$$

$$\frac{\Psi\left(b, \frac{3\pi}{2}\right) - \Psi(b,\pi)}{\Psi(a,\pi) - \Psi\left(a, \frac{3\pi}{2}\right)} = \frac{2ab}{a^2 + b^2} \tag{4.21}$$

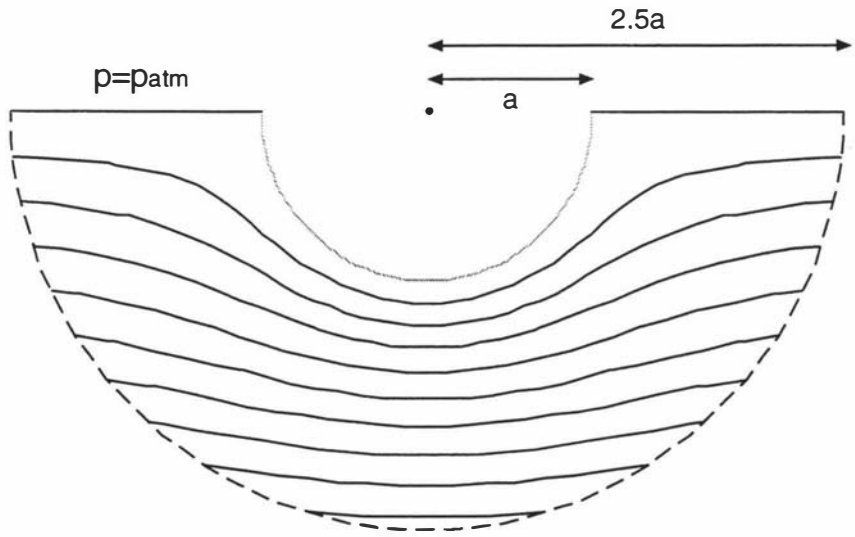

(a) Cross-section of isobaric surfaces, region out to $r = 2.5a$ depicted.

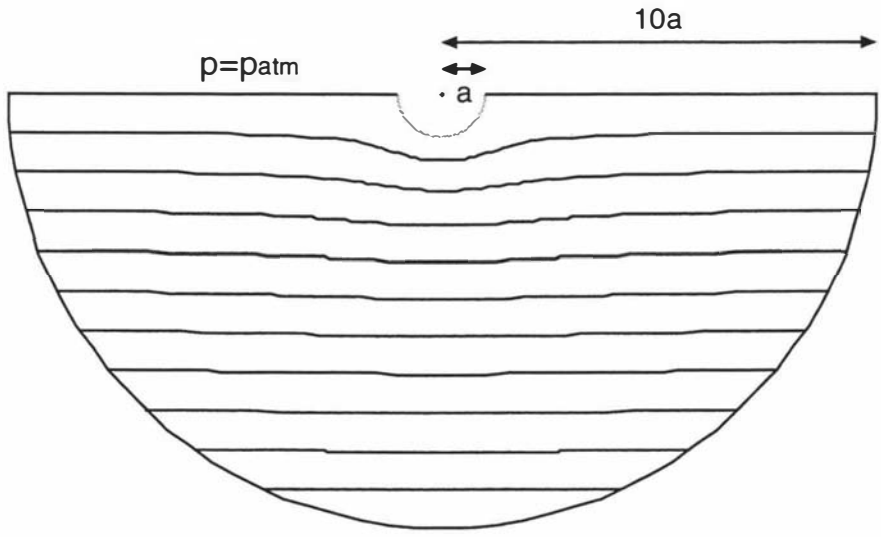

(b) Cross-section of isobaric surfaces shown over simulation field $a \leq r \leq 10a$.

Figure 4.2: Isolines for pressure for semi-circular horizontal trench. (See text for details.)

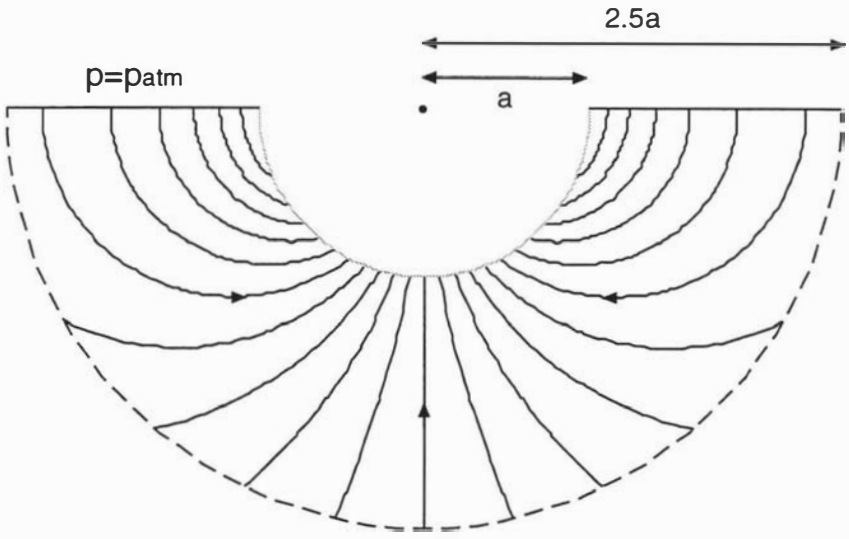

(a) Cross-section of stream surfaces, region out to $r = 2.5a$ depicted.

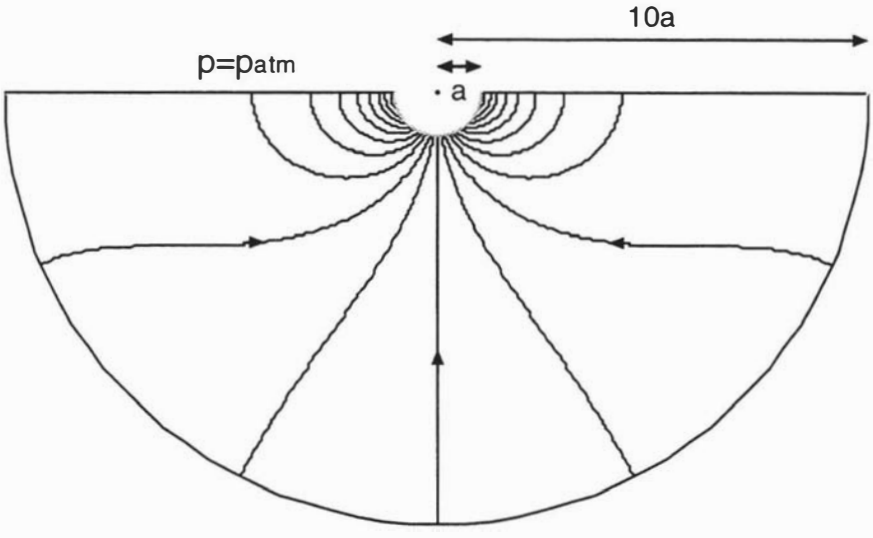

(b) Cross-section of stream surfaces shown over simulation field $a \leq r \leq 10a$.

Figure 4.3: Isolines for stream-function for semi-circular horizontal trench. (See text for details.)

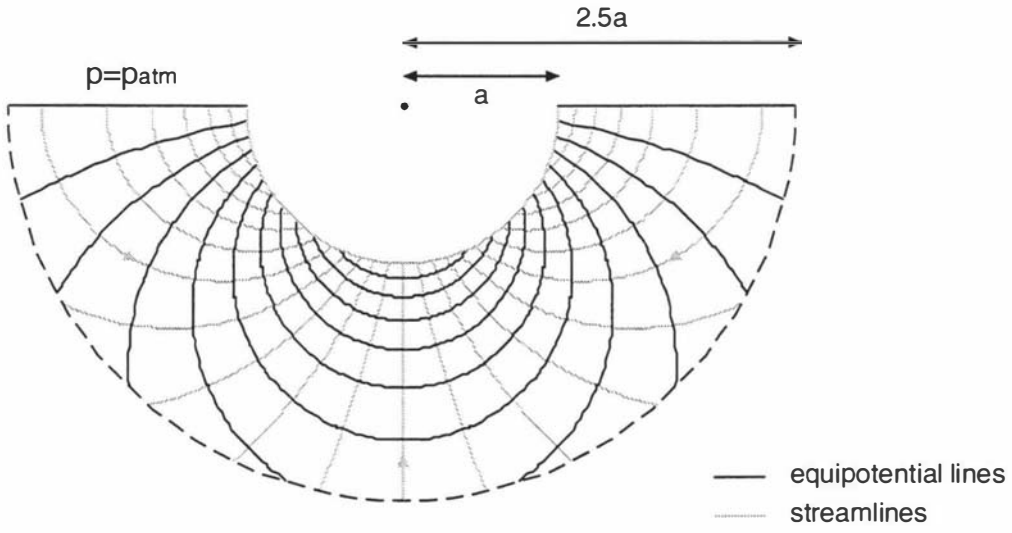

Figure 4.4: Equipotential and streamlines for semi-circular horizontal trench. Region out to $r = 2.5a$ depicted. (See text for details.)

For the case $b = 10a$ illustrated in Figure 4.3, approximately 80% of the flow originates from the surface while 20% is derived from groundwater. However, as the outer radius b for the solution region becomes large, Equations 4.20 and 4.21 show that, in the long term, all of the water arriving at the trench originally came from the surface.

It is also possible to determine where most of the recharge of water is coming from in the relatively short term. As the outer radius b of the solution region becomes large, the travel time from a point, (r_0, θ_0), to the trench may be calculated as follows: Equation 4.17 may be written in the form

$$\Psi = -A\frac{1}{r}\cos\theta \tag{4.22}$$

where

$$A = \frac{k\rho g a^2}{\mu} \tag{4.23}$$

The component of the Darcy velocity of the flow in the radial direction is given by

$$v_r = \frac{1}{r}\frac{\partial \Psi}{\partial \theta} = A\frac{1}{r^2}\sin\theta \tag{4.24}$$

The radial component, u_r, of the pore-averaged velocity (fluid particle velocity) of the flow is given in terms of the radial component of the Darcy velocity by

$$u_r = \frac{1}{\phi}v_r \tag{4.25}$$

where ϕ is the porosity.

Consider the solution region $3\pi/2 \leq \theta \leq 2\pi$, $r \geq a$. (The solution in the region $\pi \leq \theta < 3\pi/2$, $r \geq a$ may be found by symmetry.) For $\theta_0 \neq 3\pi/2$, combining and rearranging Equations 4.22 and 4.24 gives

$$\begin{aligned} {v_r}^2 + \left(\frac{\Psi}{r}\right)^2 &= \frac{A^2}{r^4} \\ {v_r}^2 &= \frac{A^2}{r^4} - \frac{\Psi^2}{r^2} \end{aligned} \tag{4.26}$$

The value of the stream-function Ψ is constant along a given streamline (line whose tangent is everywhere parallel to the velocity vector). Therefore, along the streamline which passes through the point (r_0, θ_0) the value of the stream-function is $\Psi(r_0, \theta_0)$. Equation 4.26 may then be written in the form

$${v_r}^2 = \frac{A^2}{r^4} - \frac{\Psi\,(r_0,\theta_0)^2}{r^2} = \frac{A^2\cos^2\theta_0}{{r_0}^2}\frac{1}{r^4}\left(\frac{{r_0}^2}{\cos^2\theta_0} - r^2\right) \tag{4.27}$$

Using Equations 4.25 and 4.27 for $3\pi/2 < \theta_0 \leq 2\pi$ and Equations 4.24 and 4.25 for $\theta_0 = 3\pi/2$, u_r may be written in the form

$$u_r = \frac{dr}{dt} = \begin{cases} -\frac{A\cos\theta_0}{\phi {r_0}}\frac{1}{r}\left(\frac{{r_0}^2}{\cos^2\theta_0} - r^2\right)^{1/2} & 3\pi/2 < \theta_0 \leq 2\pi \\ -\frac{A}{\phi r^2} & \theta_0 = 3\pi/2 \end{cases} \tag{4.28}$$

Integration of Equation 4.28 on the interval $a \leq r \leq r_0$ gives

$$\frac{2A}{\phi}t = \begin{cases} \frac{{r_0}^3}{\cos^3\theta_0}\left[\theta_0 + \sin\theta_0\cos\theta_0 - \arccos\left(\frac{a\cos\theta_0}{r_0}\right)\right. & \\ \qquad \left. + \frac{a}{r_0}\cos\theta_0\sqrt{1-\frac{a^2}{r_0^2}\cos^2\theta_0}\right] & 3\pi/2 < \theta_0 \leq 2\pi \\ \frac{2}{3}\left({r_0}^3 - a^3\right) & \theta_0 = 3\pi/2 \end{cases} \tag{4.29}$$

Equation 4.29 can then be used to plot isolines for the "time to trench". All fluid along a particular isoline will arrive at the trench at the same time. (See Figure 4.5.)

For a given "time to trench" isoline (see Figure 4.5), let r_x be the radius at which the isoline intersects the x-axis and r_y the radius at which the isoline intersects the y-axis. Using Equation 4.29, it can be shown that the ratio r_x/r_y is always less than or equal to one, decreases with time t and tends to the value $\sqrt[3]{4/3\pi} \approx 0.7515$ for large times t. The ratio $(r_x - a)/(r_y - a)$ increases with time t and also tends to the value $\sqrt[3]{4/3\pi}$ for large times t. Hence the flow is always "digging deeper" from beneath the bottom of the trench (a distance of $r_y - a$) than it is "reaching out" from the sides of the trench (a distance of $r_x - a$). While the difference between these two distances increases in length with time, the difference between the two decreases with time relative to the length scale of $r_x - a$ (or $r_y - a$).

The ratio of the flow originating from the surface to the total flow may be plotted against time in the following way. Let $t(r_0, 2\pi)$ be the time it takes for the fluid originating at the point $(r_0, 2\pi)$ to reach the trench, and let $F(r_0)$ be the ratio of the flow originating from the surface to the total flow during this time. Using Equation 4.17, $F = F(r_0)$ is then given by

$$F = \frac{\Psi(r_0, 2\pi) - \Psi(a, 2\pi)}{\Psi(a, 3\pi/2) - \Psi(a, 2\pi)} = 1 - \frac{a}{r_0} \tag{4.30}$$

Equations 4.29 and 4.30 may be used to find the following equation for time as a function of F (the ratio of the flow originating from the surface to the total flow).

$$\frac{2A}{\phi a^3}t = \frac{2\pi - \arccos(1-F) + (1-F)\sqrt{1-(1-F)^2}}{(1-F)^3} \tag{4.31}$$

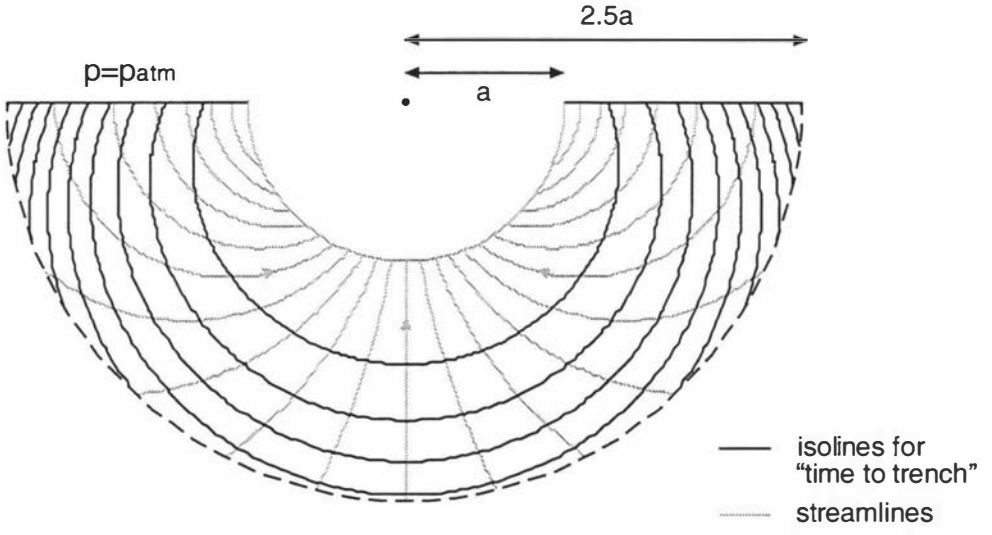

(a) Cross-section of "time to trench" surfaces, region out to $r = 2.5a$ depicted.

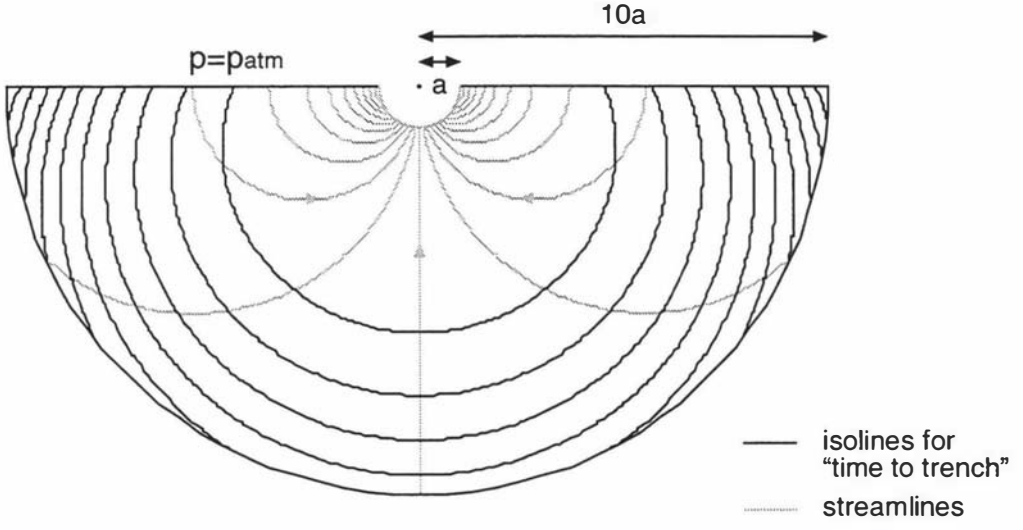

(b) Cross-section of "time to trench" surfaces shown over simulation field $a \leq r \leq 10a$.

Figure 4.5: Isolines for "time to trench" and streamlines for semi-circular horizontal trench. All fluid on a given "time to trench" isoline will reach the trench surface at the same time. (See text for further details.)

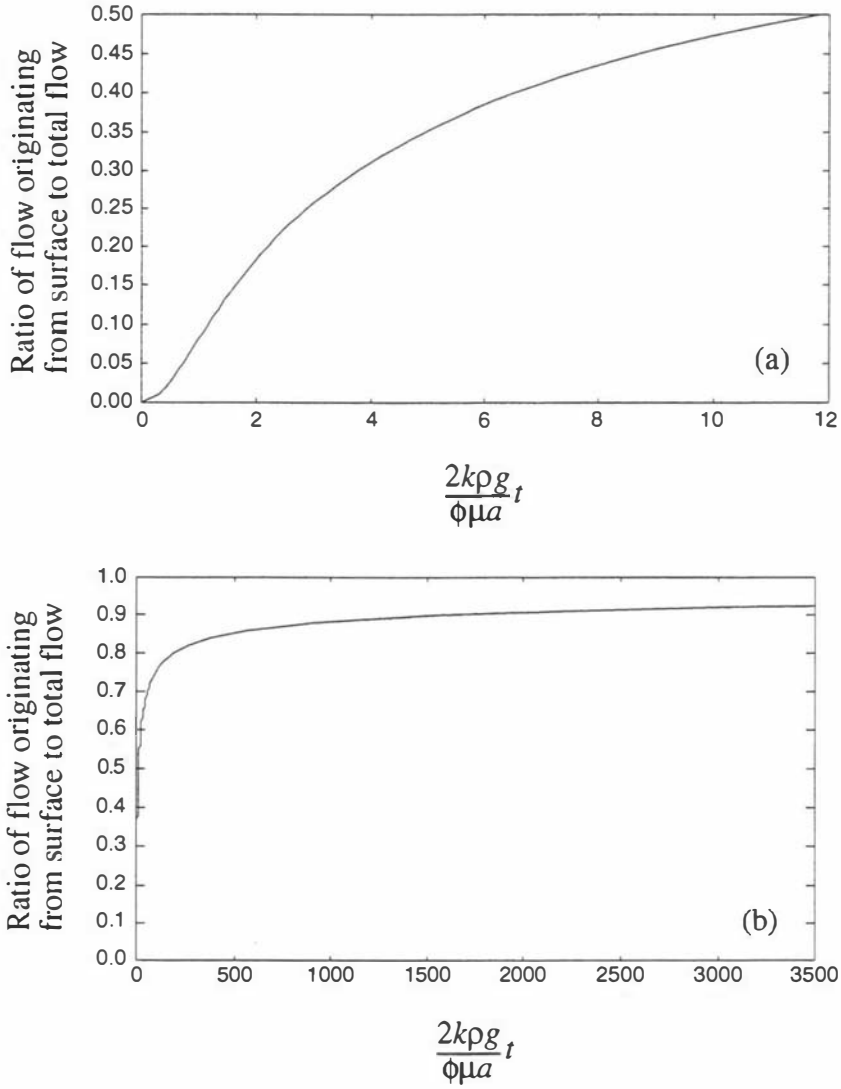

Figure 4.6: The ratio of the flow originating from the surface to the total flow is plotted in terms of a non-dimensionalized time. The ratio in Figure (a) is given over a relatively short "time scale" while in Figure (b) the ratio is shown over a relatively long "time period". (See text for further details.)

According to Equation 4.31, for a particular ratio, $F(r_0)$, of the flow originating from the surface to the total flow, the time period, $t(r_0, 2\pi)$, over which $F(r_0)$ is obtained is dependent on the properties of the porous medium, the temperature of the fluid, and the depth of the trench. In particular, $t(r_0, 2\pi)$ is proportional to $(\phi\mu a)/(k\rho)$. Therefore, an increase in the porosity of the porous medium or an increase in the depth of the trench, will increase the time it takes to obtain a given ratio $F(r_0)$. An increase in the permeability of the porous medium or in the temperature of the liquid water, will decrease the time it takes to obtain $F(r_0)$. (Note: The greater the temperature of the liquid water, the smaller the value of the fraction μ/ρ.)

The ratio of the flow originating from the surface to the total flow is plotted against the non-dimensionalized time $\frac{2A}{\phi a^3}t = \frac{2k\rho g}{\phi\mu a}t$ in Figure 4.6. During the very early stages of a given time period, Figure 4.6 shows that the majority of the fluid arriving at the trench was already in the ground at the beginning of the time period. Over time, the water beneath the surface is flushed by groundwater. (See Figures 4.5 and 4.6.)

In a hydrothermal eruption full steady-state flow will not be established. In such a non-isothermal case, as stated previously, we would expect the sources of the flow to be more local in character and the far field flow of the isothermal case to be inapplicable. Nevertheless, the present analysis may give some insight into how the ground flow will "recover" after an eruption. The replenishment of the depleted zone is likely to be from groundwater and not from depth. The hot water beneath the surface continues over time to be flushed by cool groundwater. This will have a cooling effect on the region and may explain long recovery times before subsequent eruptions.

4.2.1 Example Trench

An investigation of the flow to the trench in a particular case gives some insight into the time frames over which various aspects of the flow occur. Consider the case where the water is at $20°C$, the trench has a radius of $a = 1\ m$, and the porosity and permeability of the porous medium are given by $\phi = 0.10$ and $k = 10^{-11}\ m^2$ respectively. The "time to trench" isolines shown in Figure 4.5 (a) are separated by a time of 19.8 minutes for this case, while the isolines in Figure 4.5 (b) are separated by 0.845 days. Tables 4.1 and 4.2 give the time to trench, the ratio of the flow originating from the surface to the total flow, and the distances $r_x - a$ and $r_y - a$ for each of the "time to trench" isolines shown in Figures 4.5 (a) and (b) respectively. The plot of the ratio of the flow originating from the surface to the total flow verses time in this case is given in Figure 4.7. The distances $r_x - a$ and $r_y - a$ are plotted against time in Figure 4.8 and the ratios r_x/r_y

Table 4.1: Variables which describe where the flow is coming from during time periods associated with the isolines shown in Figure 4.5 (a) are given for the case $a = 1\ m$, $\phi = 0.10$, $k = 1 \times 10^{-11}\ m^2$, and $T = 20°C$.

time (min)	"time to trench" isoline in in Figure 4.5 (a)	ratio of flow from surface to total flow	$r_x - a$ (m)	$r_y - a$ (m)
19.8	1	0.213	0.27	0.65
39.6	2	0.338	0.51	1.00
59.4	3	0.412	0.70	1.25
79.2	4	0.462	0.86	1.46
99.0	5	0.498	0.99	1.64
118.8	6	0.526	1.11	1.80
138.6	7	0.548	1.21	1.94
158.4	8	0.567	1.31	2.07
178.2	9	0.583	1.40	2.19

Table 4.2: Variables which describe where the flow is coming from during time periods associated with the isolines shown in Figure 4.5 (b) are given for the case $a = 1\ m$, $\phi = 0.10$, $k = 1 \times 10^{-11}\ m^2$, and $T = 20°C$.

time (days)	"time to trench" isoline in in Figure 4.5 (b)	ratio of flow from surface to total flow	$r_x - a$ (m)	$r_y - a$ (m)
0.845	1	0.778	3.50	4.99
1.690	2	0.824	4.67	6.54
2.535	3	0.846	5.49	7.63
3.380	4	0.860	6.14	8.50
4.225	5	0.870	6.69	9.23
5.070	6	0.878	7.17	9.88
5.915	7	0.884	7.60	10.45
6.760	8	0.889	7.99	10.97
7.605	9	0.893	8.35	11.45
8.450	10	0.897	8.69	11.89

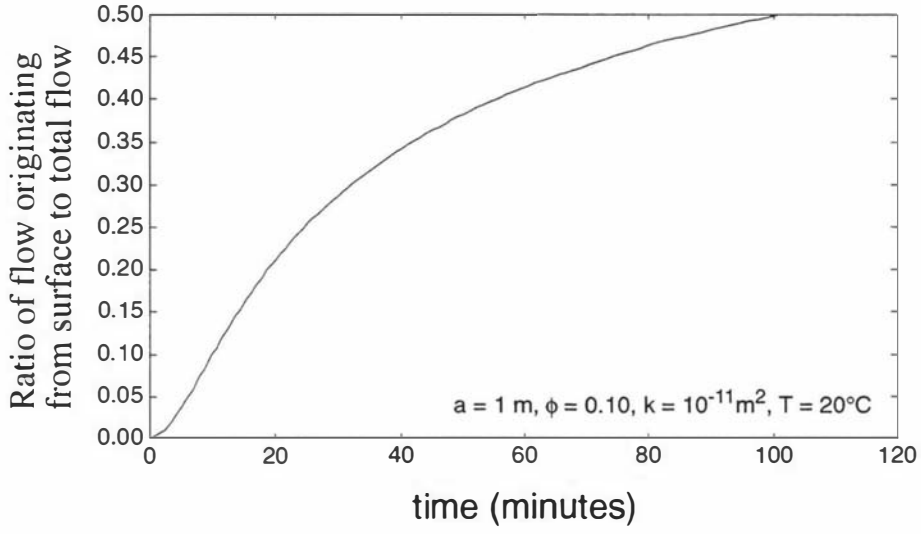

(a) The ratio of the flow originating from the surface to the total flow over a period of 2 hours.

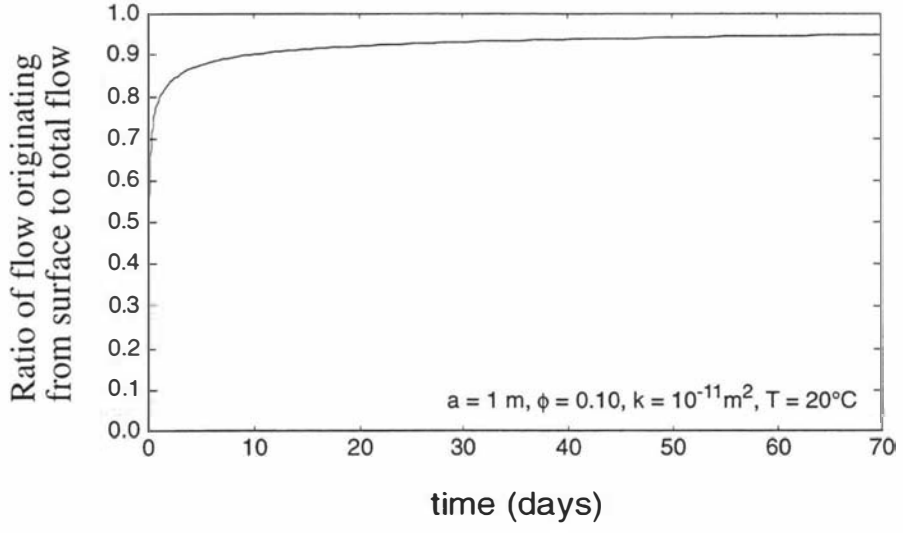

(b) The ratio of the flow originating from the surface to the total flow over a period of 70 days.

Figure 4.7: The ratio of the flow originating from the surface to the total flow is plotted against time for the case of a semi-circular horizontal trench with 1 m radius being dug from a porous medium with porosity $\phi = 0.10$ and permeability $k = 1 \times 10^{-11}\ m^2$. The fluid (liquid water) in the medium is assumed to be at a constant temperature of $20°C$. (See text for further details.)

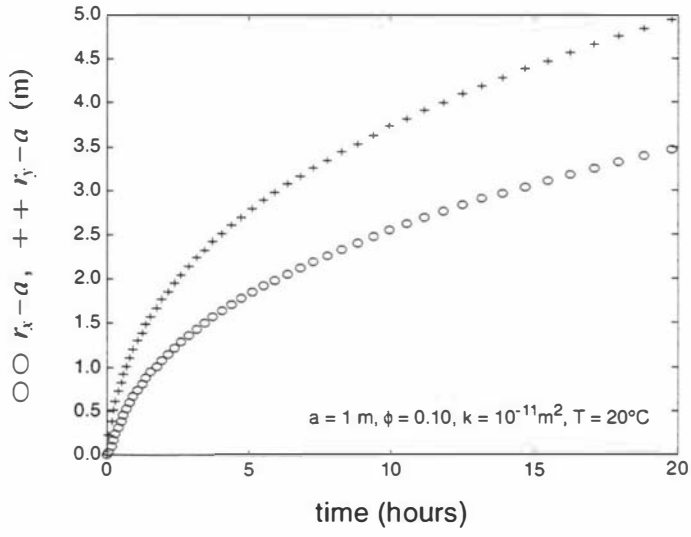

Figure 4.8: The distances $r_x - a$ and $r_y - a$ are plotted against time for the case of a semi-circular horizontal trench with 1 m radius being dug from a porous medium with porosity $\phi = 0.10$ and permeability $k = 1 \times 10^{-11}\ m^2$. The fluid (liquid water) in the medium is assumed to be at a constant temperature of $20°C$. (See text for further details.)

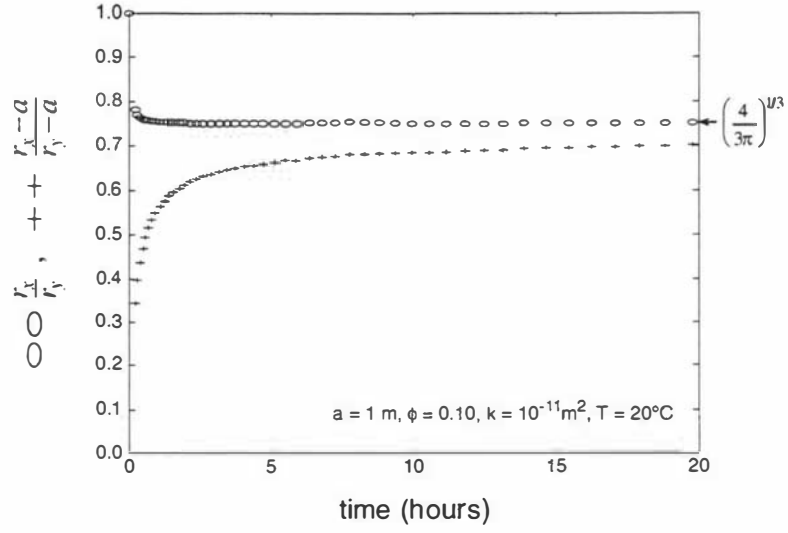

Figure 4.9: The ratios r_x/r_y and $(r_x - a)/(r_y - a)$ are plotted against time for the case of a semi-circular horizontal trench with 1 m radius being dug from a porous medium with porosity $\phi = 0.10$ and permeability $k = 1 \times 10^{-11}\ m^2$. The fluid (liquid water) in the medium is assumed to be at a constant temperature of $20°C$. (See text for further details.)

and $(r_x - a)/(r_y - a)$ are plotted against time in Figure 4.9.

For this case, all the fluid along the first time line in Figure 4.5 (a) will take approximately 19.8 minutes to reach the trench. After this time, only 21% of the flow will have come from the surface. (See Table 4.1.) Water will have come from a depth of 1.65 m (0.65 m from the trench), and from as far out as 1.27 m along the surface (0.27 m from the trench). Within an hour, the ratio r_x/r_y will have nearly reached its limit of approximately 0.7515. (See Figure 4.9.) After a period of approximately one hour and forty minutes, approximately half of the flow arriving at the trench will have begun at the surface. It will have come from a depth of 2.64 m (1.64 m from the trench), and from as far out as 1.99 m along the surface (0.99 m from the trench). After eight and a half days, nearly 90% of the flow will have originated from the surface. (See Table 4.2.) It will have come from a depth of up to 11.9 m from the bottom of the trench and from as far out as 8.7 m from the trench along the surface.

4.2.2 Numerical Solution

This problem has also been solved numerically for pressure and the mass flux potential function using finite difference methods. A simulation field of $a \leq r \leq 10a$ and $\pi \leq \theta \leq 3\pi/2$ with symmetry about $\theta = 3\pi/2$ was used. The results found match the analytic solution. The velocity potential is again given in terms of the mass flux potential by $\Phi = \Phi_m/\rho$.

Streamlines were found by plotting lines which were everywhere perpendicular to the velocity potential lines. The procedure for this follows: A point on the boundary, $(r_{init}, \theta_{init})$, was chosen from which to initiate a streamline. As the boundary is an equipotential line, $\Phi = 0$, any streamline must be perpendicular to the boundary. Hence, for some sufficiently small length ds, a second point on the streamline, $(r_{init} - ds, \theta_{init})$, was chosen. Subsequent points were found by first determining the closest point in the mesh, (r_i, θ_i), to the current point, (r, θ). Values for the potential function, Φ, at (r, θ_i), (r, θ_{i+1}), (r_i, θ) and (r_{i+1}, θ) were interpolated using finite difference methods and used to calculate the partial derivatives $\partial\Phi/\partial\theta$ and $\partial\Phi/\partial r$ by a forward difference. In polar co-ordinates

$$|\nabla\Phi| = \sqrt{\left(\frac{\partial\Phi}{\partial r}\right)^2 + \left(\frac{1}{r}\frac{\partial\Phi}{\partial\theta}\right)^2} \tag{4.32}$$

$$dr = \frac{\frac{\partial\Phi}{\partial r}ds}{|\nabla\Phi|} \tag{4.33}$$

$$d\theta = \frac{\frac{1}{r^2}\frac{\partial \Phi}{\partial \theta} ds}{|\nabla \Phi|} \tag{4.34}$$

Using Equations 4.32 - 4.34, the next point on the streamline was chosen to be $(r - dr, \theta - d\theta)$.

The results found for streamlines by this method also match the analytic solution. Streamlines, isobars and equipotential lines for the numerical solution are not shown here as no difference may be detected between these and those found by analytical solution given in Figures 4.2, 4.3 and 4.4.

It should be noted that this simple, but effective, method used for plotting the streamlines in this case may also eventually prove useful in solving the steady non-isothermal case. Once the conservation equations have been solved for either h_f or $\mathbf{Q}_m$, the orthogonality of ∇h_f and $\mathbf{Q}_m$ (see Equation 3.22) may be used to complete the solution.

4.3 Hemi-spherical hole

Next, consider the case of digging a hemi-spherical hole for the extraction of water. The radius of the hole is a and conditions are ambient at some distance b from the centre of the hole. The solution to the flow in this problem can be found by solving Laplace's equation in spherical co-ordinates with symmetry about the vertical axis. (See Figure 4.10.)

Laplace's equation in spherical co-ordinates with axial symmetry is given for the potential $\Phi_m(r, \theta)$ by

$$\frac{\partial}{\partial r}\left(r^2 \frac{\partial \Phi_m}{\partial r}\right) + \frac{1}{\sin\theta}\frac{\partial}{\partial \theta}\left(\sin\theta \frac{\partial \Phi_m}{\partial \theta}\right) = 0 \tag{4.35}$$

where r is the radial distance from the origin and θ is measured from the vertical axis of symmetry, $a \leq r \leq b$, $\pi/2 \leq \theta \leq \pi$. (See Figure 4.10.) The boundary conditions in this case become

$$\begin{aligned} &\Phi_m\left(r, \tfrac{\pi}{2}\right) = \tfrac{\partial \Phi_m}{\partial \theta}(r, \pi) = 0 && \text{for } a \leq r \leq b \\ &\Phi_m(a, \theta) = \tfrac{-k\rho g z}{\nu} = \tfrac{-k\rho g a \cos\theta}{\nu}, \ \Phi_m(b, \theta) = 0 && \text{for } \tfrac{\pi}{2} \leq \theta \leq \pi \end{aligned} \tag{4.36}$$

The analytic solution to Equation 4.35 with boundary conditions 4.36 is

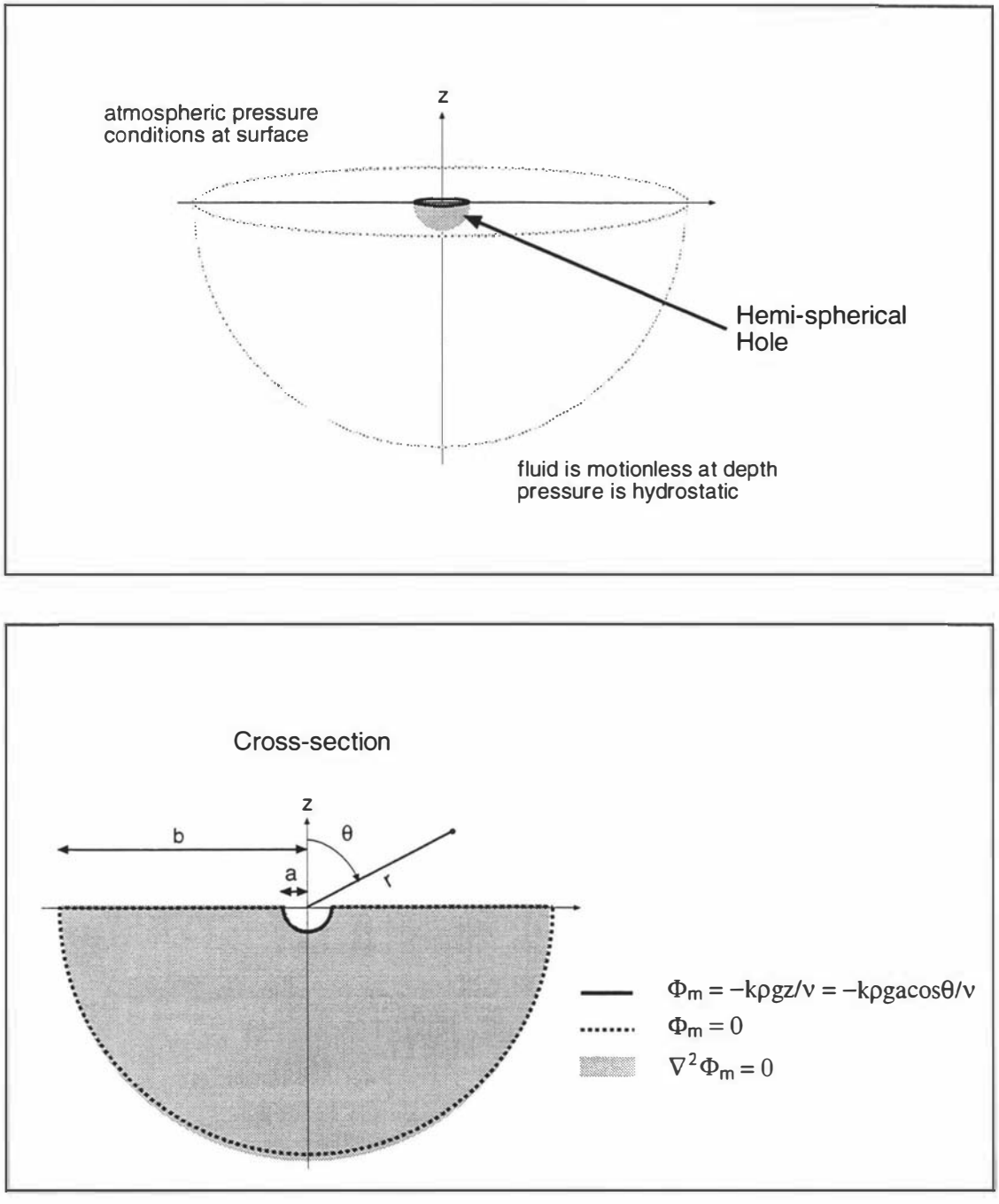

Figure 4.10: Hemi-spherical hole dug for extracting water. A cross-section of the ground region, illustrating boundary conditions for the flow problem, is shown. (See text in Section 4.3 for details.)

$$\Phi_m = \frac{k\rho g a^3}{\nu(b^3 - a^3)} \left(\frac{r^3 - b^3}{r^2} \right) \cos\theta \tag{4.37}$$

By Equation 4.2 the mass flux then becomes

$$\mathbf{Q}_m = \frac{k\rho g a^3}{\nu(b^3 - a^3)} \left[\left(\frac{r^3 + 2b^3}{r^3} \right) \cos\theta \mathbf{e_r} + \left(\frac{b^3 - r^3}{r^3} \right) \sin\theta \mathbf{e}_\theta \right] \tag{4.38}$$

The total mass flux into the hole, Q, is then found by integrating the radial component of the mass flux vector, to give

$$Q = \frac{k\rho g \pi a^2}{\nu} \frac{a^3 + 2b^3}{b^3 - a^3} \tag{4.39}$$

The mass stream function, Ψ_m, which is related to the mass flux by

$$\mathbf{Q}_m = \frac{1}{r^2 \sin\theta} \frac{\partial \Psi_m}{\partial \theta} \mathbf{e_r} - \frac{1}{r \sin\theta} \frac{\partial \Psi_m}{\partial r} \mathbf{e}_\theta \tag{4.40}$$

may be found for this case in the form

$$\Psi_m = \frac{k\rho g a^3}{\nu(b^3 - a^3)} \left(\frac{r^3 + 2b^3}{2r} \right) \sin^2\theta \tag{4.41}$$

The velocity potential, Φ, and stream-function, Ψ, for the flow are then given by

$$\Phi = \frac{\Phi_m}{\rho} = \frac{k\rho g a^3}{\mu(b^3 - a^3)} \left(\frac{r^3 - b^3}{r^2} \right) \cos\theta \tag{4.42}$$

$$\Psi = \frac{\Psi_m}{\rho} = \frac{k\rho g a^3}{\mu(b^3 - a^3)} \left(\frac{r^3 + 2b^3}{2r} \right) \sin^2\theta \tag{4.43}$$

As the outer radius b of the solution region becomes large, for finite r

$$\Phi \rightarrow -\frac{k\rho g a^3}{\mu}\frac{1}{r^2}\cos\theta \tag{4.44}$$

$$\mathbf{Q}_m \rightarrow \frac{k\rho g a^3}{\nu}\left(\frac{2}{r^3}\cos\theta\mathbf{e_r} + \frac{1}{r^3}\sin\theta\mathbf{e}_\theta\right) \tag{4.45}$$

$$Q \rightarrow \frac{2k\rho g\pi a^2}{\nu} \tag{4.46}$$

$$\Psi \rightarrow \frac{k\rho g a^3}{\mu}\frac{1}{r}\sin^2\theta \tag{4.47}$$

$$p \rightarrow p_{atm} + \rho g\left(\frac{a^3}{r^2} - r\right)\cos\theta \tag{4.48}$$

Note that in this case Q is proportional to the square of the depth of the hole, a^2.

Investigation into the convergence of the flow near the hole shows that

$$\frac{Q}{Q \text{ as } b\rightarrow\infty} = \frac{\Psi(a,\theta)}{\Psi(a,\theta) \text{ as } b\rightarrow\infty} = \frac{a^3+2b^3}{2(b^3-a^3)} \tag{4.49}$$

Therefore, an outer radius of $b = 10a$ is sufficient for numerical and analytic solutions to agree to within about 1%.

The cross-section of the stream surfaces and cross-section of isobaric surfaces are given in Figures 4.11 and 4.12 respectively. These were calculated on the simulation field $a \leq r \leq b = 10a$, and an enlargement of the region out to $r = 2.5a$ is also shown. Characteristics similar to those found in Figures 4.2 and 4.3 can be seen in Figures 4.11 and 4.12. The equipotential lines, as expected, are again found to be everywhere perpendicular to the streamlines. (See Figure 4.13).

This problem was also solved numerically for pressure and the mass flux potential function using finite difference methods. The stream-function was then found numerically in a manner similar to that described in Section 4.2.2. Results again match those found analytically.

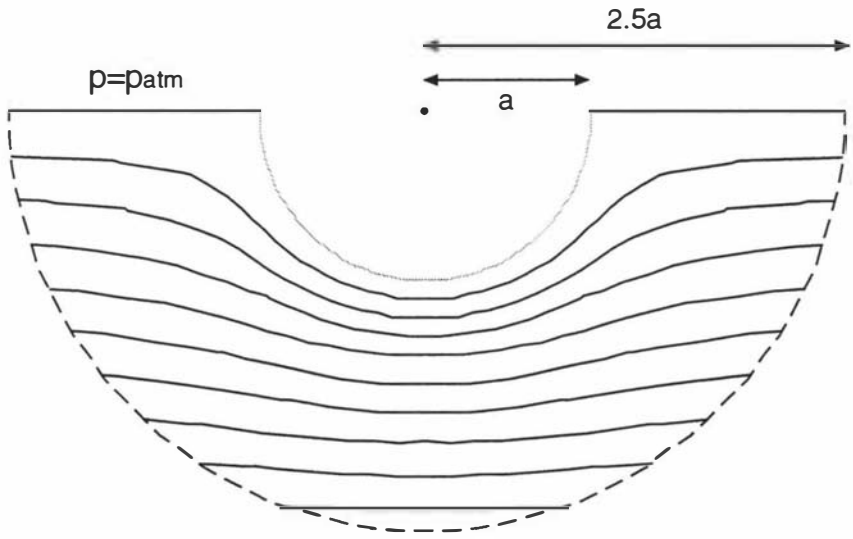

(a) Cross-section of isobaric surfaces, region out to $r = 2.5a$ depicted.

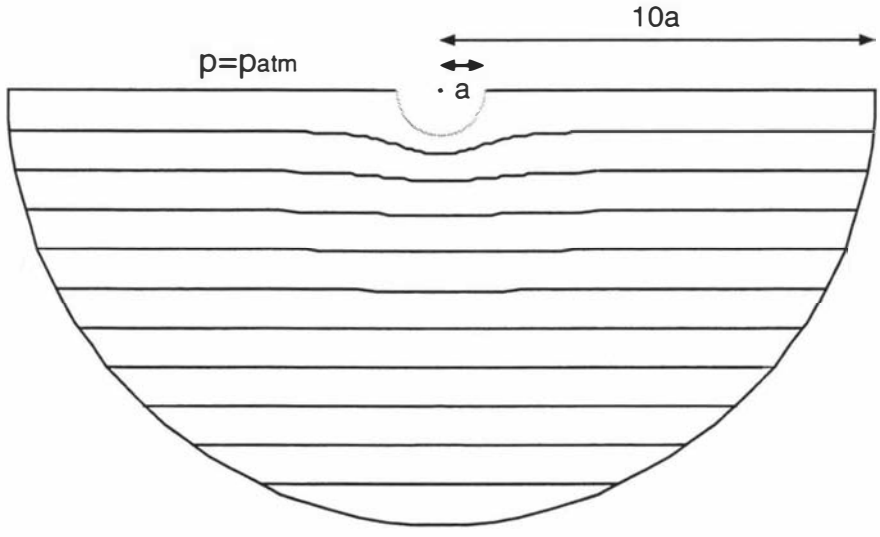

(b) Cross-section of isobaric surfaces shown over simulation field $a \leq r \leq 10a$.

Figure 4.11: Isolines for pressure for hemi-spherical hole. (See text for details.)

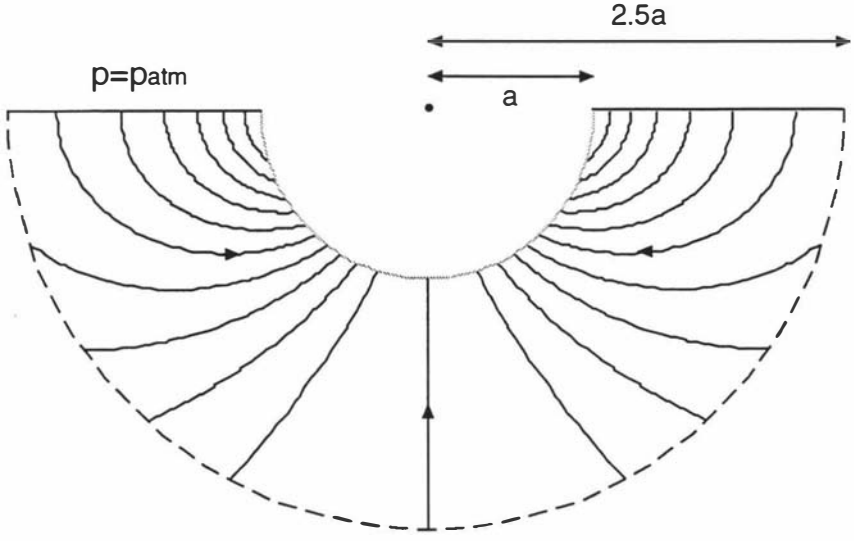

(a) Cross-section of stream surfaces, region out to $r = 2.5a$ depicted.

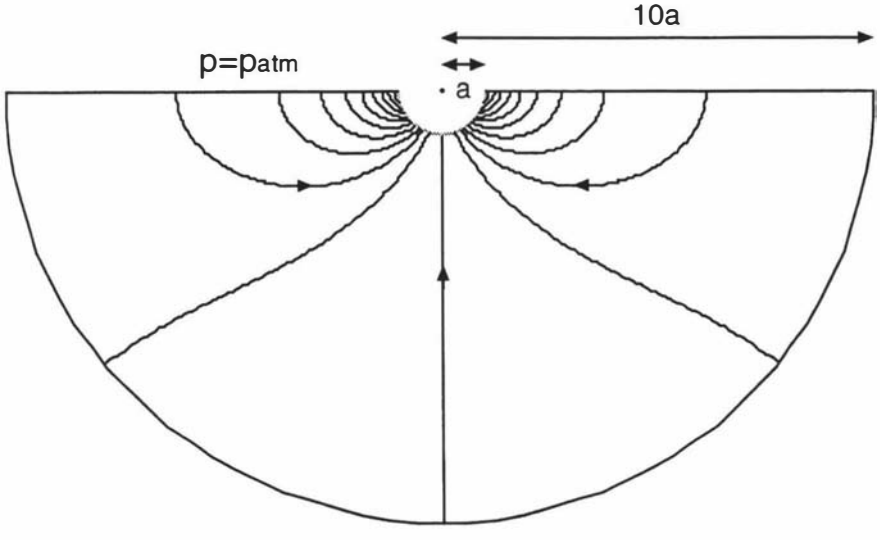

(b) Cross-section of stream surfaces shown over simulation field $a \leq r \leq 10a$.

Figure 4.12: Isolines for stream-function for hemi-spherical hole. (See text for details.)

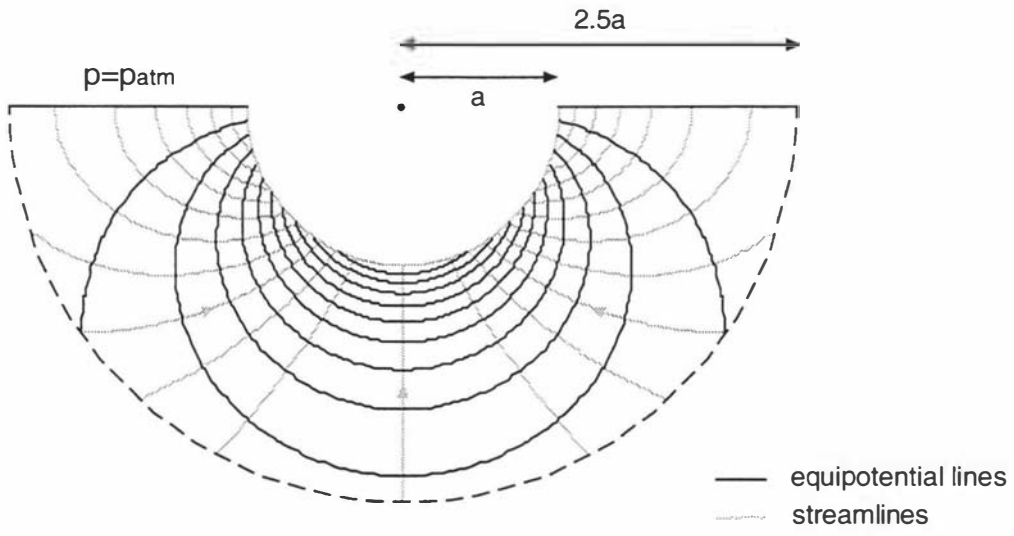

Figure 4.13: Equipotential and streamlines for hemi-spherical hole. Region out to $r = 2.5a$ depicted. (See text for details.)

From Equation 4.43, the ratios of the flow originating from the surface to the total flow, and that from the subsurface to the total, are given by

$$\frac{\Psi\left(a,\pi/2\right)-\Psi\left(b,\pi/2\right)}{\Psi(a,\pi/2)-\Psi\left(a,\pi\right)} = 1-\frac{3ab^2}{a^3+2b^3} \tag{4.50}$$

$$\frac{\Psi\left(b,\frac{\pi}{2}\right)-\Psi\left(b,\pi\right)}{\Psi(a,\pi/2)-\Psi\left(a,\pi\right)} = \frac{3ab^2}{a^3+2b^3} \tag{4.51}$$

For the case $b = 10a$ illustrated in Figure 4.12, 85% of the flow originates from the surface while 15% is derived from groundwater. However, as the outer radius b for the solution region becomes large, Equations 4.50 and 4.51 show that, in the long term, all of the flow originates from the surface.

As the outer radius b of the solution region becomes large, the travel time from a point (r_0, θ_0), to the hole may be calculated in the following way: Equation 4.47 may be written in the form

$$\Psi = B\frac{1}{r}\sin^2\theta \tag{4.52}$$

where

$$B = \frac{k\rho g a^3}{\mu} \tag{4.53}$$

The component of the Darcy velocity of the flow in the radial direction is given by

$$v_r = \frac{1}{r^2 \sin\theta}\frac{\partial \Psi}{\partial \theta} = \frac{2B}{r^3}\cos\theta \tag{4.54}$$

For $\theta_0 \neq \pi$, combining and rearranging Equations 4.52 and 4.54 gives

$$\begin{aligned} {v_r}^2 + \frac{4B\Psi}{r^5} &= \frac{4B^2}{r^6} \\ {v_r}^2 &= \frac{4B^2}{r^6} - \frac{4B^2}{r^5}\frac{\sin^2\theta_0}{r_0} \end{aligned} \tag{4.55}$$

Using Equations 4.25 and 4.55 for $\pi/2 \leq \theta_0 < \pi$ and Equations 4.25 and 4.54 for $\theta_0 = \pi$, the radial pore-averaged velocity, u_r, may be written in the form

$$u_r = \frac{dr}{dt} = \begin{cases} -\frac{2B}{\phi}\frac{1}{r^3}\left(1 - \frac{\sin^2\theta_0}{r_0}r\right)^{1/2} & \pi/2 \leq \theta_0 < \pi \\ -\frac{2B}{\phi r^3} & \theta_0 = \pi \end{cases} \tag{4.56}$$

Integration of Equation 4.56 on the interval $a \leq r \leq r_0$ gives

$$\frac{2B}{\phi}t = \begin{cases} \frac{r_0^4}{\sin^8\theta_0}\left[\frac{2}{7}\cos^7\theta_0 - \frac{6}{5}\cos^5\theta_0 + 2\cos^3\theta_0 - 2\cos\theta_0 \right. \\ \quad -\frac{2}{7}\left(1 - \frac{a}{r_0}sin^2\theta_o\right)^{\frac{7}{2}} + \frac{6}{5}\left(1 - \frac{a}{r_0}sin^2\theta_o\right)^{\frac{5}{2}} \\ \quad \left. -2\left(1 - \frac{a}{r_0}sin^2\theta_o\right)^{\frac{3}{2}} + 2\left(1 - \frac{a}{r_0}sin^2\theta_o\right)^{\frac{1}{2}}\right] & \pi/2 \leq \theta_0 < \pi \\ \frac{({r_0}^4 - a^4)}{4} & \theta_0 = \pi \end{cases} \tag{4.57}$$

Equation 4.57 can then be used to plot isolines for the "time to hole". (See Figure 4.14.)

As was the case in the semi-circular horizontal trench, for this hemi-spherical hole the flow is always "digging deeper" from beneath the bottom of the trench than it is "reaching out" from the sides of the trench. (See Figure 4.14.) Using Equation 4.57, it can be shown that the ratio r_x/r_y for this hemi-spherical hole is again always less than or equal to one and decreases with time t, tending in this case to the value $\frac{1}{2}\left(\frac{35}{8}\right)^{1/4} \approx 0.7231$ for large times t. The ratio $(r_x - a)/(r_y - a)$ increases with time t and also tends to the value $\frac{1}{2}\left(\frac{35}{8}\right)^{1/4}$.

Using Equation 4.47, the ratio of the flow originating from the surface to the total flow during the time it takes for the fluid originating at $(r_0, \pi/2)$ to reach the trench is given by

$$F = \frac{\Psi(r_0, \pi/2) - \Psi(a, \pi/2)}{\Psi(a, \pi) - \Psi(a, \pi/2)} = 1 - \frac{a}{r_0} \tag{4.58}$$

Using Equations 4.57 and 4.58, the following equation for time as a function of F is obtained.

$$\frac{2B}{\phi a^4} t = \frac{-\frac{2}{7}F^{7/2} + \frac{6}{5}F^{5/2} - 2F^{3/2} + 2F^{1/2}}{(1-F)^4} \tag{4.59}$$

The ratio of the flow originating from the surface to the total flow is plotted against time for both the hemi-spherical hole and the semi-circular horizontal trench in Figure 4.15. A comparison of the two cases shows the overall pattern of the "recharge" of the system is the same in both cases. During the very early stages of a given time period, the majority of the fluid arriving at the trench was already in the ground at the beginning of the time period. Over time, the water beneath the surface is flushed by groundwater. However, if a hemi-spherical hole and a semi-circular horizontal trench, both of equal depth, are dug from porous mediums of equal porosity and permeability, and if the fluid in both porous mediums is at the same temperature, the ratio of the flow originating from the surface to the total flow is initially greater in the hemi-spherical hole than it is in the horizontal trench. In other words, in the short term, the hemi-spherical hole is being "quenched" faster than the horizontal trench. It does not take long, however, before the ratio of the flow coming from the surface to the total flow is greater in the horizontal trench than in the hemi-spherical hole. (See Figure 4.15.)

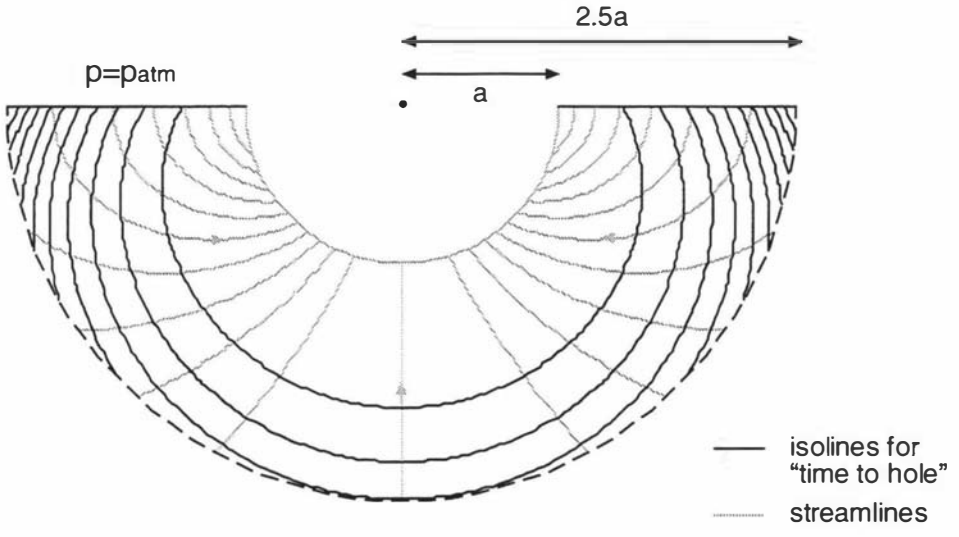

(a) Cross-section of "time to hole" surfaces, region out to $r = 2.5a$ depicted.

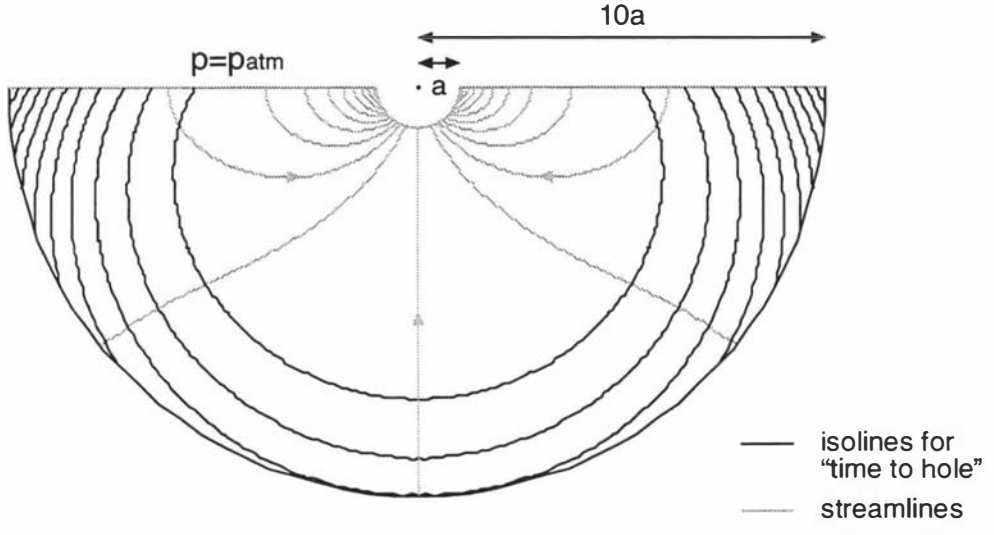

(b) Cross-section of "time to hole" surfaces shown over simulation field $a \leq r \leq 10a$.

Figure 4.14: Isolines for "time to hole" and streamlines for hemi-spherical hole. All fluid on a given "time to hole" isoline will reach the surface of the hole at the same time. (See text for further details.)

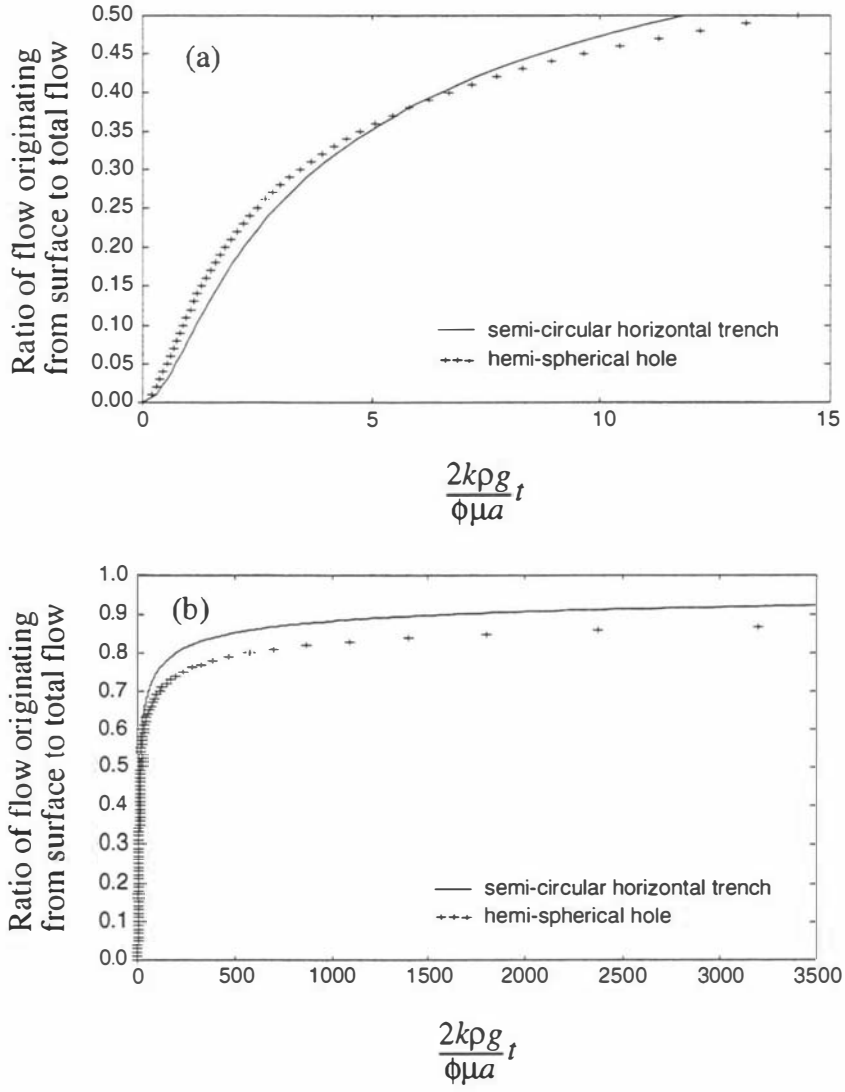

Figure 4.15: The ratio of the flow originating from the surface to the total flow is plotted in terms of a non-dimensionalized time for both the semi-circular horizontal trench and the hemi-spherical hole. The ratio in Figure (a) is given over a relatively short "time scale" while in Figure (b) the ratio is shown over a relatively long "time period". (See text for further details.)

4.3.1 Example Hemi-Spherical Hole

In this section, an investigation is made into the flow to a hemi-spherical hole of radius 1 m dug from a porous medium filled with liquid water at a temperature of $20°C$. The porous medium is assumed to have a porosity of $\phi = 0.10$ and a permeability of $k = 1 \times 10^{-11}\ m^2$. Comparisons between the flow to this hemi-spherical hole and the example horizontal trench described in Section 4.2.1 are made. (Note that the radius of the example horizontal trench is the same as the radius of the example hemi-spherical hole and that both are dug from porous mediums of equal porosity and permeability. The liquid water flowing through both porous mediums is also at the same temperature.)

The "time to hole" isolines shown in Figure 4.14 (a) are separated by a time of 26.6 minutes for this example hemi-spherical hole case, while the isolines in Figure 4.14 (b) are separated by 4.9 days. Tables 4.3 and 4.4 give the time to trench, the ratio of the flow originating from the surface to the total flow, and the distances $r_x - a$ and $r_y - a$ for each of the "time to hole" isolines shown in Figures 4.14 (a) and (b) respectively.

The ratio of the flow originating from the surface to the total flow is plotted against time for both the example horizontal trench and example hemi-spherical hole in Figure 4.16. As stated in the general case, the ratio of the flow originating from the surface to the total flow is initially greater in the hemi-spherical hole than it is in the horizontal trench. Figure 4.16 (a) shows, for this particular case, the time at which the ratio of the flow originating from the surface to the total flow becomes larger for the horizontal trench is approximately 50 minutes.

The distances $r_x - a$ and $r_y - a$ are plotted against time for both the hemi-spherical hole and the horizontal trench in Figure 4.17. In the short term (over the first two hours), Figure 4.17 (a) shows that the depths to which the flow is "digging", $r_y - a$, and distances to which the flow is "reaching out", $r_x - a$, are very similar for both cases. Initially, both distances are slightly larger for the hemi-spherical hole than the horizontal trench. However, the distance to which the flow is "reaching out" becomes greater for the trench within the first hour, and the depth to which the flow is "digging" becomes greater for the trench after about 1.5 hours. In the long term, over a period of several days, both distances are significantly greater for the horizontal trench than they are for the hemi-spherical hole and the differences between the two continues to grow with time. [See Figure 4.17 (b).]

The ratios r_x/r_y and $(r_x - a)/(r_y - a)$ are plotted against time for the hemi-spherical hole in Figure 4.18. Within an hour the ratio r_x/r_y is already approximately 0.7231, the limit of r_x/r_y as time becomes large. This is similar to the time scale taken for the ratio r_x/r_y in the horizontal trench to approach its limit of approximately 0.7515.

Table 4.3: Variables which describe where the flow is coming from during time periods associated with the isolines shown in Figure 4.14 (a) are given for the case $a = 1\ m$, $\phi = 0.10$, $k = 1 \times 10^{-11}\ m^2$, and $T = 20°C$.

time (min)	"time to hole" isoline in in Figure 4.14 (a)	ratio of flow from surface to total flow	$r_x - a$ (m)	$r_y - a$ (m)
26.6	1	0.286	0.40	0.92
53.2	2	0.390	0.64	1.26
79.8	3	0.448	0.81	1.49
106.4	4	0.485	0.94	1.67
133.0	5	0.510	1.04	1.82
159.6	6	0.533	1.14	1.95
186.2	7	0.550	1.22	2.06
212.8	8	0.563	1.29	2.17
239.4	9	0.576	1.36	2.26
266.0	10	0.587	1.42	2.35

Table 4.4: Variables which describe where the flow is coming from during time periods associated with the isolines shown in Figure 4.14 (b) are given for the case $a = 1\ m$, $\phi = 0.10$, $k = 1 \times 10^{-11}\ m^2$, and $T = 20°C$.

time (days)	"time to hole" isoline in in Figure 4.14 (b)	ratio of flow from surface to total flow	$r_x - a$ (m)	$r_y - a$ (m)
4.9	1	0.818	4.49	6.59
9.8	2	0.847	5.52	8.02
14.7	3	0.861	6.22	8.98
19.6	4	0.871	6.76	9.73
24.5	5	0.878	7.20	10.34
29.4	6	0.884	7.59	10.87
34.3	7	0.888	7.92	11.34
39.2	8	0.892	8.23	11.76
44.1	9	0.895	8.50	12.14
49.0	10	0.898	8.76	12.49

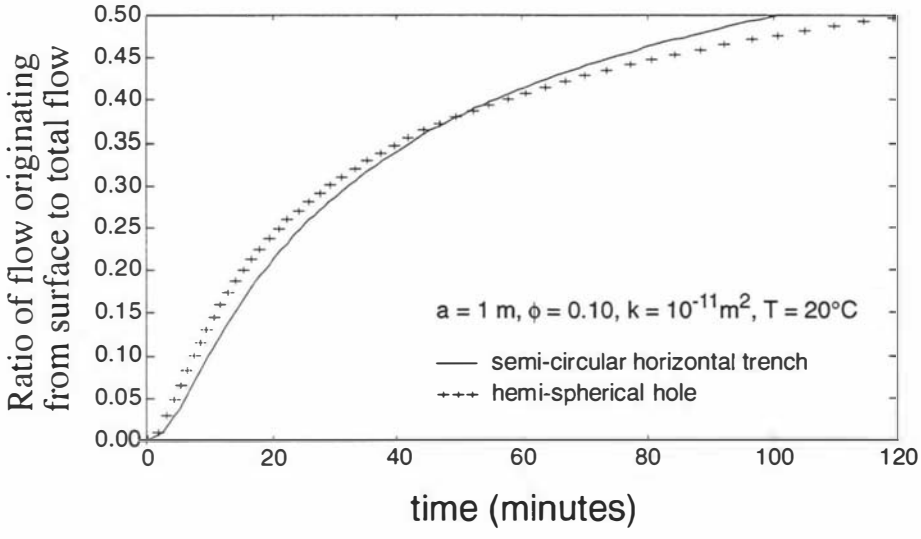

(a) The ratio of the flow originating from the surface to the total flow over a period of 2 hours.

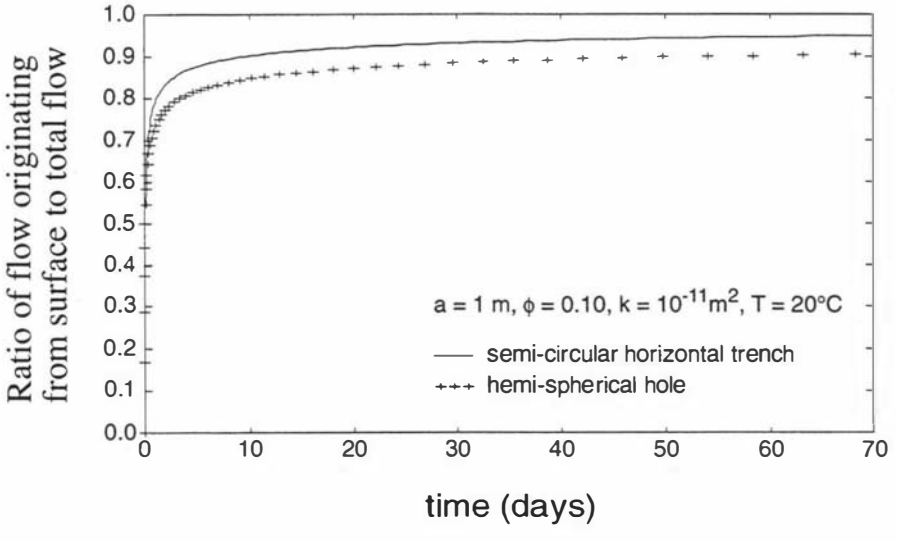

(b) The ratio of the flow originating from the surface to the total flow over a period of 70 days.

Figure 4.16: The ratio of the flow originating from the surface to the total flow is plotted against time for the cases of a semi-circular horizontal trench and a hemi-spherical hole, both with 1 m radius being dug from a porous medium with porosity $\phi = 0.10$ and permeability $k = 1 \times 10^{-11}\ m^2$. The fluid (liquid water) in the medium is assumed to be at a constant temperature of $20°C$. (See text for further details.)

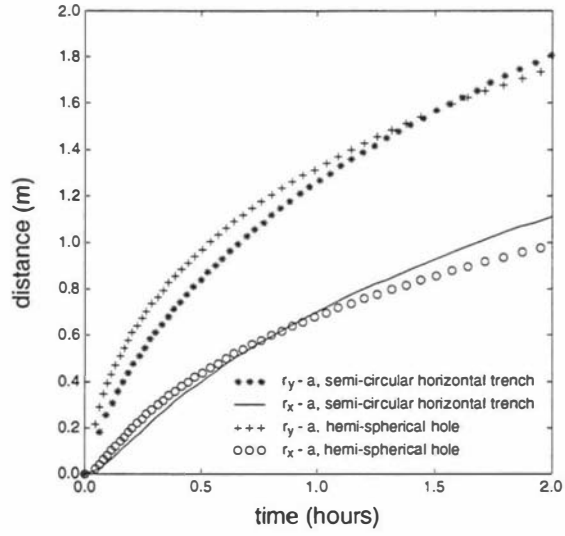

(a) The distances $r_x - a$ and $r_y - a$ over a period of 2 hours.

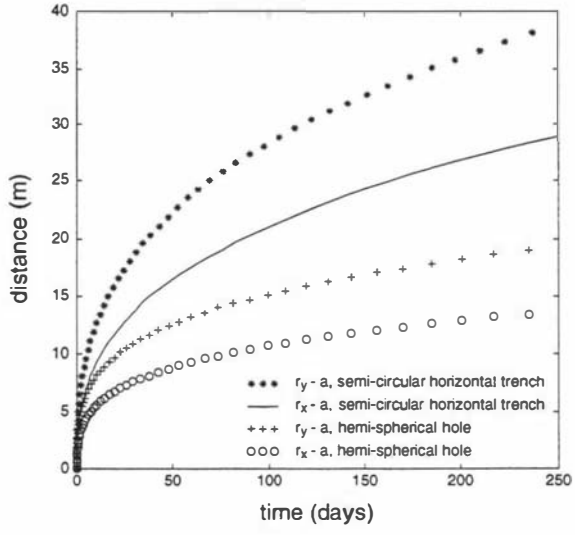

(b) The distances $r_x - a$ and $r_y - a$ over a period of 250 days.

Figure 4.17: The distances $r_x - a$ and $r_y - a$ are plotted against time for the cases of a semi-circular trench and a hemi-spherical hole, each with 1 m radius being dug from a porous medium with porosity $\phi = 0.10$ and permeability $k = 1 \times 10^{-11}\ m^2$. The fluid (liquid water) in the medium is assumed to be at a constant temperature of $20°C$. (See text for further details.)

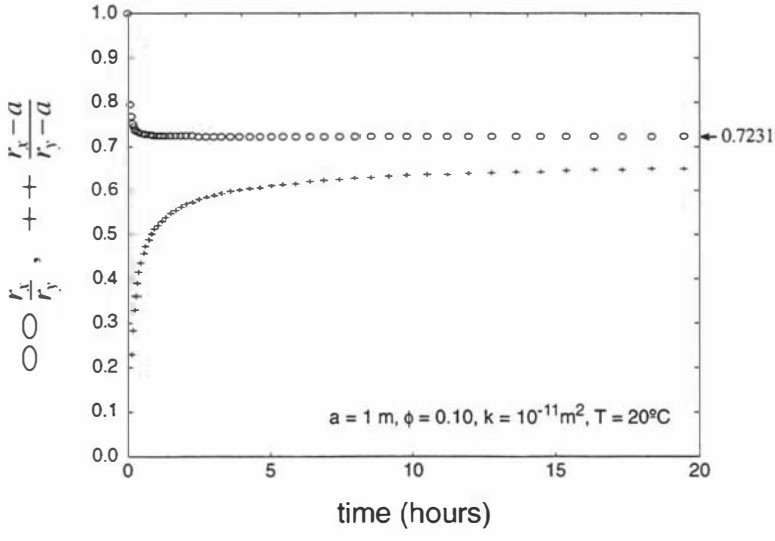

Figure 4.18: The ratios r_x/r_y and $(r_x - a)/(r_y - a)$ are plotted against time for the case of a hemi-spherical hole with 1 m radius being dug from a porous medium with porosity $\phi = 0.10$ and permeability $k = 1 \times 10^{-11}\ m^2$. The fluid (liquid water) in the medium is assumed to be at a constant temperature of $20°C$. (See text for further details.)

4.4 Cylindrical hole

Finally, consider the case of sinking a cylindrical hole for the purpose of gathering groundwater. The hole has radius a and depth d. It is assumed that conditions are ambient (hydrostatic) on a cylindrical surface with radius b from the centre of the hole and with depth D from the surface. (See Figure 4.19.) The solution to the flow in this problem can be found by solving Laplace's equation, Equation 4.4, in cylindrical coordinates with symmetry about the vertical axis.

Laplace's equation in cylindrical co-ordinates with axial symmetry is given for the mass flux potential $\Phi_m(r, z)$ by

$$\frac{1}{r}\frac{\partial}{\partial r}\left(r\frac{\partial \Phi_m}{\partial r}\right) + \frac{\partial^2 \Phi_m}{\partial z^2} = 0 \tag{4.60}$$

where r is the distance from the vertical z-axis. The boundary conditions in this case become

$$\begin{array}{ll}
\Phi_m(b, z) = 0 & \text{for } -D \leq z \leq 0 \\
\Phi_m(r, -D) = 0 & \text{for } 0 \leq r \leq b \\
\Phi_m(r, 0) = 0 & \text{for } a \leq r \leq b \\
\Phi_m(a, z) = -\frac{k}{\nu}\rho g z & \text{for } -d \leq z \leq 0 \\
\Phi_m(r, -d) = \frac{k}{\nu}\rho g d & \text{for } 0 \leq r \leq a \\
\frac{\partial \Phi_m}{\partial r}(0, z) = 0 & \text{for } -D \leq z \leq -d
\end{array} \tag{4.61}$$

The mass stream-function for this case can be found by solving

$$\frac{\partial^2 \Psi_m}{\partial r^2} - \frac{1}{r}\frac{\partial \Psi_m}{\partial r} + \frac{\partial^2 \Psi_m}{\partial z^2} = 0 \tag{4.62}$$

for $\Psi_m(r, z)$ with the boundary conditions

$$\begin{array}{ll}
\frac{\partial \Psi_m}{\partial r}(b, z) = 0 & \text{for } -D \leq z \leq 0 \\
\frac{\partial \Psi_m}{\partial z}(r, -D) = 0 & \text{for } 0 \leq r \leq b \\
\frac{\partial \Psi_m}{\partial z}(r, 0) = 0 & \text{for } a \leq r \leq b \\
\frac{\partial \Psi_m}{\partial r}(a, z) = -\frac{k}{\nu}\rho g a & \text{for } -d \leq z \leq 0 \\
\frac{\partial \Psi_m}{\partial z}(r, -d) = 0 & \text{for } 0 \leq r \leq a \\
\frac{\partial \Psi_m}{\partial z}(0, z) = 0 & \text{for } -D \leq z \leq -d
\end{array} \tag{4.63}$$

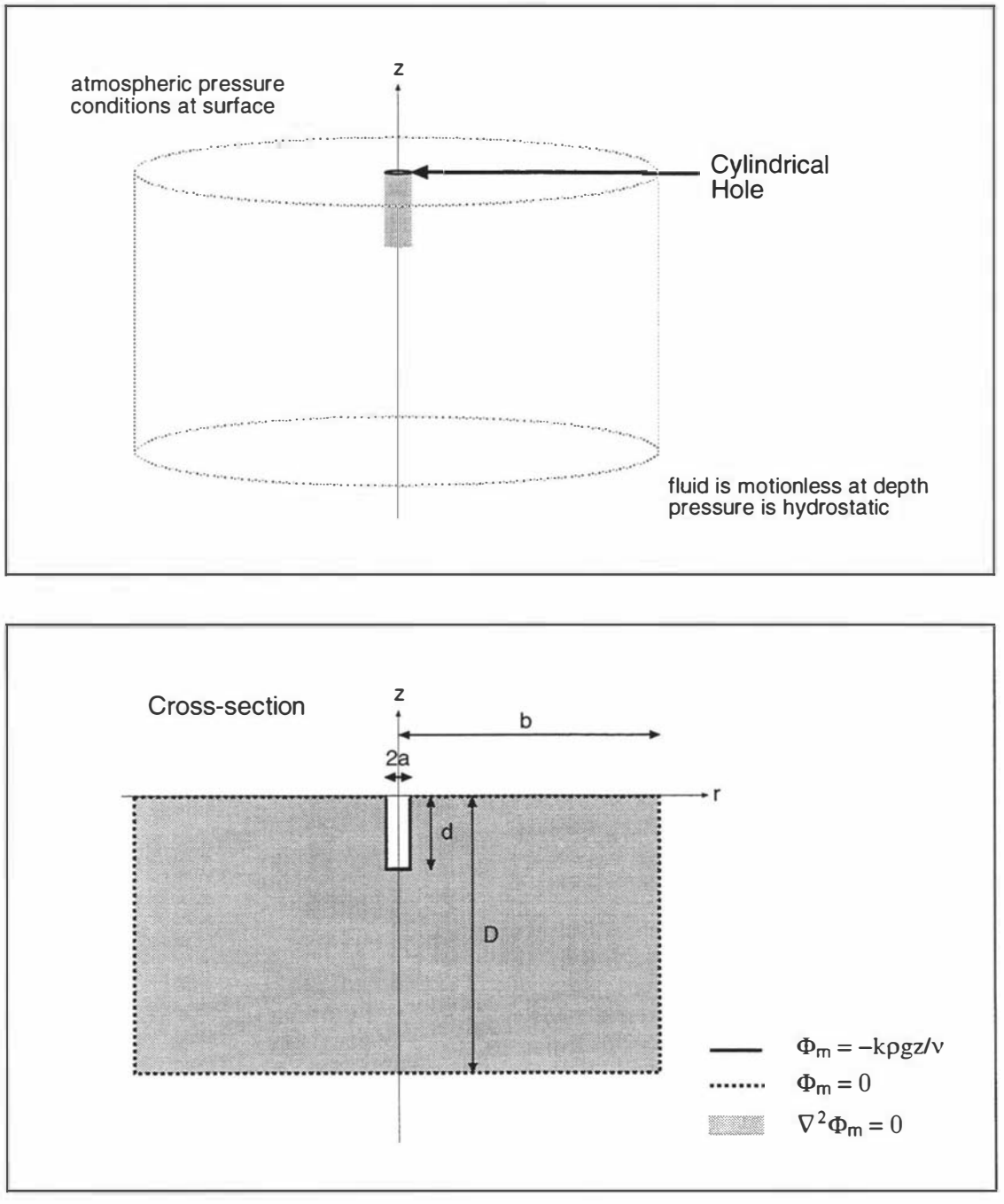

Figure 4.19: Cylindrical hole dug for extracting water. A cross-section of the ground region, illustrating boundary conditions for the flow problem, is shown. (See text in Section 4.4 for details.)

Equation 4.60, with boundary conditions 4.61, and Equation 4.62, with boundary conditions 4.63, were solved numerically using finite difference methods. The isobars (cross-section of the isobaric surfaces) and streamlines (cross-sections of the stream surfaces) are shown in Figures 4.20 (a) and 4.20 (b). Guided by the considerations for the previous two geometric configurations, a numerical solution was found on a domain with a radius and depth of ten times the depth of the hole, d. The radius of the hole, a, was chosen to be small in comparison to its depth, d. (In the case shown in Figure 4.20, $d = 10a$.) This was done in an effort to simulate a crack or fissure in the ground. The region out to $r = 2.5d$ and down to $z = -2.5d$ is depicted.

For this cylindrical case, ($d = 10a$, $b = D = 10d$), 90% of the flow originates from the surface while 10% is derived from groundwater. From results found in both the horizontal trench and hemi-spherical hole, we would expect that as the outer radius b and the depth D for the solution region becomes large, all of the flow would originate from the surface. Calculations also show that for this case, ($d = 10a$, $b = D = 10d$), 86% of the flow emerging from the hole comes from the sides, while only 14% comes from the bottom.

A simulation using the groundwater flow simulator HYDROTHERM (Hayba and Ingebritsen 1994) was carried out for comparison with the numerical results for this cylindrical case. The calculations were performed on a simulation field of $0 \leq r \leq 10\ m$ and $-10 \leq z \leq 0\ m$. The porosity and permeability of the porous medium were uniform and given by 0.10 and $1 \times 10^{-10}\ m^2$ respectively. Atmospheric conditions ($p = 1\ bar$ and $T = 20°C$) were placed on the ground surface ($z = 0$) and the fluid in the porous medium was at a constant temperature ($20°C$) and had an initial pressure distribution determined by a hydrostatic pressure gradient. A cylindrical hole of radius $0.1\ m$ and depth $1\ m$ was then removed from the formation. Constant atmospheric temperature and pressure boundary conditions were placed on the surface and along the "hole boundary", while "no flux" conditions were placed on the basal and lateral boundaries. Figure 4.21 (a) shows a comparison of the isobars for the Laplace Equation numerical solution and for the HYDROTHERM simulation once it had reached steady state. The main pressure reduction is shown to be local in both cases and a good agreement between the two solutions is obtained. Figure 4.21 (b) shows a comparison of the streamlines for the Laplace Equation numerical solution and the velocity flow vectors for the HYDROTHERM simulation once it had reached steady state. Both solutions show commensurate direction and magnitude of the flow.

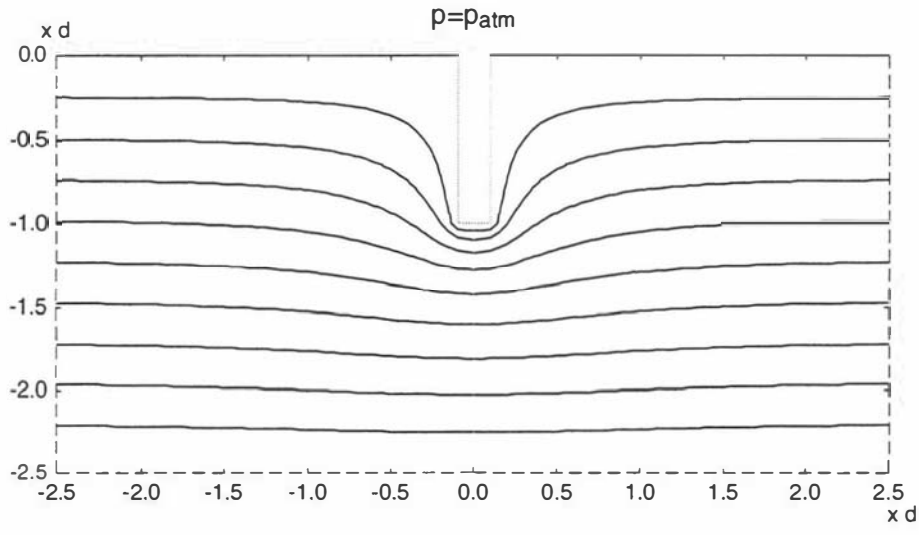

(a) Cross-section of isobaric surfaces

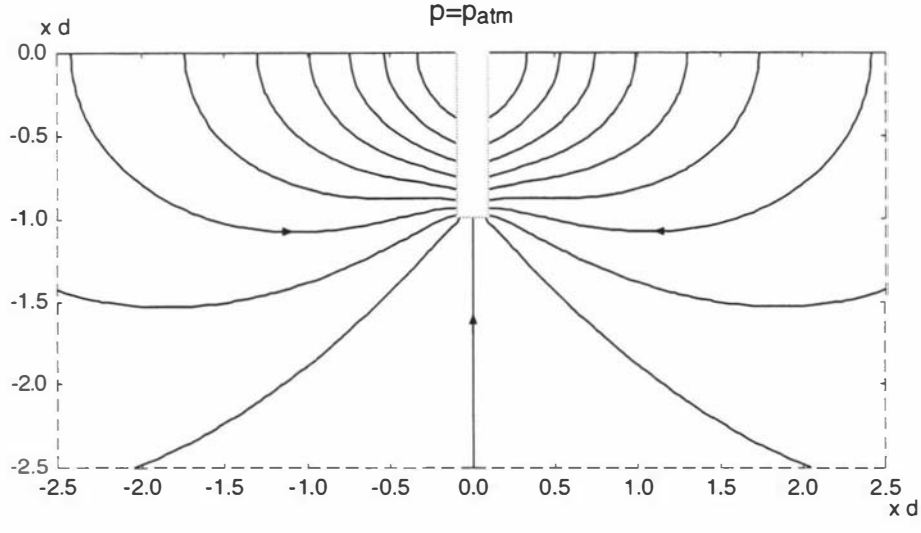

(b) Cross-section of stream surfaces

Figure 4.20: Isolines for pressure and stream-function for cylindrical hole (radius $a = 0.1d$, depth d) calculated on the simulation field $0 \leq r \leq 10d$, $-10d \leq z \leq 0$. The region out to $r = 2.5d$, $z = -2.5d$ is depicted.

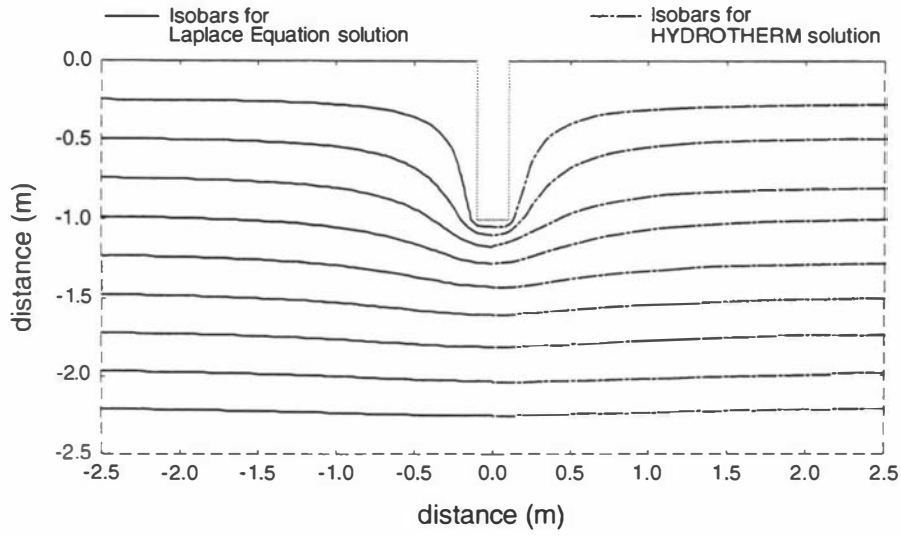

(a) Cross-section of isobaric surfaces

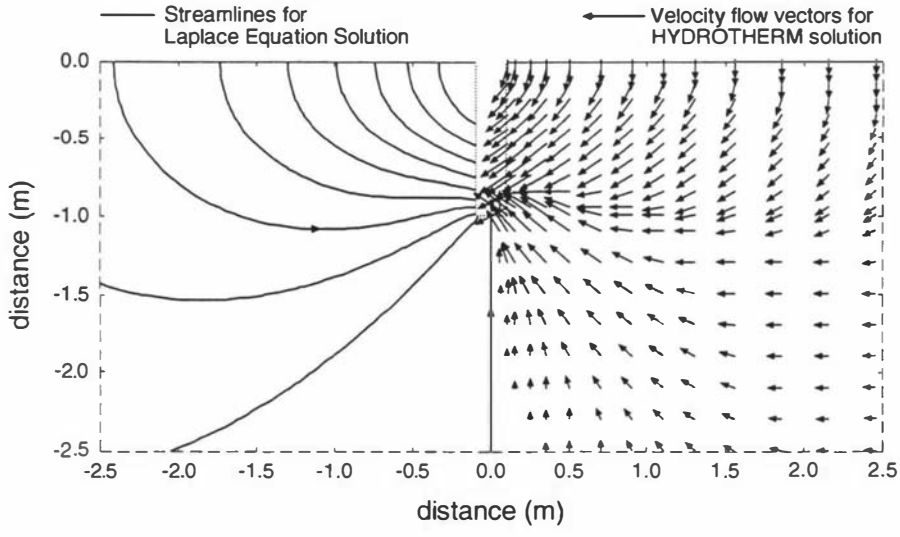

(b) Cross-section of stream surfaces and velocity flow vectors

Figure 4.21: A comparison of results found by our numerical Laplace Equation solution and a HYDROTHERM simulation for the case of a cylindrical hole (radius $a = 0.1\ m$, depth $d = 1\ m$) dug from a porous medium filled with liquid water. Results were calculated on the simulation field $0 \leq r \leq 10\ m$, $-10 \leq z \leq 0\ m$. The region out to $r = 2.5\ m$, $z = -2.5\ m$ is depicted. Results shown for the HYDROTHERM simulation are those obtained after the simulation had reached a steady-state. (See text for details.)

4.5 Summary

The conservation equations were set out in Chapter 3 for the description of ground fluid flow in hydrothermal eruptions in order to investigate suitable methods for solution in the general case. In this chapter, simple two-dimensional isothermal flows have been studied. Analytic solutions, where possible, have been compared with numerical solutions for steady flows.

In each of the three cases studied, the main pressure reduction was found to be local. As this pressure lowering will have a significant effect on flashing in a hydrothermal eruption, we would expect hydrothermal eruption fluid to originate locally.

In the cases of the semi-circular horizontal trench and the hemi-spherical hole, it was determined that over short periods of time, the majority of flow arriving at the trench originated in the ground. Over time, however, the ground continued to be flushed by water from the surface. The time scales over which this happens are dependent on the properties of the porous medium, the depth of the trench or hole, and the temperature of the fluid. While in a hydrothermal eruption full steady-state flow will not be established and we would expect the sources of the flow to be local, the description of the flow in these two cases may give some insight into how the ground flow will "recover" after an eruption. The replenishment of the depleted zone is likely to be from near-surface groundwater and not from depth. This will have a cooling effect on the region and may explain long recovery times before subsequent eruptions.

The pressure, potential and stream functions for the semi-circular horizontal trench and hemi-spherical hole cases were found both analytically and numerically. In both cases the analytic and numerical solutions found were equivalent. The streamlines in each case were found using the numerical method described in Section 4.2.2. This straightforward method, which effectively plots lines which are everywhere perpendicular to the equipotential lines, may also eventually prove useful in solving the steady non-isothermal case. Once the conservation equations have been solved for either h_f or $\mathbf{Q}_m$, the orthogonality of ∇h_f and $\mathbf{Q}_m$ may be used to complete the solution.

In the cylindrical case, results found numerically were compared to those found with the use of the groundwater flow simulator HYDROTHERM (Hayba and Ingebritsen 1994). A good agreement in the overall picture of the flow was obtained. The use of HYDROTHERM [or other simulators such as TOUGH2 (Pruess 1991)] may eventually prove useful in simulating aspects of the non-isothermal flow case.

CHAPTER 5

Transient Boiling Processes in Horizontal Flows

5.1 Introduction

The development of mathematical models for hydrothermal eruptions depends crucially on understanding transient boiling processes in porous media. In an effort to improve current understanding in this area, numerical experiments, physical experiments, and computer simulations have been carried out which investigate the progression of boiling fronts through porous media. In the experiments described in this chapter, the general problem being considered is as follows: a one-dimensional horizontal core is assumed to be initially saturated with liquid water and at some constant pressure throughout. If, as in the case of the hydrothermal eruption, the pressure is then reduced at one end of the porous medium, the pressure reduction will cause boiling to occur and flow to commence. A boiling front will be initiated at the end of the core and will quickly progress through

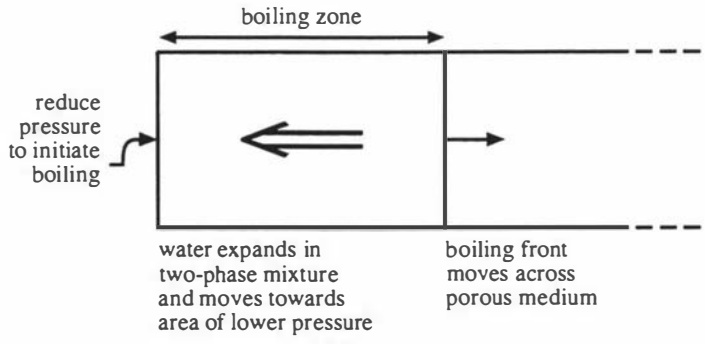

Figure 5.1: Schematic of boiling front propagation in a porous medium.

the porous medium. (See Figure 5.1.)

5.2 Numerical experiment

A numerical solution to the problem presented in Section 5.1 may be found by solving the (suitably simplified) equations of motion given in Chapter 3. The core in this numerical experiment is assumed to be semi-infinite in length and the fluid is assumed to be initially liquid at saturated (boiling) conditions. Both the homogeneous mixture (HM) and separable phase (SP) flow cases described in Chapter 3 are considered.

In one horizontal dimension, the conservation of mass and energy equations, Equations 3.1 and 3.2, for both the HM and SP flow cases can be written respectively as follows

$$\frac{\partial A_m}{\partial t} = -\frac{\partial \mathbf{Q}_m}{\partial x} \tag{5.1}$$

$$\frac{\partial A_e}{\partial t} = -\frac{\partial \mathbf{Q}_e}{\partial x} \tag{5.2}$$

The time t is taken to be zero at the moment the end of the core is depressurized and the positive horizontal distance x is measured from this end of the core.

5.2.1 Homogeneous mixture (HM) flow model

In the case of the homogeneous mixture model, from Equations 3.7 - 3.10, and 3.12 we have

$$A_m = \phi\rho_f \tag{5.3}$$

$$A_e = (1-\phi)\rho_r c_r T_{sat} + \phi\rho_f u_f \tag{5.4}$$

$$\mathbf{Q}_m = k\frac{\rho_f}{\mu_f}\left(-\frac{\partial p}{\partial x}\right) \tag{5.5}$$

$$\mathbf{Q}_e = h_f \mathbf{Q}_m + K\left(-\frac{\partial T_{sat}}{\partial x}\right) \tag{5.6}$$

where the density, specific enthalpy, internal energy, and dynamic viscosity of the two-phase fluid mixture are given by Equations 3.3 - 3.6.

The expressions 5.3 - 5.6 and 3.3 - 3.6 are substituted into the conservation of mass and energy equations, Equations 5.1 and 5.2, to give:

$$A_1 p_t + B_1 S_t = C_1 p_x S_x + D_1 p_x^2 + E_1 p_{xx} \tag{5.7}$$

$$A_2 p_t + B_2 S_t = C_2 p_x S_x + D_2 p_x^2 + E_2 p_{xx} \tag{5.8}$$

where the subscripts x and t are used to represent the partial derivatives with respect to x and t respectively and the coefficients A_1, A_2, B_1, B_2, C_1, C_2, D_1, D_2, E_1, and E_2 are (non-linear) functions of pressure and saturation. (For clarity, the functions for the coefficients A_1, A_2, B_1, B_2, C_1, C_2, D_1, D_2, E_1, and E_2 as well as the derivation of Equations 5.7 and 5.8 are not shown here, but are instead given in Appendix A.)

Equations 5.7 and 5.8 may then be reduced to a simpler set of ordinary differential equations by use of the similarity variable $\eta = x/\sqrt{t}$.

$$-\frac{1}{2}\eta A_1 p' - \frac{1}{2}\eta B_1 S' = C_1 p' S' + D_1 (p')^2 + E_1 p'' \tag{5.9}$$

$$-\frac{1}{2}\eta A_2 p' - \frac{1}{2}\eta B_2 S' = C_2 p' S' + D_2 (p')^2 + E_2 p'' \tag{5.10}$$

Here the superscripts $'$ and $''$ are used to represent the first and second derivatives with respect to η.

By eliminating p'' from Equations 5.9 and 5.10, an equation for S' as a function of p, p', and S is obtained. Similarly, eliminating S' from Equations 5.9 and 5.10 gives an equation for p'' as a function of p, p', and S.

$$p' = p'(p, p', S) \tag{5.11}$$

$$S' = S'(p, p', S) = \frac{\left[-\frac{1}{2}\eta (A_1 E_2 - A_2 E_1) - (D_1 E_2 - D_2 E_1) p'\right] p'}{\frac{1}{2}\eta (B_1 E_2 - B_2 E_1) + (C_1 E_2 - C_2 E_1) p'} \tag{5.12}$$

$$(p')' = p''(p, p', S) \tag{5.13}$$

$$= \frac{\left[\left(\frac{1}{2}\eta B_1 + C_1 p'\right)\left(\frac{1}{2}\eta A_2 + D_2 p'\right) - \left(\frac{1}{2}\eta B_2 + C_2 p'\right)\left(\frac{1}{2}\eta A_1 + D_1 p'\right)\right] p'}{\frac{1}{2}\eta (B_2 E_1 - B_1 E_2) + (C_2 E_1 - C_1 E_2) p'}$$

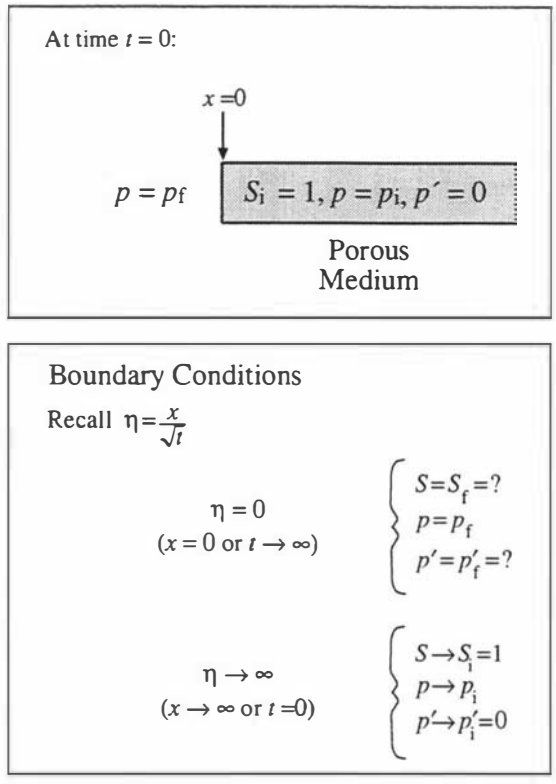

Figure 5.2: Boundary conditions for the one-dimensional horizontal flow problem described in Section 5.2. (See text for details.)

The core is assumed to be initially saturated with liquid water and at some pressure $p = p_i$. At time $t = 0$, the pressure at $x = 0$ is reduced to $p = p_f$. Therefore, at $t = 0$ or as x tends to infinity (both equivalent to η tending to infinity), we have $S = 1$, $p = p_i$, and $p' = 0$. At $x = 0$ or as t tends to infinity (equivalent to $\eta = 0$), $S = S_f$, $p = p_f$, and $p' = p'_f$. (See Figure 5.2.) S_f and p'_f are unknown, but may be found using the shooting method.

As stated previously, the fluid is at saturated (boiling) conditions. The temperature and pressure ranges of interest are small. Solutions to the problem in the saturated pressure range $1 \leq p \leq 5$ *bar* ($99.6° \leq T_{sat}(p) \leq 150°C$) are of interest for modelling hydrothermal eruptions, while solutions in the saturated pressure range $0.006112 \leq p \leq 0.1233$ *bar* ($0°C \leq T_{sat}(p) \leq 50°C$) are of interest for comparison with the physical experiment described later in Section 5.3. A set of simple functions describing the thermodynamic properties of water needed for solution to this problem over the temperature and saturated pressure ranges of interest were determined. These functions

are given in Appendix B.

Under the boundary conditions given in Figure 5.2, and using the coefficients given in Appendix A and the correlations and formulae for thermodynamic properties given in Appendix B, Equations 5.11 - 5.13 can be solved numerically to obtain liquid saturation and pressure distributions along the porous medium sample. Results shown in Section 5.2.3 were obtained using fourth order Runge-Kutta methods. Liquid saturation and pressure distributions found provide a description of the progression of the boiling front as it moves through the porous medium.

5.2.2 Separable phase (SP) flow model

In the case of separable phase flow, a two-phase Darcy Law is used in determining the mass flow rate per unit area. From Equations 3.13 - 3.18, the fluid mass and energy per unit volume of formation and mass and energy fluxes per unit area are given by

$$A_m = \phi[S\rho_l + (1-S)\rho_v] \tag{5.14}$$

$$A_e = (1-\phi)\rho_r c_r T_{sat} + \phi[S\rho_l u_l + (1-S)\rho_v u_v] \tag{5.15}$$

$$\mathbf{Q}_m = k\left(k_{rl}\frac{\rho_l}{\mu_l} + k_{rv}\frac{\rho_v}{\mu_v}\right)\left(-\frac{\partial p}{\partial x}\right) \tag{5.16}$$

$$\mathbf{Q}_e = k\left(k_{rl}h_l\frac{\rho_l}{\mu_l} + k_{rv}h_v\frac{\rho_v}{\mu_v}\right)\left(-\frac{\partial p}{\partial x}\right) + K\left(-\frac{\partial T_{sat}}{\partial x}\right) \tag{5.17}$$

In a manner similar to that used for solution of the HM flow case, the conservation of mass and energy equations given in 5.1 and 5.2 can be combined with Equations 5.14 - 5.17 and re-written in the form of Equations 5.7 and 5.8. The coefficients A_1, A_2, B_1, B_2, C_1, C_2, D_1, D_2, E_1, and E_2, while different from those found for the homogeneous mixture case, are again (non-linear) functions of pressure and saturation. (The functions for A_1, A_2, B_1, B_2, C_1, C_2, D_1, D_2, E_1, and E_2 as well as the derivation of Equations 5.7 and 5.8 for this separable phase flow case are given in Appendix A.)

The similarity variable η is again used to write the conservation of mass and energy equations in the form of 5.9 and 5.10 and these equations are then solved numerically (using fourth order Runge-Kutta methods) under the same boundary conditions as in the HM flow case. (See Figure 5.2.) As for the HM case, a set of simple functions describing the thermodynamic properties of water needed for solution to this problem over the temperature and pressure ranges of interest was determined. These functions

are given in Appendix B. Linear functions (the so-called X-curves) were used to describe the relative permeabilities k_{rl} and k_{rv}. These functions are also given in Appendix B.

5.2.3 Comparison of HM and SP models

A comparison of calculated solutions for the homogeneous mixture flow model with those for the separable phase flow model shows that for a given pressure reduction at one end of a porous medium sample, more liquid water is predicted to be converted to gas in the HM case than in the SP case. It is also predicted that the boiling front progresses at a faster rate in the SP case than in the HM case. This is illustrated in the following example: Consider a porous medium sample with $\phi = 0.1$, $k = 1 \times 10^{-10}\ m^2$, $K = 2\ Wm^{-1}K^{-1}$, $\rho_r = 2650\ kg\ m^{-3}$, and $c_r = 1000\ Jkg^{-1}K^{-1}$. The sample is assumed to be initially saturated with liquid water, at a pressure $p_{\mathrm{i}} > 1\ bar$ and a temperature $T_{\mathrm{i}} = T_{sat}\left(p_{\mathrm{i}}\right)$, before the pressure at one end of the core is reduced to 1 bar and the temperature reduced to T_{sat} (1 bar) = 99.6°C. Figure 5.3 shows the final liquid saturations obtained for a range of initial pressures ($1 \leq p_{\mathrm{i}} \leq 4.5\ bar$) in both the HM and SP flow cases. For each of the initial pressures investigated, the final liquid saturations are greater for the SP case than for the HM model. In the solution for a given initial pressure p_{i}, let η_{i} be the value of η for which $S = 0.99$ ($p \approx p_{\mathrm{i}}$, $p' \approx 0$). While the boundary conditions for the problem are placed on η as $\eta \to \infty$, η_{i} is the value of the similarity variable for which the initial conditions have "approximately" been met. Recall, $\eta = x/\sqrt{t}$. Therefore, for a given time t, the distance through which the boiling front has progressed is given "approximately" by $x = \eta_{\mathrm{i}}\sqrt{t}$. Similarly, the time it would take for the boiling front to progress through a given distance x is given "approximately" by $t = \left(x/\eta_{\mathrm{i}}\right)^2$. Figure 5.4 shows, over a range of initial pressures, the "rate" η_{i} at which the boiling front progresses through the porous medium for both the HM and SP cases. This "rate" is always larger in the SP case than in the HM case. Let $HM\eta_{\mathrm{i}}$ be the value of η_{i} for the HM flow case and $SP\eta_{\mathrm{i}}$ be the value of η_{i} for the SP flow case. Then, the greater the difference is between the initial pressure, p_{i}, in the core and the final pressure, p_{f}, to which one end is depressurized, the larger (and closer to 1) is the ratio $HM\eta_{\mathrm{i}}/SP\eta_{\mathrm{i}}$, and, therefore, the closer (proportionally) the "rates" at which the boiling fronts progress for the two flow cases.

A more detailed picture of the progression of the boiling front through the core is obtained by looking at the liquid saturation and pressure distributions in a particular case. Suppose the porous medium sample described in the previous example is initially at a pressure $p_{\mathrm{i}} = 1.2\ bar$ and temperature $T_{\mathrm{i}} = T_{sat}(p_{\mathrm{i}}) = 104.8°C$ before the pressure at one end of the sample is suddenly reduced to $p_{\mathrm{f}} = 1\ bar$ and the temperature reduced to $T_{\mathrm{f}} = T_{sat}\left(p_{\mathrm{f}}\right) = 99.6°C$. Calculated saturation and pressure distributions for the two

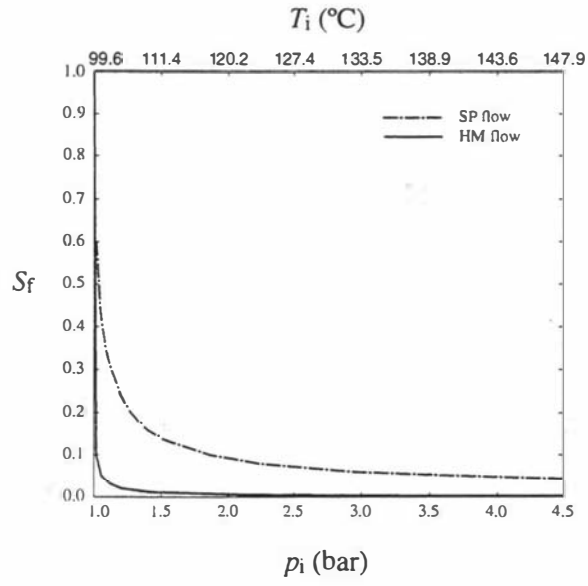

Figure 5.3: A core ($k = 1\times10^{-10}\ m^2$, $\phi = 0.1$, $K = 2\ Wm^{-1}K^{-1}$, $\rho_r = 2650\ kg\,m^{-3}$, $c_r = 1000\ Jkg^{-1}K^{-1}$), initially at a pressure p_i, and temperature $T_{sat}\,(p_i)$, is depressurized to 1 bar and the temperature reduced to $99.6°C$ at one end. The final liquid saturations, S_f, are shown for both HM and SP flows over a range of initial pressures p_i.

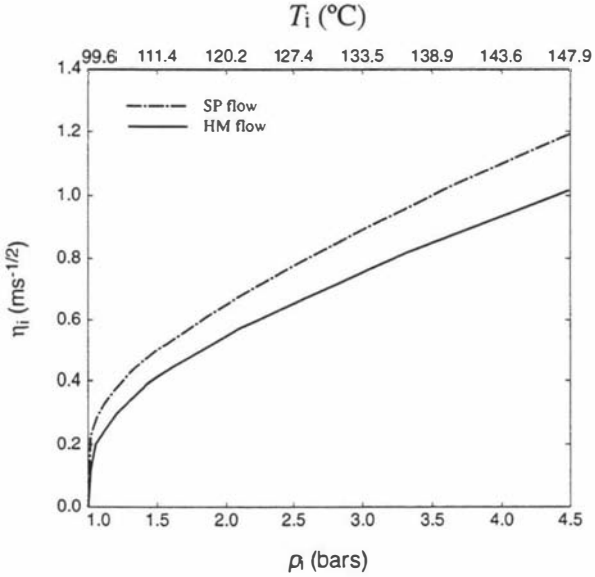

Figure 5.4: A core ($k = 1\times10^{-10}\ m^2$, $\phi = 0.1$, $K = 2\ Wm^{-1}K^{-1}$, $\rho_r = 2650\ kg\,m^{-3}$, $c_r = 1000\ Jkg^{-1}K^{-1}$), initially at a pressure p_i, and temperature $T_{sat}\,(p_i)$, is depressurized to 1 bar and the temperature reduced to $99.6°C$ at one end. The "rate", η_i, of the progression of the boiling zone is shown for both HM and SP flows over a range of initial pressures p_i. (See text for details.)

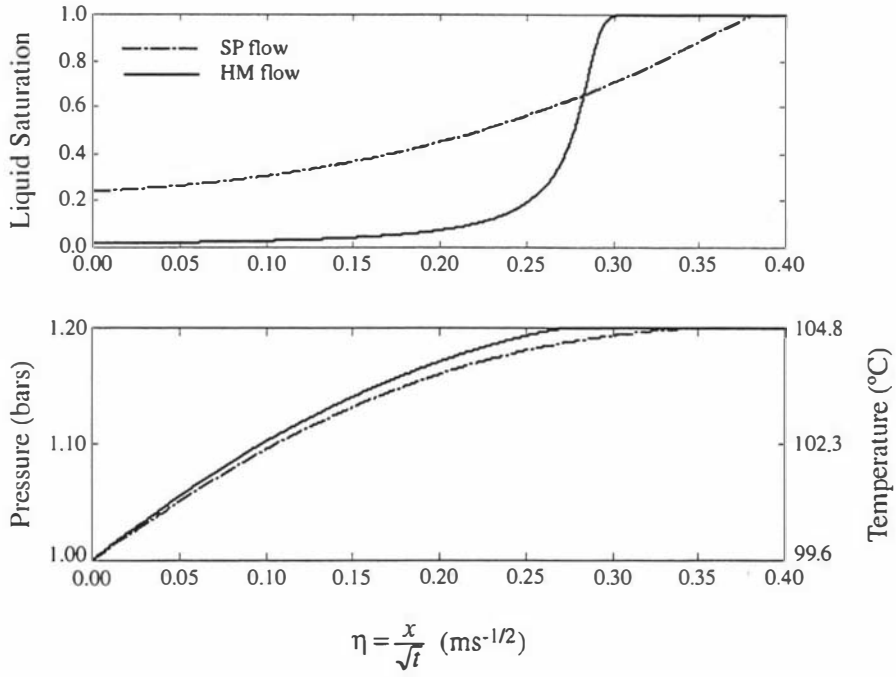

Figure 5.5: A porous medium sample ($k = 1 \times 10^{-10}\ m^2$, $\phi = 0.1$, $K = 2\ Wm^{-1}K^{-1}$, $\rho_r = 2650\ kg\ m^{-3}$, $c_r = 1000\ Jkg^{-1}K^{-1}$) is initially saturated with liquid water, at a pressure of 1.2 bar, and a temperature of T_{sat} (1 bar) = 104.8°C when the pressure at one end of the sample is reduced to 1 bar. Saturation and pressure distributions are shown for both HM and SP flow.

flow cases are shown versus η in Figure 5.5. In the HM case just over 98% of the liquid water in the core is converted to water vapour to give $S_f = 0.0185$. In the SP case only 76% is converted ($S_f = 0.24$). The saturation and pressure distributions versus η can be scaled appropriately to obtain plots versus time and in Figure 5.6 the saturation distributions are shown 1 second, 1 minute and 1 hour after the depressurization of one end of the core. The "rate", η_i, at which the boiling front progresses in the HM flow case is $HM\eta_i = 0.2982ms^{-1/2}$ and in the SP flow case is $SP\eta_i = 0.3784ms^{-1/2}$. Using the value of η_i for each of the two cases, it can be shown that in the HM case it would take about 11 seconds for the boiling front to progress through 1 m of the core, while in the SP case it would take about 7 seconds to travel this same distance. This specific case again illustrates the point that the boiling front progresses faster in the SP case than in the HM case and that more fluid boils in the HM case than in the SP case. It also shows that, over most of the region through which the boiling front has already progressed, more boiling has occurred in the HM case than in the SP case. (See Figures 5.5 and 5.6.)

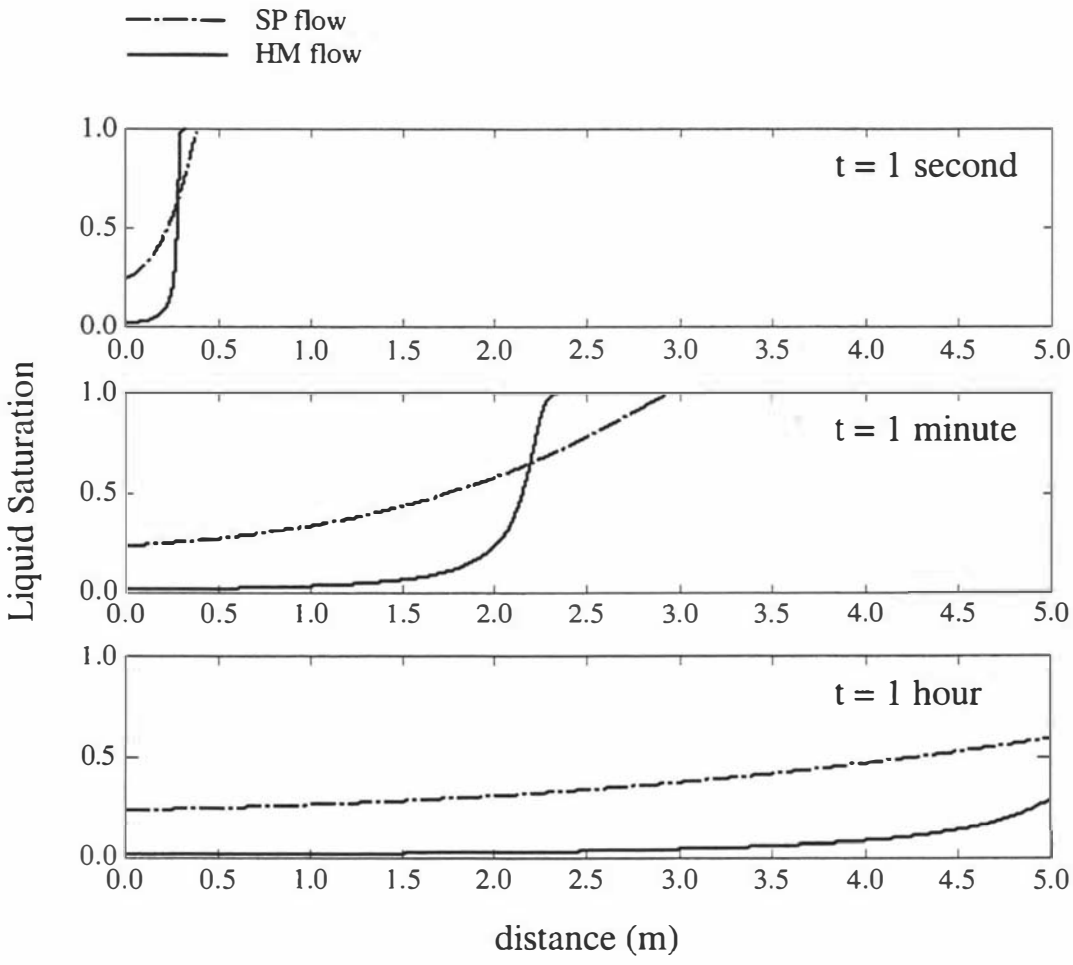

Figure 5.6: A porous medium sample ($k = 1 \times 10^{-10}\ m^2$, $\phi = 0.1$, $K = 2\ Wm^{-1}K^{-1}$, $\rho_r = 2650\ kg\ m^{-3}$, $c_r = 1000\ Jkg^{-1}K^{-1}$) is initially saturated with liquid water, at a pressure of 1.2 bar, and a temperature of T_{sat} (1 bar) = 104.8°C when the pressure at one end of the sample is reduced to 1 bar. Saturation distributions are shown for both HM and SP flow 1 second, 1 minute, and 1 hour after depressurization of the one end.

The specific volume fluxes (or Darcy velocities) of the fluid mixture, liquid phase, and vapour phase for each of the two flow cases are given as follows. From Equation 3.10 the specific volume flux for the fluid mixture, v_f, in the one horizontal dimension HM flow case is given by

$$v_f = \frac{k}{\mu_f}\left(-\frac{dp}{dx}\right) \tag{5.18}$$

where μ_f is given by Equation 3.6 and $\frac{dp}{dx} = \frac{1}{\sqrt{t}}\frac{\partial p}{\partial \eta}$. The specific volume flux of the liquid phase, v_l, and vapour phase, v_v, for the HM flow case are then given by

$$v_l = S v_f \tag{5.19}$$

$$v_v = (1-S)\, v_f \tag{5.20}$$

For the SP flow case the specific volume flux of the fluid mixture is given by

$$v_f = v_l + v_v \tag{5.21}$$

where the specific volume fluxes of the liquid and vapour phases are given separately by

$$v_l = \frac{k k_{rl}}{\mu_l}\left(-\frac{dp}{dx}\right) \tag{5.22}$$

$$v_v = \frac{k k_{rv}}{\mu_v}\left(-\frac{dp}{dx}\right) \tag{5.23}$$

Again, $\frac{dp}{dx} = \frac{1}{\sqrt{t}}\frac{\partial p}{\partial \eta}$.

In each of the two flow cases, pore-averaged velocities may be defined for the fluid mixture, u_f, liquid phase, u_l, and vapour phase, u_v, to be the average of the velocities of the "fluid" (fluid mixture, liquid phase and vapour phase) taken over the pore space. These pore-averaged velocities are given by

$$u_i = \frac{v_i}{\phi} \quad i = f, l, v \tag{5.24}$$

Using this definition, the pore-averaged velocity and particle velocity of the fluid mixture are the same.

The areal fractions of the pore space available for the flow of the liquid phase and vapour phase are S and $1-S$ respectively. Phase-averaged velocities for the liquid phase, w_l, and vapour phase, w_v, are then given by

$$\mathrm{w}_l = \frac{\mathrm{u}_l}{S} \tag{5.25}$$

$$\mathrm{w}_v = \frac{\mathrm{u}_v}{(1-S)} \tag{5.26}$$

For the liquid and vapour phases, these phase-averaged velocities are the particle velocities. [Note: For the HM flow case, by Equations 5.24, 5.19, 5.25, 5.20, and 5.26, the particle velocities of the fluid mixture, liquid phase, and vapour phase are therefore the same ($\mathrm{u}_f = \mathrm{w}_l = \mathrm{w}_v$) as required by the nature of the fluid mixture being a homogeneous mixture.]

For the specific case discussed in this section and illustrated in Figure 5.5, the pore-averaged velocity of the fluid mixture and the phase-averaged velocities for the liquid and vapour phases for each of the two flow cases are shown in Figure 5.7 for the time $t = 1$ second. The results show that for HM flow, the pore-averaged velocity of the fluid mixture is the same as the phase-averaged velocities of the liquid and vapour (as defined). In each flow case, the pore-averaged velocity of the fluid mixture is similar, although the fluid mixture is moving slightly faster and over a slightly greater distance in the SP flow model. Recall that the justification given in Chapter 3 for investigation into the HM flow model was an assumption that (in hydrothermal eruptions) the fluid mixture is moving so quickly that separable two-phase flow does not have time to develop. It is interesting to note then that the predictions of this flow regime are (as shown in Figure 5.7) a slightly slower mixture flow and a slower progression of the boiling front than in SP flow. The phase-averaged velocities of each phase are very different for the two flow cases. The liquid phase moves much slower in the SP flow model than in the HM model, while the vapour moves at a greater speed in the SP case than in the HM case. This is due to the fact that in HM flow the vapour is "dragging" the liquid along with it while at the same time the liquid is "holding" the vapour back due to the fact that the two-phases must move at the same phase-averaged (or particle) velocities.

The effect that thermal conductivity, permeability, and porosity have on the similarity solution has been investigated. When thermal conductivity is neglected, Equations 5.7

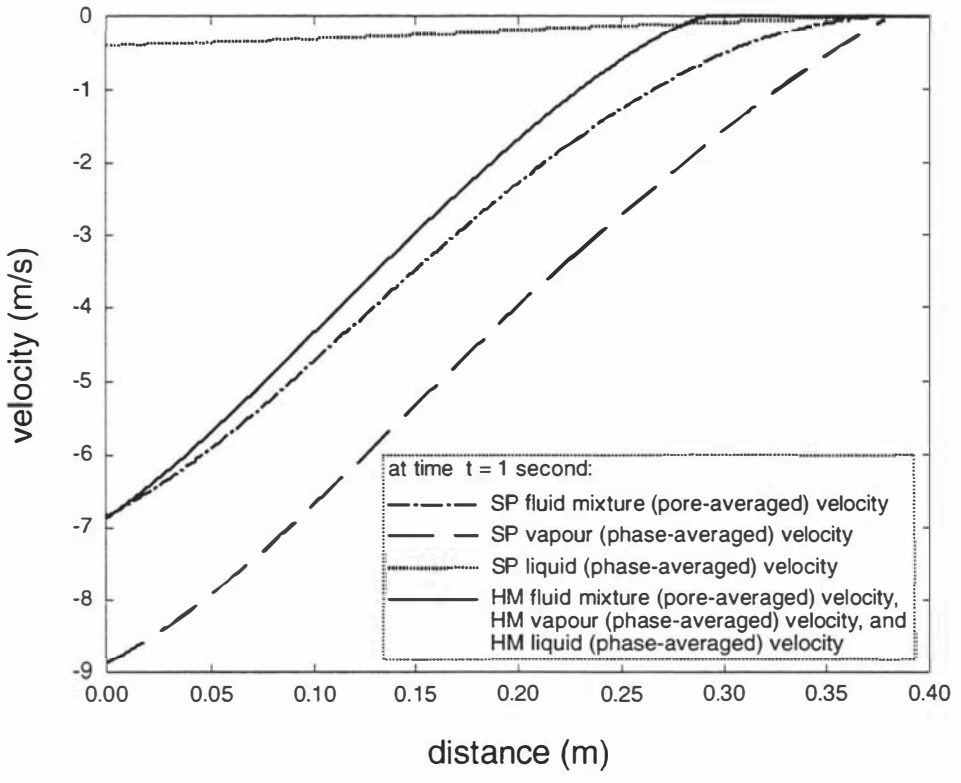

Figure 5.7: A porous medium sample ($k = 1 \times 10^{-10}\ m^2$, $\phi = 0.1$, $K = 2\ Wm^{-1}K^{-1}$, $\rho_r = 2650\ kg\ m^{-3}$, $c_r = 1000\ Jkg^{-1}K^{-1}$) is initially saturated with liquid water, at a pressure of 1.2 bar, and a temperature of T_{sat} (1 bar) = 104.8°C when the pressure at one end of the sample is reduced to 1 bar. The pore-averaged velocity of the fluid mixture and the phase-averaged velocities of the liquid and vapour phases are shown for both HM and SP flow one second after depressurizing the end of the core.

and 5.8 can again be written in the form of Equations 5.9 and 5.10, using (in this special case) the similarity variable $\eta = \sqrt{k} \cdot x/\sqrt{t}$. When k occurs in the similarity variable in this way, k does not appear in the coefficients C_i, D_i, and E_i for $i = 1, 2$. The result of using this similarity variable for solution is that, for all other parameters (p_i, S_i, p_f, ϕ, ρ_r, c_r) remaining the same, altering k only alters the rate at which the boiling front progresses through the porous medium. That is, varying k has the effect of scaling the length of the boiling zone by $\sqrt{k}$. Investigation shows that the effects of thermal conductivity are negligible for permeabilities greater than or equal to approximately $1 \times 10^{-13}\ m^2$ (although small effects can be seen at $1 \times 10^{-13}\ m^2$). This is illustrated in the following example: Consider a porous medium sample with $K = 2\ Wm^{-1}K^{-1}$, $\phi = 0.1$, $\rho_r = 2650\ kg\ m^{-3}$, and $c_r = 1000\ Jkg^{-1}K^{-1}$. The sample is assumed to be initially saturated with liquid water, at a pressure p_i, and a temperature $T_{sat}\,(p_\mathrm{i})$ before the pressure at one end of the core is reduced to 1 bar and the temperature reduced to $T_{sat}\,(1\text{ bar}) = 99.6°\mathrm{C}$. A plot of p_i versus S_f over a range of values for p_i is given in Figure 5.8 for the SP flow case. For each initial pressure, p_i, investigated, the final liquid saturation obtained is the same for permeabilities $k \geq 1 \times 10^{-12}\ m^2$ and there is little difference in these final liquid saturations and those for $k = 1 \times 10^{-13}\ m^2$. However, for permeabilities of $k \leq 1 \times 10^{-14}\ m^2$, less boiling occurs and the final liquid saturations are higher. While the results shown in Figure 5.8 are for the SP flow case only, similar results are found for the HM case. In the HM case, however, the values of the final liquid saturation are very small regardless of k so the effects of thermal conductivity are less in the HM case than in the SP case. The effects of varying the porosity ϕ on the final liquid saturation are shown in Figure 5.9. For both HM flow and SP flow, the lower the porosity ϕ, the lower the final liquid saturation and hence the more boiling occurs. The effect of differing porosities is more dramatic in the SP flow case than for the HM flow case as, again, most of the water in the HM case boils regardless of ϕ.

As stated previously, the effects of thermal conductivity are negligible for permeabilities greater than $1 \times 10^{-13}\ m^2$. When thermal conductivity is neglected, a scaling factor of $\sqrt{k}$ is introduced in the parameter η. Therefore, returning to the example illustrated in Figure 5.5, if the permeability of the rock matrix investigated had been $k = 1 \times 10^{-12}\ m^2$ instead of $k = 1 \times 10^{-10}\ m^2$ the saturation and pressure distributions of the solution found would have been those shown in Figure 5.5 with the η-axis scaled by a factor of 1/10. The saturation distributions 1 second, 1 minute, and 1 hour after depressurization would have been those shown in Figure 5.6 with the x-axis scaled by 1/10. Similarly, if the permeability had been $k = 1 \times 10^{-8}\ m^2$, the saturation and pressure distributions for the solution found would have been those shown in Figure 5.5 with the η-axis scaled by a factor of 10.

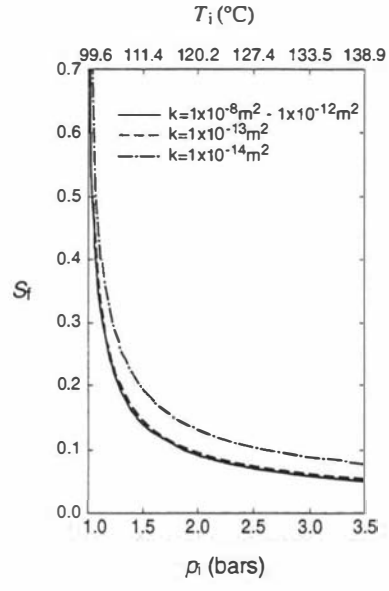

Figure 5.8: A porous medium sample ($\phi = 0.1$, $K = 2\ Wm^{-1}K^{-1}$, $\rho_r = 2650\ kg\ m^{-3}$, $c_r = 1000\ Jkg^{-1}K^{-1}$) is initially saturated with liquid water, at a pressure of p_{i}, and a temperature of $T_{sat}\ (p_{\mathrm{i}})$ when the pressure at one end of the sample is reduced to 1 bar and the temperature reduced to $99.6°C$. Final liquid saturations obtained for SP flow are shown for various permeabilities k over a range of initial pressures p_{i}.

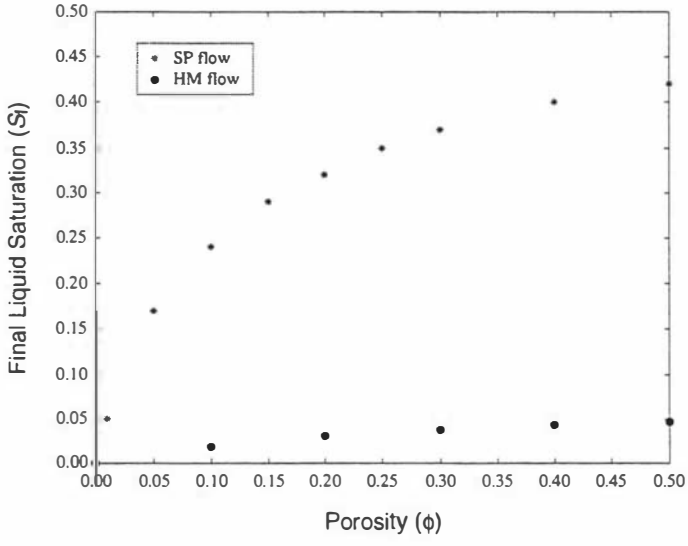

Figure 5.9: A porous medium sample ($k = 1 \times 10^{-10}\ m^2$, $K = 2\ Wm^{-1}K^{-1}$, $\rho_r = 2650\ kg\ m^{-3}$, $c_r = 1000\ Jkg^{-1}K^{-1}$) is initially saturated with liquid water, at a pressure of 1.2 bar, and a temperature of T_{sat} (1 bar) = 104.8°C when the pressure at one end of the sample is reduced to 1 bar and the temperature reduced to $99.6°C$. Final liquid saturations obtained for both HM and SP flows are shown over a range of porosities ϕ.

5.3 Physical experiment

A set of physical experiments on rapid transient boiling in porous media have been carried out with the intention of providing data to be used to test the validity or otherwise of the mathematical models described in Section 5.2. Results obtained allow a qualitative comparison only.

In the physical experiments, a porous medium sample is placed inside a containment vessel. The sample is then saturated with liquid water. A decrease in pressure at one end of the sample allows boiling to occur. A boiling front is initiated at the end of the vessel and quickly moves through the sample (see Figure 5.1). Nuclear Magnetic Resonance techniques are used to image the liquid water content throughout the sample over time, providing a picture of the progression of the boiling front as it moves through the core.

5.3.1 Apparatus and procedure

The experimental apparatus consists of a containment vessel, connection hose, ambient condition reservoir, Nuclear Magnetic Resonance (NMR) equipment and a vacuum pump (see Figure 5.10).

In the experiment, a cylindrical rock core was first sealed around its sides with heat shrink. Plastic caps fitted with O-rings were then placed on each end. One end of the core was sealed by its cap while the other end remained open to allow for the eventual flow of fluid from the rock to the ambient condition reservoir. (See Figure 5.10.) The core was initially saturated with de-ionized water and its dimensions, average porosity, permeability (from a permeameter experiment) and density were calculated. A cylindrical brass chamber, 3 litres in volume, was used to provide "ambient" conditions for the experiment. Most of the air was removed from the reservoir enabling the pressure within the reservoir to be controlled by the temperature. [An addition of a small amount of water into the reservoir would then provide an ambient pressure of $p_{air} + p_{sat}(T_{ambient})$.] The temperature of the reservoir was reduced to $T_{ambient}$, a temperature low enough to provide ambient pressure conditions which would initiate boiling in the core. A connecting hose of diameter 8 mm and length 2.5 m was filled with cold water and used to connect the ambient conditions reservoir to the core. The core was placed inside the NMR, the vacuum pump was turned off and the initial pressure p_{air} and temperature $T_{ambient}$ inside the reservoir were recorded. The experiment was initiated by opening the tap between the reservoir and the connecting hose. The cold water inside the hose boiled due to the pressure reduction and flowed into the ambient condition reservoir. The addition of this water to the reservoir provided the ambient pressure for the experiment of $p_{air} + p_{sat}(T_{ambient})$. Shortly after the opening of the tap, boiling was initiated at the

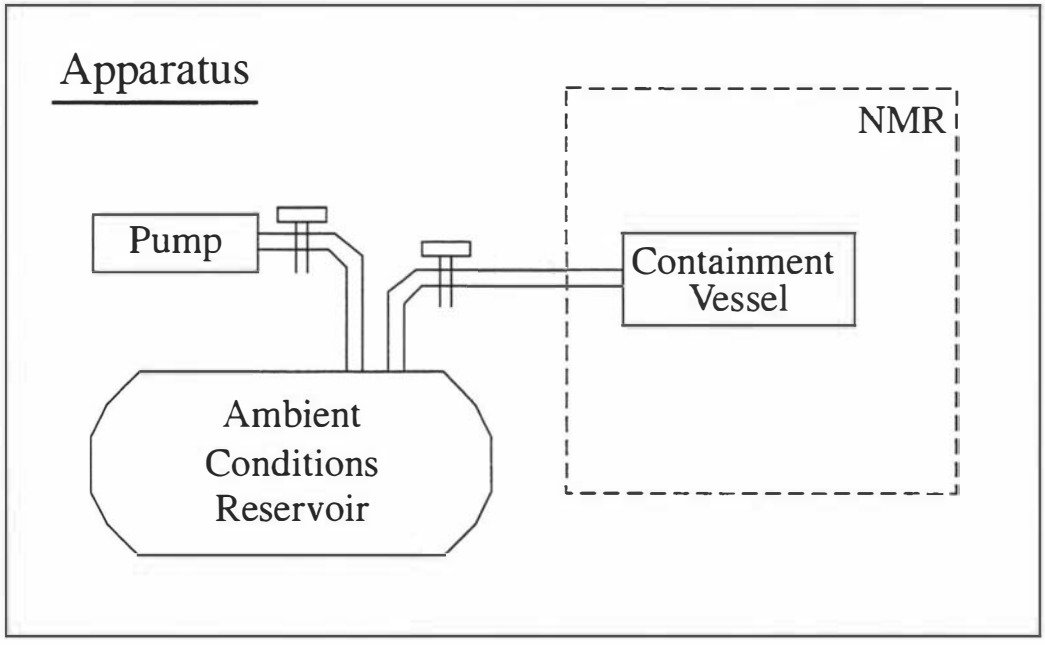

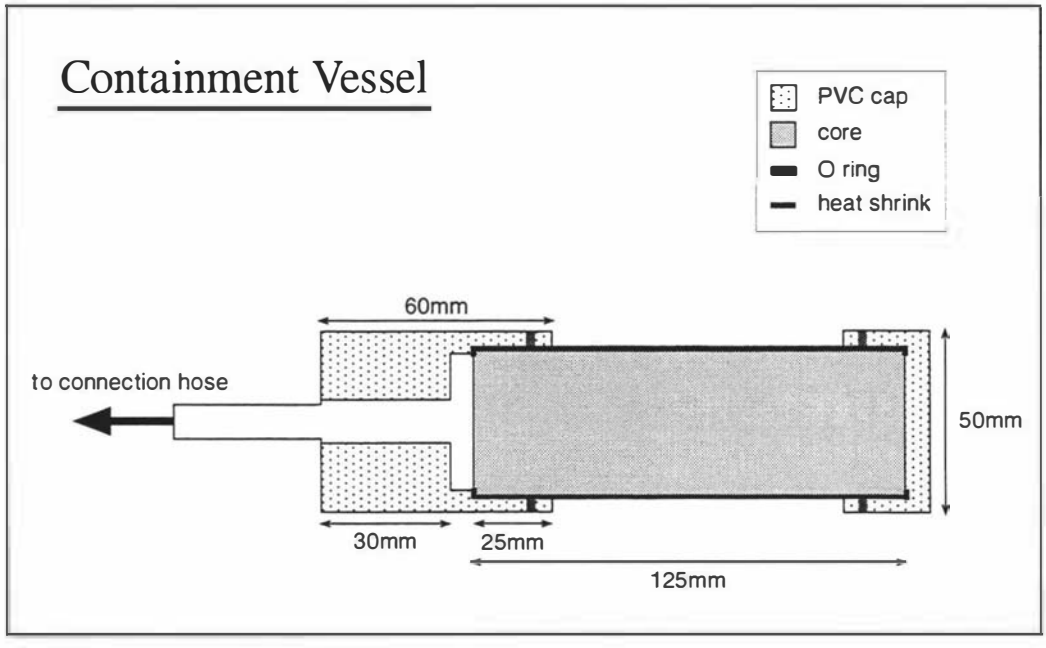

Figure 5.10: Experimental apparatus. (Not shown to scale.)

depressurized end of the core and the NMR equipment was used to measure the spatially distributed image of water concentration in the core.

5.3.2 Results

A number of laboratory experiments were performed using a bentheimer rock core of length 12.5 cm and diameter 3.8 cm. Approximate rock properties were: $\rho_r = 2000\ kg\,m^{-3}$, $\phi = 0.18$, $K = 2\ Wm^{-1}K^{-1}$, $c_r = 1000\ Jkg^{-1}$, and $k = 1 \times 10^{-12}\ m^2$. The initial temperature and pressure inside the ambient condition reservoir were $T_{ambient} = 2°C$ and $p_{air} = 5\ mbar$ providing an ambient pressure for the experiments of approximately $p_{air} + p_{sat}(T_{ambient}) = 12\ mbar$. The core was initially at atmospheric conditions (approximately 1 bar and $20°C$). Therefore, the initial pressure within the formation was greater than the saturated pressure. It was expected, however, that the pressure along the core would immediately lower to the saturated pressure following the depressurization of the open end. Using NMR imaging, one-dimensional liquid saturation distributions along the core were found. Some NMR images are reproduced in Section 5.3.2.2 with comments. Results of numerical experiments (found using the similarity variable solution method described in Section 5.2) are given in Section 5.3.2.1 for comparison with the physical experiment results in Section 5.3.2.2.

5.3.2.1 Numerical Results

Numerical experiments were performed on a rock core with the same rock properties as the core used in the physical experiment ($\rho_r = 2000\ kg\,m^{-3}$, $\phi = 0.18$, $K = 2\,Wm^{-1}K^{-1}$, $c_r = 1000\ Jkg^{-1}$, and $k = 1 \times 10^{-12}\ m^2$). In these numerical experiments it was assumed that the porous medium sample was initially at a temperature $20°C$ and pressure $p_{\mathrm{i}} = p_{sat}(20°C) = 2337\ Pa$ when one end of the core was depressurized to $p_{\mathrm{f}} = 1200\ Pa$ and the temperature at this end reduced to $10°C$. The "rate" at which the boiling front progressed through the core in both the HM and SP flow cases was given by $\eta_{\mathrm{i}} \approx 0.004$. Therefore, according to numerical results, it should take approximately 16 minutes for a boiling front to reach the end of the core opposite that which was depressurized. Numerical experiments predict the final liquid saturation to be $S_{\mathrm{f}} \approx 0.006$ for HM flow and $S_{\mathrm{f}} \approx 0.34$ for SP flow.

5.3.2.2 Physical Experiment Results

Experiment A: In this experiment saturation distributions were found every 200 milliseconds for 25 seconds. Two measured saturation distributions are shown in Figure 5.11.

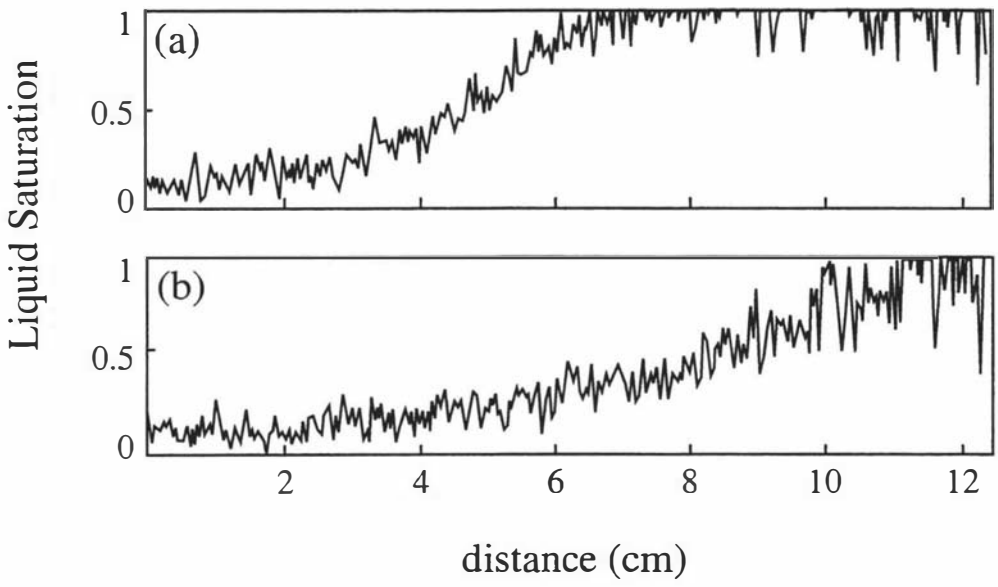

Figure 5.11: Experiment A. Two images of liquid saturation: image (a) was taken within 200 milliseconds of the onset of boiling, and image (b) a further 200 milliseconds later. (See text for details.)

We have assumed the core was initially saturated with liquid water. An image of liquid saturation was taken before boiling was initiated and subsequent images have been normalized with respect to this initial distribution. Consecutive images taken were separated by 200 milliseconds. The time at which the tap was turned and the experiment began is not recorded electronically. The first images taken show a fully saturated core. These images were followed by images in which boiling occurs. It is therefore assumed that in between the last fully saturated core image and the first image in which boiling occurs, the tap was turned and the experiment began. Hence, the image shown in Figure 5.11 (a) took place within 200 milliseconds of the onset of boiling and the image in Figure 5.11 (b) was taken a further 200 milliseconds later.

While data obtained shows a boiling front moving through the core as expected, the progression of the front occurs quickly and not enough information about the process is obtained. In less than 200 milliseconds [see Figure 5.11 (a)] boiling has apparently begun in the first 7 *cm* of the core, while in fewer than 400 milliseconds [see Figure 5.11 (b)] boiling is occurring throughout the core. According to the numerical results given in Section 5.3.2.1, this process should occur at a much slower rate. The final liquid saturation for this experiment is between $S_f = 0.1$ and $S_f = 0.2$. This is in between the final liquid saturations predicted by the numerical solutions for the HM flow case and that for the

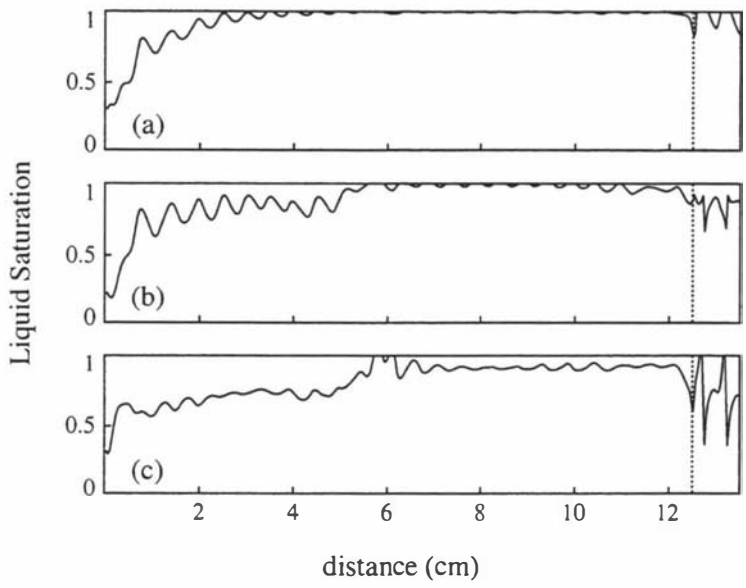

Figure 5.12: Experiment B. Three (normalized) images of liquid saturation: image (a) was taken within 0.5 seconds of initiation of boiling, image (b) 0.5 seconds later, and image (c) approximately 8 minutes later.

SP flow case.

(Note: After some discussion between the scientist operating the NMR equipment and her colleagues, it was determined that the NMR equipment may have been set to focus on volumes in the core which were too large. This may have had one of the following effects. It may have presented a picture of what was occurring in the large pores in the core only. If this was the case, results may suggest that boiling fronts progress through larger pores at a faster rate than they do through smaller ones. It may, however, be that the result of the NMR setting was to take inappropriate averages over areas which were too large. It was decided that adjustments would be made to the NMR setup and more experiments would be conducted.)

Experiment B: Saturation images in this experiment were found every half-second for 10 minutes. Three saturation distributions obtained are shown in Figure 5.12. Again, distributions have been normalized with respect to an initial scan.

Figure 5.12 (a) shows the initiation of a boiling front from the depressurized end. Boiling appears to also have begun at the closed end of the core even before the boiling front reaches this end. A small amount of water lies between the rock and the plastic cap which seals this closed end. It is this "end-water" which appears to begin to boil almost immediately (see portion of scan to the right of dotted line in Figure 5.12). In

Figure 5.12 (b) the progression of the boiling front can be seen as well as the continuation of boiling in the water at the end of the core. Over time, some boiling occurs throughout the core [see Figure 5.12 (c)].

Further observations (not shown here) indicate increases in saturation at some regions at later times. Such an increase may be due to recondensation of moving steam or to the flow of water back into the core. Upon removal of the core from the NMR, it was noted that the core felt cold to the touch. A qualitative deduction, then, is that the core was too cold for further boiling to take place under the conditions of the experiment.

The speed at which the boiling front moves through the core in Experiment B is closer to numerical estimates, but because the core is finite, the predictions of the semi-infinite model may not apply. The final liquid saturation for this experiment is between $S_f = 0.2$ and $S_f = 0.3$ which is closer to the numerical prediction of the SP flow case than that of HM flow.

5.4 Numerical simulations

Several simulations using HYDROTHERM (Hayba and Ingebritsen 1994) were carried out for comparison with both the finite core experiments and the SP flow similarity solutions. (Note: HYDROTHERM simulates separable phase groundwater flow only; it does not simulate two-phase homogeneous mixture flow.) Unfortunately pressures are constrained in HYDROTHERM to be no less than 0.5 *bar* so comparisons with the physical experiments are qualitative only.

Simulations were carried out on a one-dimensional core of length 14.5 *cm*, $\rho_r = 2000\ kg\ m^{-3}$, $\phi = 0.18$, $K = 2\ Wm^{-1}K^{-1}$, $c_r = 1000\ Jkg^{-1}$, and $k = 1 \times 10^{-12}\ m^2$. The core was assumed to be initially saturated with liquid water, at a pressure $p_i = 1.1\ bar$ and temperature $T_i = T_{sat}(p) = 102.3°C$. Constant temperature and pressure conditions of $p_f = 1\ bar$ and $T_f = T_{sat}(p) = 99.6°C$ were placed on the depressurized end.

When "no flux" boundary conditions were placed on the end opposite that which was depressurized, a boiling front was initiated at the depressurized end and progressed through the porous medium [see Figure 5.13 (a)]. As the system approached thermodynamic equilibrium, increases in liquid saturation were seen [see Figure 5.13 (b)]. Calculated velocities indicated that water was flowing back into the core replenishing the depleted zone. Such late time increases in liquid saturation indicate consistency in this aspect of the simulations and physical experiments. In the physical experiments this had a cooling effect on the region. In the event that such an effect were produced in hydrothermal eruptions, it would slow the eruption in progress, and any cooling effect on the area may explain long recovery times between subsequent eruptions.

When "end-water" was placed at the closed end of the porous medium, small-scale boiling was indicated almost immediately in this water (not shown). This boiling, however, occurred in very small quantities in the simulations, much smaller than the NMR profiles indicated.

Good agreement between the simulation and the (SP) similarity solution was obtained up to the time at which the boiling front had progressed completely through the core. Late-time saturation increases are a feature of the finiteness of the core and are therefore not predicted by the similarity solution. (Note: This agreement for early time periods is true for simulations in which a relatively small pressure reduction was made at one end of the short core. The effects of the boundary conditions which are placed on the end opposite depressurization can be seen even during early time periods for large pressure drops.)

When constant temperature and pressure boundary conditions were placed on the end opposite that which was depressurized, we again saw the progression of a boiling front through the porous medium [see Figure 5.14 (a)]. As this boiling front moved through the core, heat was removed from the system [see Figure 5.14 (d), $t < 20\ s$]. Once the boiling front had progressed completely through the porous medium, increases in liquid saturation were again seen, but water velocities indicate in this case these were due to water being fed from the end opposite that which was depressurized. A liquid-resaturation front moved back through the core until the system eventually reached a steady state [see Figure 5.14 (b)].

Good agreement between the simulation and the (SP) similarity solution was again obtained up to the time at which the boiling front had progressed completely through the core.

5.5 Summary

In this chapter, a report is given on numerical experiments, physical experiments and computer simulations which have been conducted to investigate some aspects of transient boiling processes in porous media.

In Section 5.2, a comparison of the progression of boiling fronts under the differing flow regimes of HM and SP fluid flows was made. A one-dimensional semi-infinite mathematical model was solved for both cases. As the HM flow model is based on the assumption that the rapidity of motion (in hydrothermal eruptions) does not allow for separable phase flow to develop, it is interesting to note that the predictions of this flow regime are slower fluid mixture flow and a slower progression of the boiling front than predicted by the SP flow model. A comparison of results for the two flow cases also

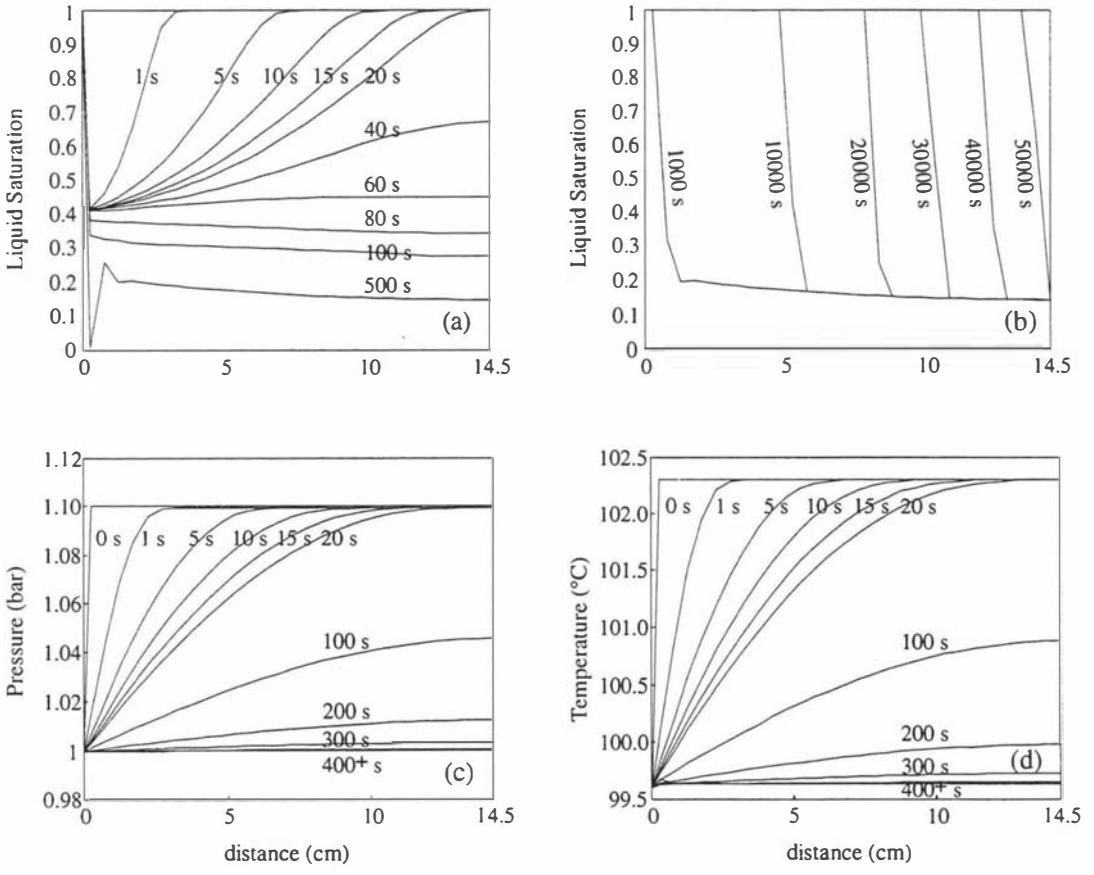

Figure 5.13: Saturation, pressure and temperature curves for one-dimensional core. Constant pressure and temperature conditions at $x = 0$ *cm*, "no flux" boundary conditions at $x = 14.5$ *cm*. (See text for details.)

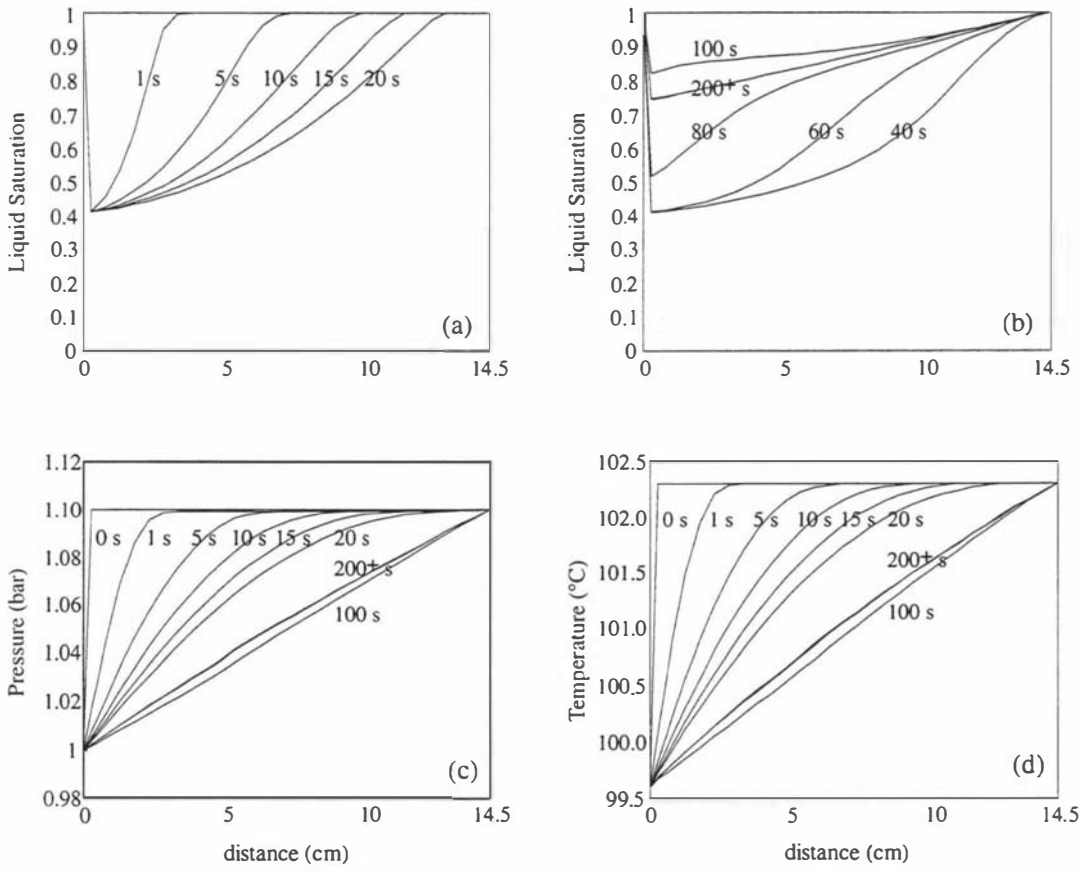

Figure 5.14: Saturation, pressure and temperature curves for one-dimensional core. Constant pressure and temperature conditions at both ends. (See text for details.)

shows, due to the fact that the liquid and vapour must move at the same speed in HM flow, the liquid phase moves considerably faster and the vapour phase slightly slower in the HM flow case. Perhaps the most significant difference in the two flow cases, however, is that considerably more fluid boils in the HM flow case, particularly for smaller pressure drops across the core.

For both models of fluid mixture flow, investigation shows that the effects of thermal conductivity are negligible for $k \geq 1 \times 10^{-13}\ m^2$. For cases in which the thermal conductivity is negligible, the result of varying the permeability k on the solution is to scale the length of the boiling zone at any given time by $\sqrt{k}$. Also, for both fluid mixture flow models, the larger the porosity of the porous medium, the less boiling which occurs and the higher the final liquid saturation in the core. This difference in final liquid saturations is greater in SP flow as most of the fluid in the HM case boils regardless of the porosity.

The results of the one-dimensional semi-infinite mathematical models were compared to results from physical experimental data. It was originally hoped that such a comparison would allow for some conclusions to be made on whether HM flow or SP flow was likely to occur during early time periods in hydrothermal eruptions. However, more investigation is needed before such conclusions can be made. Because physical experiments were constrained to be finite, direct comparison of all aspects of results was not possible. Both numerical and physical experiments show a boiling front initiated at one end of the porous medium. However, the rate at which the front progressed through the core and boiling effects at the closed end of the core may be features of the finiteness of the physical experiment which were not predicted by the semi-infinite model. Differences in numerical and physical experimental configurations need to be resolved in order to gain quantitative agreement. Suggestions for future improvements to experimental work are given in Chapter 6.

Numerical simulations using HYDROTHERM were conducted for comparison with both the physical experiment results and those from the SP similarity solution. Simulation calculations again show the progression of a boiling front through the porous medium. Some of the physical experiment effects due to the finiteness of the core (such as late time resaturation) which were not predicted by the semi-infinite similarity solution, were predicted by the computer simulations. Results of computer simulations and the SP similarity solution agree for "early" time periods, but the effects of the boundary conditions placed on the "closed" end of the finite core in the simulations do not allow for "late" time comparisons with the semi-infinite similarity solution.

CHAPTER 6

Summary, Conclusions and Suggestions for Future Work

6.1 Summary and Conclusions

Much of the mathematical modelling work which has been done to date on hydrothermal eruptions has focused on the underground flow processes which take place (McKibbin 1990, 1996; Bercich and McKibbin 1992). These investigations have focused on quasi-steady one-dimensional flow models in the vertical direction. The models of McKibbin (1990) and Bercich and McKibbin (1992) examined the motion of the boiling front and erosion surface under the assumption that the fluid was a two-phase water mixture in which the velocities of the liquid and vapour phases were the same (HM flow). The model of McKibbin (1996) studied the effects of non-condensable gases on the motion of the boiling front. The objective of this thesis has been to further the understanding of the underground flow and boiling processes involved in hydrothermal eruptions. The main contributions to this area are: a description of the recharge of a hydrothermal system following an eruption which is based on a study of steady isothermal flow, and an investigation of transient boiling processes in one horizontal dimension which includes a comparison of the predictions of homogeneous mixture (HM) and separable phase (SP) flows.

The definition of a hydrothermal eruption and its relation to / distinction from other phreatic eruptions was discussed in Chapter 1. Previous modelling experiences of specific eruptions (prehistoric and historic, natural and induced) were then summarized. In Chapter 2, a conceptual model of the hydrothermal eruption process was formed based on information gathered from these previous modelling experiences. This model describes an eruption initiated at the surface by a sudden pressure reduction. The pressure reduction

causes boiling to occur and a boiling front moves downward through the porous medium. Solid material is also ejected upward from the erosion surface. A discussion on events which may cause the pressure reduction necessary to initiate an eruption is given. Events which may cause instability in the hydrothermal system allowing future initiation events to trigger an eruption are also described. A laboratory model of a hydrothermal eruption has been constructed. Observations from this physical model provide visual observations consistent with those seen in naturally occurring hydrothermal eruptions. Qualitative results from this laboratory model support the conceptual model given in this work and confirm the effectiveness of the proposed triggering mechanism.

A mathematical model of the underground flow processes in hydrothermal eruptions was formed in Chapter 3 based on the conceptual model. The principles of conservation of mass, momentum and energy, are used to obtain a set of non-linear partial differential equations which regulate transient mass and energy transport. The fluid is modelled as a two-phase water mixture under two different fluid flow regimes: single homogeneous mixture (HM) flow and separable phase (SP) flow.

The solution to the mathematical problem outlined in Chapter 3 was presented in Chapter 4 under the simplifying assumption of steady isothermal flow. This is equivalent to investigating the problem of digging a hole for the purposes of extracting water. The resultant pressure reduction will cause flow to commence. The flow around and into the hole is quantified and the origin of the flowing water is determined for three geometrical configurations. In each case, results show pressure reduction to be a localized occurrence. As this pressure lowering has a direct effect on boiling in hydrothermal eruptions, the origin of hydrothermal eruption fluid may be deduced to be local. Calculations also show that, over time, the water within the formation is flushed by groundwater from the surface. The time frame over which this occurs is dependent on the properties of the porous medium, the temperature of the fluid, and the depth of the hole. The larger the porosity of the porous medium and the greater the depth of the hole, the slower this surface "recharge". The larger the permeability of the porous medium and the greater the temperature of the fluid the quicker the surface "recharge". While the flow in a hydrothermal eruption is not steady, and, as stated previously, is expected to originate locally, the far field flow of the isothermal case may show how ground flow will recover following an eruption. Cool groundwater continues to flood the depleted zone over time, cooling the affected region. This may explain long recovery times before subsequent eruptions.

In chapter 5 an investigation was made into the progression of boiling fronts in one horizontal dimension. Using the conservation equations outlined in Chapter 3, semi-infinite horizontal models for both the HM and SP flow regimes are described and solved

numerically. Results for both cases found thermal conductivity to be negligible for permeabilities of $k \geq 1 \times 10^{-13}\ m^2$. The present work also shows that the permeability of the porous medium has a great influence on the speed of the boiling front. For cases in which thermal conductivity is negligible, an increase in the permeability results in an increase (by a factor of $\sqrt{k}$) in the length of the boiling zone. The magnitude of the porosity of the porous medium also shows a marked effect on the amount of boiling which takes place, particularly for SP flow.

It has been noted above that previous mathematical models investigating underground flow processes in hydrothermal eruptions were based on the HM flow regime; that model was chosen because it was assumed that the fluid in a hydrothermal eruption flows so quickly that separable phase flow does not have time to develop. Numerical simulators, such as HYDROTHERM and TOUGH2, generally used in geothermal reservoir modelling, are based on the SP flow model. One might then ask, when modelling rapid transient underground boiling processes, what model should be used to best describe the flow? What are the implications for the solution of choosing a particular flow model over another? If HM flow is indeed occurring in hydrothermal eruptions, and simulators (which assume SP flow) are then used to carry out investigations, what effect does this have on the final result? A comparison of predictions for the two flow models shows, under similar conditions, the rate of progression of the boiling front and the velocity of the fluid mixture are similar for both cases, though slightly slower in the HM fluid flow model. Due to the fact that the liquid and vapour phases must move at the same speed in HM flow, the liquid phase moves markedly faster and the vapour phase somewhat slower in the HM flow case. The most significant difference between the two cases is that considerably more water is predicted to boil in HM flow. Due to a slower boiling front and more liquid water boiling in HM flow predictions, eruptions of longer duration may be deduced. The amount of water which boils may also affect conditions necessary to trigger an eruption. The more fluid that boils and escapes upwards, the greater is the lift provided to the rock in the porous medium above, and the more likely the initiation of eruption.

In an effort to determine which model in fact best describes the flow during early time periods in hydrothermal eruptions, a set of physical experiments have been carried out for comparison with the two flow models (see Section 5.3). Qualitative results from the physical experiment agree with results of the numerical experiments. However, more work is needed to obtain quantitative agreement and determine which of the two flow regimes is occurring in the porous medium. Suggestions for improvements to the experimental setup are given in Section 6.2. These suggestions, together with the work described in Section 5.3, provide a basis for future work which may help solve the fluid flow regime

mystery. Numerical simulations using HYDROTHERM have been carried out; these provide insight into features of the physical experiment (such as a resaturation front) which were due to the finiteness of the core and therefore not predicted by the semi-infinite solution. These numerical simulations were also compared with the SP flow model solution. While the influence of the boundary conditions placed on the finite core in the simulations do not allow for comparison at later time periods, there is good agreement over times where comparison can be made.

6.2 Suggestions for Future Work

Based on the conceptual model presented in Chapter 2, any complete mathematical model of a hydrothermal eruption must include: a model of the above-ground flow which includes solid material being thrown up and re-ejected in the eruptive stream; a model of the below-ground boiling processes which take place; a model which connects the above- and below-ground flows taking into account the high-speed flow effects at the interface between the two; an eroding surface and ground slumping following eruption. The mathematical modelling done in this thesis, as well as the work done by McKibbin (1990, 1996) and Bercich and McKibbin (1992), provides some insight into the underground flow and boiling processes which occur. Recently, preliminary work has also begun on methods of modelling the upwards flowing eruptive plume (Rynhart, McKibbin, and Kelly 2000). A "complete" hydrothermal eruption flow model, however, is still a distant goal. Some suggestions for extending the work in this thesis are:

- To improve the laboratory eruption model described in Chapter 2. A larger scale model may allow for quantitative measurements to be made of: the speed with which the boiling front progresses through the porous medium, the height to which material is ejected, and the radius out to which material is thrown. A series of experiments in which the pressure reduction made at the surface and the porosity of the medium in the eruption column were varied, may provide useful data for comparison with future mathematical models.

- Apply the numerical method used for plotting the streamlines in Section 4.2.2 to the quasi-steady non-isothermal flow problem. The effectiveness of this straightforward numerical technique in plotting curves which are everywhere perpendicular to a given curve was verified against analytic results in Chapter 4. In the quasi-steady non-isothermal case, ∇h_f and $\mathbf{Q}_m$ have been shown to be orthogonal (see Section 3.4). Therefore, once the conservation equations have been used to solve for either h_f or $\mathbf{Q}_m$, the numerical technique described may be used to complete

the solution.

- Use numerical simulators, such as HYDROTHERM (Hayba and Ingebritsen 1994) or TOUGH2 (Pruess 1991), to investigate vertical SP flow. In Chapter 5, results from HYDROTHERM simulations were compared to results from the SP similarity solution model. A good agreement was obtained for "early" time periods. (An increase in the length of the core used for numerical simulations will increase the length of time over which the two models are in agreement.) Similar simulations could be carried out in the vertical case. In Chapter 5 a comparison of HM and SP flow was made. Results showed a significant difference in the amount of boiling which occurred in each of the two cases. HYDROTHERM simulations may be used to compare vertical SP flow with a vertical HM flow model to determine if these differences are as great when the effects of gravity are taken into account.

- Use numerical simulators, such as HYDROTHERM or TOUGH2, to investigate the two-dimensional non-isothermal flow problem. In Chapter 4, results from the numerical solution to the problem of two-dimensional steady isothermal flow to a cylindrical well were compared with results from a HYDROTHERM simulation and good agreement was found. Figure 6.1 illustrates sample results from a simulation of non-isothermal flow towards a cylindrical hole. A series of simulations under varying initial fluid conditions, boundary conditions, crater shapes and rock matrix properties may provide future insights into the underground flow processes which occur in hydrothermal eruptions and the conditions necessary to trigger them.

- Conduct further horizontal boiling experiments using NMR (or CT scanner) equipment under improved experimental configurations. Perhaps the most beneficial improvement which could be made to the experimental setup would be the implementation of temperature control over and/or insulation of the area surrounding the core. This temperature control would allow for experiments to be run at higher temperatures, more closely approximating those in hydrothermal systems. The problem of insufficient heat in the rock matrix to allow for the continuation of boiling would be reduced. Because of the restrictions in HYDROTHERM for pressures to be greater than 0.5 *bar*, if both the pressure and saturated temperature within the core, and the ambient pressure and saturated temperature in the ambient conditions reservoir, were higher than 0.5 *bar* and $T_{sat}(0.5\ bar)$, any data obtained from the physical experiment could be compared with HYDROTHERM simulations as well as the similarity solution. There was no temperature control available in the NMR equipment used to conduct the experiments described in Chapter 5. For these experiments, it was necessary to place the saturated core in the NMR machine for

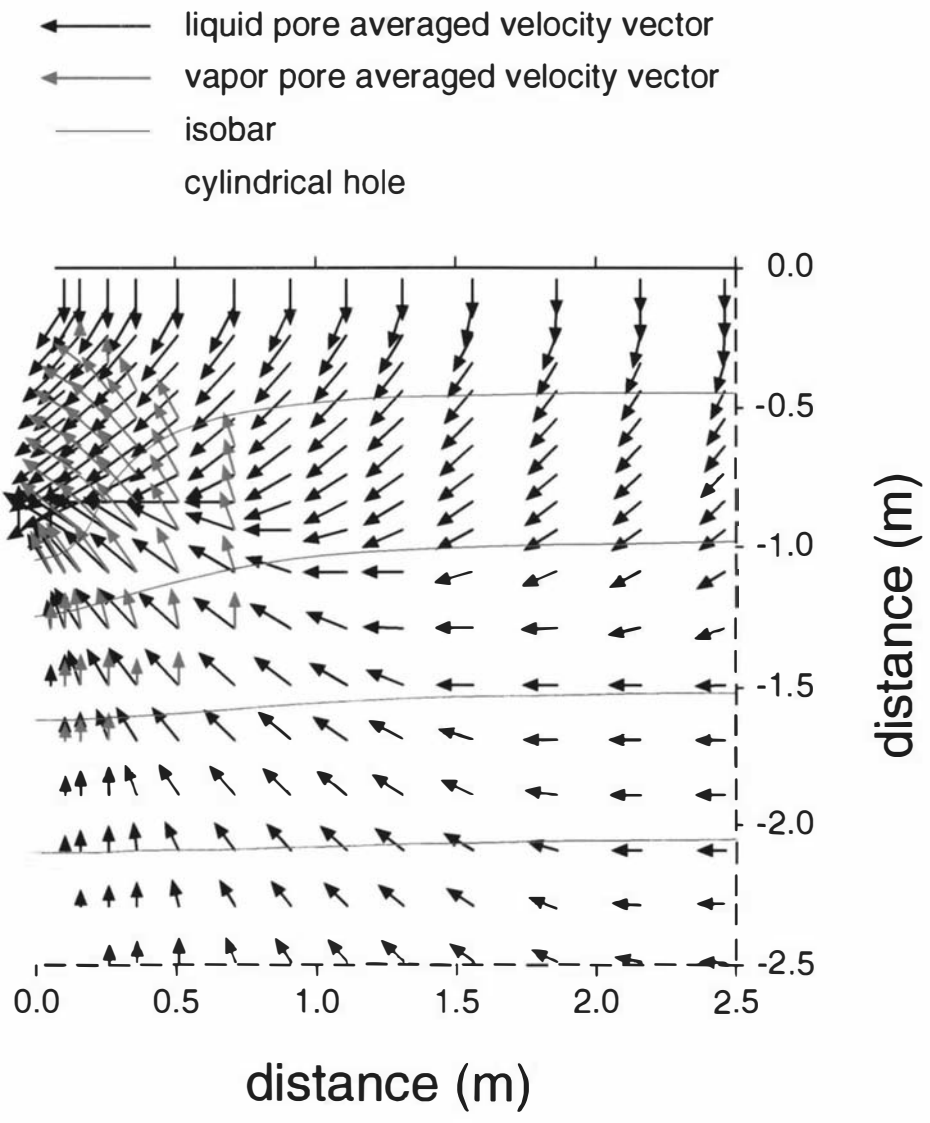

Figure 6.1: Calculated liquid water and water vapour velocity vectors from a HYDROTHERM simulation. A porous medium of porosity 0.10 and permeability $1 \times 10^{-10}\ m^2$ was initially saturated with liquid water at a temperature determined by the "boiling point with depth" relation and a pressure determined by a hydrostatic pressure gradient. A cylindrical hole of radius 0.1 m and depth 1 m was then removed from the formation. Constant atmospheric temperature and pressure conditions were placed on the surface and along the hole boundary. Results shown are those found one day after the "crater" was formed.

an extended period of time prior to the experiment in order to set up the NMR system and to take initial scans. The use of cores much above room temperature was therefore not practical. Another constructive improvement to the experimental setup would be a system which allowed for temperature measurements to be taken across the core. This may help provide a better understanding of conditions within the core during the experiment. Finally, the use of a (much) longer core may help to reduce any "early time" effects which occur due to the finiteness of the core.

Each of the above suggestions will help further the understanding of the underground flow processes involved in hydrothermal eruptions. In the end, a numerical solution of the full non-isothermal two-phase flows is needed. Any underground model formed will then eventually need to be linked to an above-ground model to determine if the connection of the two produces the desired effects. It is hoped that future modelling done may be used to give an estimate of the risk associated with given reservoir conditions and to find if there is a way to reduce that risk and indeed to find what constitute critical conditions so as to avoid them.

APPENDIX A

Conservation Equations for Horizontal Flow

In Chapter 5, an investigation of the progression of boiling fronts in one-dimensional horizontal porous media is given. A description of the problem being studied is given in Section 5.1. Section 5.2 is devoted to the solution of this problem through the use of numerical methods for two different flow cases: HM flow and SP flow. Some of the algebraic details of the derivation of the conservation equations used for solution were not included in Section 5.2 for clarity of presentation and are instead given here in Section A.1 for the HM flow case and Section A.2 for the SP flow case. The derivation of the conservation equations introduces a set of coefficients (A_1, A_2, B_1, B_2, C_1, C_2, D_1, D_2, E_1, and E_2) for each of the two cases studied which are also given in Section A.1 for the HM flow case and Section A.2 for the SP flow case.

A.1 Homogeneous Mixture (HM) Flow

From Equations 5.1, 5.3, and 5.5, the conservation of mass equation for homogeneous mixture flow in one horizontal dimension may be written in the form

$$\frac{\partial}{\partial t}(\phi\rho_f) + \frac{\partial}{\partial x}\left(-k\frac{\rho_f}{\mu_f}\frac{\partial p}{\partial x}\right) = 0 \tag{A.1}$$

For the problem described in Section 5.2, the porosity ϕ and permeability k of the porous medium are assumed to be constant. The density ρ_f and dynamic viscosity μ_f of the fluid mixture are functions of the liquid saturation S and pressure p and are given by Equations 3.3 and 3.6. Let

$$\alpha_f = \frac{\rho_f}{\mu_f} \tag{A.2}$$

Then, using Equations 3.3 and A.2, Equation A.1 may be re-written in the form

$$\phi \frac{\partial}{\partial t} \left[S\rho_l + (1 - S)\, \rho_v \right] - k \frac{\partial}{\partial x} \left(\alpha_f \frac{\partial p}{\partial x} \right) = 0 \tag{A.3}$$

Expanding Equation A.3 gives

$$\begin{aligned} \phi \left[\rho_l S_t + S \frac{\partial \rho_l}{\partial p} p_t - \rho_v S_t + (1 - S) \frac{\partial \rho_v}{\partial p} p_t \right] & \qquad \text{(A.4)} \\ -k \left(\frac{\partial \alpha_f}{\partial S} p_x S_x + \frac{\partial \alpha_f}{\partial p} p_x p_x + \alpha_f p_{xx} \right) &= 0 \end{aligned}$$

which can be written in the form

$$A_1 p_t + B_1 S_t = C_1 p_x S_x + D_1 p_x p_x + E_1 p_{xx} \tag{A.5}$$

where

$$A_1 = \phi \left[S \frac{\partial \rho_l}{\partial p} + (1 - S) \frac{\partial \rho_v}{\partial p} \right] \tag{A.6}$$

$$B_1 = \phi \left(\rho_l - \rho_v \right) \tag{A.7}$$

$$C_1 = k \frac{\partial \alpha_f}{\partial S} \tag{A.8}$$

$$D_1 = k \frac{\partial \alpha_f}{\partial p} \tag{A.9}$$

$$E_1 = k \alpha_f \tag{A.10}$$

Equation A.5, with the coefficients given in Equations A.6 - A.10, is the form of the conservation of mass equation given in Equation 5.7, Section 5.2.1.

From Equations 5.2, 5.4, and 5.6, the conservation of energy equation for homogeneous mixture flow in one horizontal dimension may be written in the form

$$\frac{\partial}{\partial t}\left[(1-\phi)\,\rho_r c_r T_{sat} + \phi \rho_f u_f\right] + \frac{\partial}{\partial x}\left(-k\frac{\rho_f}{\mu_f}h_f\frac{\partial p}{\partial x} - K\frac{\partial T_{sat}}{\partial x}\right) = 0 \qquad \text{(A.11)}$$

For the problem described in Section 5.2, the thermal conductivity K of the formation is assumed to be equal to the thermal conductivity of the rock matrix. The properties of the rock matrix (density ρ_r, heat capacity c_r, and thermal conductivity K_r) are assumed to be constant. The specific enthalpy h_f and specific internal energy u_f of the fluid mixture are functions of the liquid saturation and pressure and are given by Equations 3.4 and 3.5. The saturated temperature T_{sat} is a function of the pressure.

Let $\beta_l = \rho_l u_l$ and $\beta_v = \rho_v u_v$. Then, using Equations 3.3 and 3.5, Equation A.11 may be written in the form

$$\frac{\partial}{\partial t}\left\{(1-\phi)\,\rho_r c_r T_{sat} + \phi\left[S\beta_l + (1-S)\,\beta_v\right]\right\} \qquad \text{(A.12)}$$

$$+\frac{\partial}{\partial x}\left(-k\alpha_f h_f\frac{\partial p}{\partial x}\right) - K\frac{\partial^2}{\partial x^2}T_{sat} = 0 \qquad \text{(A.13)}$$

Expanding Equation A.13 gives

$$(1-\phi)\,\rho_r c_r\frac{\partial T_{sat}}{\partial p}p_t + \phi\left[\beta_l S_t + S\frac{\partial \beta_l}{\partial p}p_t - \beta_v S_t + (1-S)\,\frac{\partial \beta_v}{\partial p}p_t\right] \qquad \text{(A.14)}$$

$$-k\left[\left(h_f\frac{\partial \alpha_f}{\partial p} + \alpha_f\frac{\partial h_f}{\partial p}\right)p_x p_x + \left(h_f\frac{\partial \alpha_f}{\partial S} + \alpha_f\frac{\partial h_f}{\partial S}\right)S_x p_x + \alpha_f h_f p_{xx}\right]$$

$$-K\left[\frac{\partial^2 T_{sat}}{\partial p^2}p_x p_x + \frac{\partial T_{sat}}{\partial p}p_{xx}\right] = 0$$

By combining like terms, Equation A.14 can be written in the form

$$A_2 p_t + B_2 S_t = C_2 p_x S_x + D_2 p_x p_x + E_2 p_{xx} \tag{A.15}$$

where

$$A_2 = (1-\phi)\,\rho_r c_r \frac{\partial T_{sat}}{\partial p} + \phi\left[S\frac{\partial \beta_l}{\partial p} + (1-S)\frac{\partial \beta_v}{\partial p}\right] \tag{A.16}$$

$$B_2 = \phi\,(\beta_l - \beta_v) \tag{A.17}$$

$$C_2 = k\left(h_f \frac{\partial \alpha_f}{\partial S} + \alpha_f \frac{\partial h_f}{\partial S}\right) \tag{A.18}$$

$$D_2 = k\left(h_f \frac{\partial \alpha_f}{\partial p} + \alpha_f \frac{\partial h_f}{\partial p}\right) + K\frac{\partial^2 T_{sat}}{\partial p^2} \tag{A.19}$$

$$E_2 = k\alpha_f h_f + K\frac{\partial T_{sat}}{\partial p} \tag{A.20}$$

Equation A.15, with the coefficients given in Equations A.16 - A.20, is the form of the conservation of mass equation given in Equation 5.8, Section 5.2.1.

The coefficients A_1, A_2, B_1, B_2, C_1, C_2, D_1, D_2, E_1, and E_2 are functions of pressure and liquid saturation and have been calculated for numerical solutions using simple correlations and formulae for thermodynamic properties as given in Appendix B.

A.2 Separable Phase (SP) Flow

From Equations 5.1, 5.14, and 5.16, the conservation of mass equation for separable phase flow in one horizontal dimension may be written in the form

$$\frac{\partial}{\partial t}\left\{\phi\left[S\rho_l + (1-S)\,\rho_v\right]\right\} + \frac{\partial}{\partial x}\left(-kk_{rl}\frac{\rho_l}{\mu_l}\frac{\partial p}{\partial x} - kk_{rv}\frac{\rho_v}{\mu_v}\frac{\partial p}{\partial x}\right) = 0 \tag{A.21}$$

Let $\alpha_l = \rho_l/\mu_l$ and $\alpha_v = \rho_v/\mu_v$. Expanding Equation A.21 gives

$$\phi\left[\rho_l S_t + \frac{\partial \rho_l}{\partial p} S p_t - \rho_v S_t + (1-S)\frac{\partial \rho_v}{\partial p} p_t\right] \tag{A.22}$$

$$-k\left[\frac{\partial k_{rl}}{\partial S}\alpha_l p_x S_x + k_{rl}\frac{\partial \alpha_l}{\partial p} p_x p_x + k_{rl}\alpha_l p_{xx}\right.$$

$$\left.+\frac{\partial k_{rv}}{\partial S}\alpha_v p_x S_x + k_{rv}\frac{\partial \alpha_v}{\partial p} p_x p_x + k_{rv}\alpha_v p_{xx}\right] = 0$$

By combining like terms, Equation A.22 may be written in the same form as Equation A.5 where the coefficients for this separable phase flow case are given by

$$A_1 = \phi\left[\frac{\partial \rho_l}{\partial p} S + \frac{\partial \rho_v}{\partial p}(1-S)\right] \tag{A.23}$$

$$B_1 = \phi(\rho_l - \rho_v) \tag{A.24}$$

$$C_1 = k\left(\frac{\partial k_{rl}}{\partial S}\alpha_l + \frac{\partial k_{rv}}{\partial S}\alpha_v\right) \tag{A.25}$$

$$D_1 = k\left(k_{rl}\frac{\partial \alpha_l}{\partial p} + k_{rv}\frac{\partial \alpha_v}{\partial p}\right) \tag{A.26}$$

$$E_1 = k(k_{rl}\alpha_l + k_{rv}\alpha_v) \tag{A.27}$$

Equation A.5, with the coefficients given in Equations A.23 - A.27, is the form of the conservation of mass equation used in Section 5.2.2. (See Equation 5.7.)

Let $\beta_l = \rho_l u_l$, $\beta_v = \rho_v u_v$, $\gamma_l = \rho_l h_l/\mu_l = h_l/\nu_l$, and $\gamma_v = \rho_v h_v/\mu_v = h_v/\nu_v$. Then, by Equations 5.2, 5.15, and 5.17, the conservation of energy equation for separable phase flow in one horizontal dimension may be written in the form

$$\frac{\partial}{\partial t}\{(1-\phi)\rho_r c_r T_{sat} + \phi[S\beta_l + (1-S)\beta_v]\} \tag{A.28}$$

$$+\frac{\partial}{\partial x}\left[-kk_{rl}\gamma_l\frac{\partial p}{\partial x} - kk_{rv}\gamma_v\frac{\partial p}{\partial x}\right] - K\frac{\partial^2 T_{sat}}{\partial x^2} = 0$$

Expanding Equation A.28 gives

$$(1-\phi)\,\rho_r c_r \frac{\partial T_{sat}}{\partial p} p_t + \phi \left[\beta_l S_t + S\frac{\partial \beta_l}{\partial p} p_t - \beta_v S_t + (1-S)\frac{\partial \beta_v}{\partial p} p_t\right] \tag{A.29}$$

$$-k\left[\frac{\partial k_{rl}}{\partial S}\gamma_l p_x S_x + k_{rl}\frac{\partial \gamma_l}{\partial p} p_x p_x + k_{rl}\gamma_l p_{xx}\right.$$

$$\left.+\frac{\partial k_{rv}}{\partial S}\gamma_v p_x S_x + k_{rv}\frac{\partial \gamma_v}{\partial p} p_x p_x + k_{rv}\gamma_v p_{xx}\right]$$

$$-K\left[\frac{\partial^2 T_{sat}}{\partial p^2} p_x p_x + \frac{\partial T_{sat}}{\partial p} p_{xx}\right] = 0$$

By combining like terms, Equation A.29 may be written in the same form as Equation A.15 where the coefficients for this separable phase flow case are given by

$$A_2 = (1-\phi)\,\rho_r c_r \frac{\partial T_{sat}}{\partial p} + \phi\left[S\frac{\partial \beta_l}{\partial p} + (1-S)\frac{\partial \beta_v}{\partial p}\right] \tag{A.30}$$

$$B_2 = \phi\,(\beta_l - \beta_v) \tag{A.31}$$

$$C_2 = k\left(\frac{\partial k_{rl}}{\partial S}\gamma_l + \frac{\partial k_{rv}}{\partial S}\gamma_v\right) \tag{A.32}$$

$$D_2 = k\left(k_{rl}\frac{\partial \gamma_l}{\partial p} + k_{rv}\frac{\partial \gamma_v}{\partial p}\right) + K\frac{\partial^2 T_{sat}}{\partial p^2} \tag{A.33}$$

$$E_2 = k\,(k_{rl}\gamma_l + k_{rv}\gamma_v) + K\frac{\partial T_{sat}}{\partial p} \tag{A.34}$$

Equation A.15, with the coefficients given in Equations A.30 - A.34, is the form of the conservation of mass equation used in Section 5.2.2. (See Equation 5.8.)

The coefficients A_1, A_2, B_1, B_2, C_1, C_2, D_1, D_2, E_1, and E_2 for this case are again functions of pressure and liquid saturation and have been calculated for numerical solutions using simple correlations for thermodynamic properties as given in Appendix B.

APPENDIX B

Correlations and Formulae for Thermodynamic Properties of Water

In Chapter 5, a study of the progression of boiling fronts in one-dimensional horizontal porous media is presented. In order to complete the solution to the problem described in Section 5.2, Equations 5.11 - 5.13 must be solved under the boundary conditions given in Figure 5.2 for each of two (homogeneous mixture and separable phase) flow cases. The coefficients A_1, A_2, B_1, B_2, C_1, C_2, D_1, D_2, E_1, and E_2 contained in Equations 5.11 - 5.13 are given in Appendix A in terms of various thermodynamic properties of water.

A set of formulae describing the thermodynamic properties of the homogeneous fluid mixture (necessary for solution) are given in Equations B.1 - B.6. By Equations A.2, 3.3, and 3.6,

$$\alpha_f = \frac{\rho_f}{\mu_f} = \frac{S\rho_l + (1-S)\,\rho_v}{S\mu_l + (1-S)\,\mu_v} \tag{B.1}$$

$$\frac{\partial \alpha_f}{\partial p} = \left\{ \left[S\mu_l + (1-S)\,\mu_v\right] \left[S\frac{\partial \rho_l}{\partial p} + (1-S)\,\frac{\partial \rho_v}{\partial p}\right] \right. \tag{B.2}$$

$$\left. -S\left[S\rho_l + (1-S)\,\rho_v\right] \left(\frac{\partial \mu_l}{\partial p} - \frac{\partial \mu_v}{\partial p}\right) \right\} /$$

$$\left[S\mu_l + (1-S)\,\mu_v\right]^2$$

$$\frac{\partial \alpha_f}{\partial S} = \frac{\mu_v\rho_l - \mu_l\rho_v}{\left[S\mu_l + (1-S)\,\mu_v\right]^2} \tag{B.3}$$

By Equation 3.4,

$$h_f = \frac{S\rho_l h_l + (1-S)\,\rho_v h_v}{S\rho_l + (1-S)\,\rho_v} \tag{B.4}$$

$$\frac{\partial h_f}{\partial p} = \left\{ S(1-S)\left[\left(\rho_l \frac{\partial \rho_v}{\partial p} - \frac{\partial \rho_l}{\partial p}\rho_v\right)(h_v - h_l) + \rho_l \rho_v \left(\frac{\partial h_l}{\partial p} + \frac{\partial h_v}{\partial p}\right)\right] \right. \tag{B.5}$$

$$\left. + (1-S)^2 \rho_v^2 \frac{\partial h_v}{\partial p} + S^2 \rho_l^2 \frac{\partial h_l}{\partial p} \right\} /$$

$$[S\rho_l + (1-S)\,\rho_v]^2$$

$$\frac{\partial h_f}{\partial S} = \frac{\rho_l \rho_v (h_l - h_v)}{[S\rho_l + (1-S)\,\rho_v]^2} \tag{B.6}$$

Using data taken from Rogers and Mayhew (1980), a set of simple correlations describing the necessary thermodynamic properties of the liquid and vapour phases over the temperature and saturated pressure ranges of interest were determined and are presented in Table B.1 for $611.2 \leq p \leq 12330\ Pa$ $(0.01 \leq T_{sat}(p) \leq 50°C)$ and Table B.2 for $1 \times 10^5 \leq p \leq 5 \times 10^5\ Pa$ $(99.6 \leq T_{sat}(p) \leq 151.8°C)$. The correlations found are of one of three types: $f = Ap^n$, $f = B\ln(kp)$, and $f = ap^2 + bp + c$. For functions of the type $f = Ap^n$ and $f = B\ln(kp)$ least square methods have been used to find the best line fit through log-log or semi-log plots of data respectively, while for $f = ap^2 + bp + c$ least squares methods were used to find the best quadratic fit to the data. There is close agreement between the steam table data and the correlations given in Tables B.1 and B.2.

Table B.1: Correlations for thermodynamic properties of liquid water and water vapour in the saturated pressure range $611.2 \leq p \leq 12330\ Pa$ $(0.01 \leq T_{sat}(p) \leq 50°C)$.

Correlation	Coefficients	Value of Coefficient
$h_l = B_{h_l} \ln(k_{h_l} p)$	B_{h_l}	6.9047×10^4
	k_{h_l}	1.5048×10^{-3}
$h_v = A_{h_v} p^{n_{h_v}}$	A_{h_v}	2.3166×10^6
	n_{h_v}	1.1794×10^{-2}
$\mu_l = A_{\mu_l} p^{n_{\mu_l}}$	A_{μ_l}	2.0648×10^{-2}
	n_{μ_l}	-0.38823
$\mu_v = A_{\mu_v} p^{n_{\mu_v}}$	A_{μ_v}	5.7266×10^{-6}
	n_{μ_v}	6.0987×10^{-2}
$\rho_l = a_{\rho_l} p^2 + b_{\rho_l} p + c_{\rho_l}$	a_{ρ_l}	2.8334×10^{-8}
	b_{ρ_l}	-1.4085×10^{-3}
	c_{ρ_l}	1.0011×10^3
$\rho_v = A_{\rho_v} p^{n_{\rho_v}}$	A_{ρ_v}	1.1296×10^{-5}
	n_{ρ_v}	0.9453
$\alpha_l = A_{\alpha_l} p^{n_{\alpha_l}}$	A_{α_l}	4.9319×10^4
	n_{α_l}	0.38552
$\alpha_v = a_{\alpha_v} p^2 + b_{\alpha_v} p + c_{\alpha_v}$	a_{α_v}	-8.2518×10^{-6}
	b_{α_v}	0.74877
	c_{α_v}	1.5308×10^2
$\beta_l = B_{\beta_l} \ln(k_{\beta_l} p)$	B_{β_l}	6.9503×10^7
	k_{β_l}	1.4801×10^{-3}
$\beta_v = A_{\beta_v} p^{n_{\beta_v}}$	A_{β_v}	25.3119
	n_{β_v}	0.9544
$\gamma_l = a_{\gamma_l} p^2 + b_{\gamma_l} p + c_{\gamma_l}$	a_{γ_l}	-1.2149×10^3
	b_{γ_l}	4.7685×10^7
	c_{γ_l}	-2.4618×10^{10}
$\gamma_v = a_{\gamma_v} p^2 + b_{\gamma_v} p + c_{\gamma_v}$	a_{γ_v}	-19.008
	b_{γ_v}	1.9152×10^6
	c_{γ_v}	3.4871×10^8
$T_{sat} = B_T \ln(k_T p)$	B_T	16.500
	k_T	1.5025×10^{-3}

Table B.2: Correlations for thermodynamic properties of liquid water and water vapour in the saturated pressure range $1 \times 10^5 \leq p \leq 5 \times 10^5\ Pa$ $(99.6 \leq T_{sat}(p) \leq 151.8°C)$.

Correlation	Coefficients	Value of Coefficient
$h_l = A_{h_l} p^{n_{h_l}}$	A_{h_l}	1.9707×10^4
	n_{h_l}	0.26554
$h_v = A_{h_v} p^{n_{h_v}}$	A_{h_v}	2.2019×10^6
	n_{h_v}	1.6906×10^{-2}
$\mu_l = A_{\mu_l} p^{n_{\mu_l}}$	A_{μ_l}	7.0370×10^{-3}
	n_{μ_l}	-0.28022
$\mu_v = A_{\mu_v} p^{n_{\mu_v}}$	A_{μ_v}	4.0301×10^{-6}
	n_{μ_v}	9.4704×10^{-2}
$\rho_l = a_{\rho_l} p^2 + b_{\rho_l} p + c_{\rho_l}$	a_{ρ_l}	1.0765×10^{-10}
	b_{ρ_l}	-1.7288×10^{-4}
	c_{ρ_l}	9.7387×10^2
$\rho_v = A_{\rho_v} p^{n_{\rho_v}}$	A_{ρ_v}	1.2151×10^{-5}
	n_{ρ_v}	0.9372
$\alpha_l = A_{\alpha_l} p^{n_{\alpha_l}}$	A_{α_l}	1.8698×10^5
	n_{α_l}	0.25278
$\alpha_v = A_{\alpha_v} p^{n_{\alpha_v}}$	A_{α_v}	3.0362
	n_{α_v}	0.8420
$\beta_l = A_{\beta_l} p^{n_{\beta_l}}$	A_{β_l}	2.6504×10^7
	n_{β_l}	0.2364
$\beta_v = A_{\beta_v} p^{n_{\beta_v}}$	A_{β_v}	25.9991
	n_{β_v}	0.9510
$\gamma_l = A_{\gamma_l} p^{n_{\gamma_l}}$	A_{γ_l}	3.6848×10^9
	n_{γ_l}	0.5183
$\gamma_v = a_{\gamma_v} p^2 + b_{\gamma_v} p + c_{\gamma_v}$	a_{γ_v}	-0.21785
	b_{γ_v}	1.1124×10^6
	c_{γ_v}	2.4269×10^{10}
$T_{sat} = A_T p^{n_T}$	A_T	5.0345
	n_T	0.2598

The simple linear functions given in Equations B.7 and B.8 (also known as X-curves) were used to describe the relative permeabilities k_{rl} and k_{rv}. (The residual saturations S_{lr} and S_{vr} are both assumed to be zero.)

$$k_{rl} = S \tag{B.7}$$

$$k_{rv} = 1 - S \tag{B.8}$$

[See Guerrero (1998) for more details on these and other relative permeability curves.]

Bibliography

Allis, R. A. (1979). Thermal history of the Karapiti Area, Wairakei. Report 137, DSIR Geophysics Division.

Allis, R. A. (1983). The 9th April 1983 steam eruption at Craters of the Moon Thermal Area, Wairakei. Report 196, DSIR Geophysics Division.

Anderson, L. W., J. W. Anderegg, and J. E. Lawler (1978). Model geysers. *Am. Jour. Sci. 278*, 725–738.

Bear, J. and Y. Bachmat (1991). *Introduction to Modeling of Transport Phenomena in Porous Media.* Kluwer Academic Publishers.

Bercich, B. J. and R. McKibbin (1992). Modelling the development of natural hydrothermal eruptions. In *Proc. 14th NZ Geothermal Workshop 1992*, pp. 305–312. University of Auckland. Corrigendum (1993) *Proc. 15th NZ Geothermal Workshop 1993,* University of Auckland, 345-346.

Bixley, P. F. and P. R. L. Browne (1988). Hydrothermal eruption potential in geothermal development. In *Proc. 10th NZ Geothermal Workshop 1988*, pp. 195–198. University of Auckland.

Bromley, C. J. and M. A. Mongillo (1994). Hydrothermal eruptions - a hazard assessment. In *Proc. 16th NZ Geothermal Workshop 1994*, pp. 45–50. University of Auckland.

Brotheridge, J. M., P. R. L. Browne, and M. P. Hochstein (1995). The Ngatamariki geothermal field, New Zealand: surface manifestations past and present. In *Proc. 17th NZ Geothermal Workshop 1995*, pp. 61–66. University of Auckland.

Browne, P. R. L. (1986). Near surface geology and hydrothermal eruption history of the Rotokawa Geothermal Field. Report, Ministry of Works and Development.

Browne, P. R. L. and J. V. Lawless. Characteristics of hydrothermal eruptions with examples from New Zealand and elsewhere. *Earth Science Reviews*, (in press).

Bruno, C. A. E., J. A. Burgos, and S. Ayala (December, 1992). Agua Shuca hydrothermal eruption. *Geotherm. Res. Council Bull.*, 361–369.

Collar, R. J. (1985). Hydrothermal eruptions in the Rotokawa Geothermal System, Taupo Volcanic Zone, New Zealand. Report GIR 14, Geothermal Institute, University of Auckland.

Collar, R. J. and P. R. L. Browne (1985). Hydrothermal eruptions at the Rotokawa Geothermal Field, Taupo Volcanic Zone, New Zealand. In *Proc. 7th NZ Geothermal Workshop 1985*, pp. 171–175. University of Auckland.

Cross, D. (1963). Soils and geology of some hydrothermal eruptions in the Waiotapu District. *NZ Jour. Geol. Geophys. 6*, 70–87.

Dench, N. D. (1988). Hazards and safety measures in geothermal projects. In *Proc. 10th NZ Geothermal Workshop 1988*, pp. 199–203. University of Auckland.

Dominion (Wednesday January 26, 2000). Eruptions scaring residents. *The Dominion*, Wellington, New Zealand.

Dowden, J., P. Kapadia, G. Brown, and H. Rymer (1991). Dynamics of a geyser eruption. *Jour. Geophys. Res. 96*(B11), 18059–18071.

Espanola, O. S. (1974). Geology and hot springs of Tikitere and Taheke hydrothermal fields, Rotorua, New Zealand. *N.Z. Geol. Surv. Rep. 68.*

Goff, S. and F. Goff (1997). Environmental impacts during geothermal development: some examples from Central America. In *Proc. NEDO Int. Geotherm. Symp., March 1997*, pp. 242–250. Sendai, Japan.

Grindley, G. W. (1982). Report on a visit to geothermal fields under exploration in Leyte, Southern Negros and Southern Luzon, Republic of the Philippines. Report G.59, N.Z. Geol. Surv. Rep.

Guerrero, M. T. (June 1998). Estimation of relative permeability from a dynamic boiling experiment. Master's thesis, Stanford University, available at http://ekofisk.stanford.edu/geoth/sgprpts.html.

Hayba, D. O. and S. E. Ingebritsen (1994). The computer model HYDROTHERM, a three-dimensional finite-difference model to simulate ground-water flow and heat transport in the temperature range of 0 to 1,200°C. Report 94-4045, U.S. Geological Survey Water-Resources Investigations, HYDROTHERM software available at http://water.usgs.gov/software/hydrotherm.html.

Hedenquist, J. W. and R. W. Henley (1985). Hydrothermal eruptions in the Waiotapu Geothermal System, New Zealand: Their origin, associated breccias, and relation to precious metal mineralization. *Econ. Geol. 80*, 1640–1688.

Lloyd, E. and R. Keam (1965). Waimangu in New Zealand Volcanology: Central Volcanic Region. Technical report, D.S.I.R. Information Series 50.

Lloyd, E. F. (1959). The hot springs and hydrothermal eruptions of Waiotapu. *J. Geol. Geophys. 2*, 141–176.

Lloyd, E. F. (1972). Geology and hot springs of Orakeikorako. *N.Z. Geol. Surv. Bull. 85.*

Lloyd, E. F. and R. F. Keam (1974). Trinity Terrace hydrothermal eruption, Waimangu, New Zealand. *New Zealand J. Sci. 17*, 511–528.

Luketina, K. M. (1995). *The history and application of geyser theory.* Post-Graduate Diploma of Science dissertation, University of Auckland, Auckland, New Zealand.

Marini, L., C. Principe, G. Chiodini, R. Cioni, M. Fytikas, and G. Marinelli (1993). Hydrothermal eruptions of Nisyros (Dodecanese, Greece). Past events and present hazard. *J. Volcanol. Geoth. Res. 56*, 71–94.

Mastin, L. G. (1995). Thermodynamics of gas and steam-blast eruptions. *Bull. Volcanol. 57*, 84–98.

McKibbin, R. (1989). An attempt at modelling hydrothermal eruptions. In *Proc. 11th NZ Geothermal Workshop 1989*, pp. 267–273. University of Auckland.

McKibbin, R. (1990). Mathematical modelling of hydrothermal eruptions. In *1990 Internationsl Symposium on Geothermal Energy, Geothermal Resources Council Transactions*, Volume 14, Part 2, pp. 1309–1316.

McKibbin, R. (1996). Could non-condensible gases affect hydrothermal eruptions? In *Proc. 18th NZ Geothermal Workshop 1996*, pp. 323–330. University of Auckland.

Morgan, P. G. (1917). Eruption of Frying Pan Flat, near Waimangu, Rotorua District. Report, New Zealand Geological Survey. 11th Ann. Rep. C-2B.

Muffler, L. P. J., D. E. White, and A. H. Truesdell (1971). Hydrothermal explosion craters in Yellowstone National Park. *Geol. Soc. Amer. Bull. 82*, 723–740.

Nairn, I. A. and S. Wiradiradja (1980). Late Quarternary hydrothermal explosion breccias at Kawerau Geothermal Field, New Zealand. *Bull. Volcanol. 43*, 1–13.

Nelson, C. E. and D. L. Giles (1985). Hydrothermal eruption mechanisms and hot spring gold deposits. *Econ. Geol. 80*, 1633–1639.

NGT (1994). National Geographic: Explorer - Valley of Ten Thousand Smokes on the Alaskan Peninsula. *National Geographic Television*, videocassette.

Nield, D. A. and A. Bejan (1992). *Convection in Porous Media.* Springer-Verlag New York.

NZHerald (Friday January 21, 2000). Muddy eruption jolts expert. *New Zealand Herald*, Auckland, New Zealand.

O'Sullivan, M. J. and R. McKibbin (1989). *Geothermal Reservoir Engineering.* Geothermal Institute, University of Auckland.

Potton, C. and P. Woods (1990). *Yesterday's New Earth, New Zealand's Geothermal Landscape.* Craig Potton Publishing Ltd.

Pruess, K. (1987). TOUGH User's Guide. Earth Science Division, Lawrence Berkeley Laboratory, LBL-20700, NUREG/CR-4645.

Pruess, K. (1991). TOUGH2 - A General-Purpose Numerical Simulator for Multiphase Fluid and Heat Flow. Earth Science Division, Lawrence Berkeley Laboratory, LBL-29400.

Rogers, G. F. C. and Y. R. Mayhew (1980). *Thermodynamic and Transport Properties of Fluids* (Third ed.). Basil Blackwell Publisher.

Rynhart, P. R., R. McKibbin, and D. R. Kelly (2000). Modelling the flight of hydrothermal eruption ejecta. In *Proc. 22th NZ Geothermal Workshop 2000.* University of Auckland. (in press).

Scott, B. (1992). Waimangu. A Volcanic Encounter. Report, Waimangu Volcanic Valley.

Scott, B. J. and A. D. Cody (1982). The 20 June 1981 hydrothermal explosion at Tauhara Geothermal Field, Taupo. Report 103, DSIR Report NZGS.

Shepherd, C. (March, 1903). Waimangu Geyser Eruption. *Collection: National Museum of New Zealand*, Photograph.

Smith, T. A. and R. McKibbin (1997). Modelling of hydrothermal eruptions: A review. In *Proc. 19th NZ Geothermal Workshop 1997*, pp. 123–128. University of Auckland.

Smith, T. A. and R. McKibbin (1998). Towards a hydrothermal eruption flow model. In *Proc. 20th NZ Geothermal Workshop 1998*, pp. 387–392. University of Auckland.

Smith, T. A. and R. McKibbin (1999). An investigation of boiling processes in hydrothermal eruptions. In *Proc. 21st NZ Geothermal Workshop 1999*, pp. 229–236. University of Auckland.

Smith, T. A. and R. McKibbin (2000). An investigation of boiling processes in hydrothermal eruptions. In E. Eglesias, D. Blackwell, T. Hunt, J. Lund, S. Tamanyu, and K. Kimbora (Eds.), *Proc. World Geothermal Congress 2000*, pp. 699–704. International Geothermal Association.

White, D. E. (1955). Violent mud-volcano eruption of Lake City Hot Springs, Northeastern California. *Bull. Geol. Soc. Amer. 66*, 1109–1130.

Wold, R. J., M. A. Mayhew, and R. B. Smith (1977). Bathymetric and geophysical evidence for a hydrothermal explosion crater in Mary Bay, Yellowstone Lake, Wyoming. *Jour. Geophys. Res. 82*(26), 3733–3738.

Yuhara, K. (1997). Review of hydrothermal eruptions. *J. Jap. Geotherm. Energy Ass. 34* (149), 18–34.